ONE STAR SHINES ON MANY WORLDS: EXPLORING EXTRATERRESTRIAL WATER THROUGH OBSERVATIONS OF SCATTERED LIGHT ON THE MOON AND MARS

Conor W. Hayes

A THESIS SUBMITTED TO THE FACULTY OF GRADUATE STUDIES IN PARTIAL FULFILLMENT OF THE REQUREMENTS FOR THE DEGREE OF

MASTER OF SCIENCE

GRADUATE PROGRAM IN PHYSICS AND ASTRONOMY
YORK UNIVERSITY
TORONTO, ONTARIO

SEPTEMBER 2022

Abstract

We investigate interactions between scattered light and water on the Moon and Mars. On the Moon, we develop an illumination and thermal model to examine small-scale temperatures and the thermal stability of volatile molecules at the Lunar Crater Observation and Sensing Satellite (LCROSS) impact site. We find that small-scale surface roughness creates a maximum temperature spread of approximately 10 K.

On Mars, we derive a scattering phase function for Aphelion Cloud Belt water-ice clouds (WICs) during Mars Years $34 - 36$ using Mars Science Laboratory cloud movies. We compared our phase functions with seven previously-derived Martian WIC phase functions and two Martian dust phase functions, as well as modeled phase functions for seven different ice crystal geometries. We find poor to moderate agreement with our phase functions. We also investigate interannual and diurnal variabilty of our phase functions, finding that any variability is minimal, consistent with previous results.

Acknowledgements

First, I would like to express my deepest gratitude to my supervisor, Dr. John Moores both for taking a chance on me after a clerical error ended with my program application on his desk and for the support that he has provided me with over the last two years. Being isolated at home due to COVID restrictions during the first year and a half of my time at York was often mentally taxing, and John was always available to help me talk through my challenges and set me back on track. The environment that he has helped build in the Planetary Volatiles Laboratory was a significant part of why I agreed to join PVL despite not initially wanting to do a research-focused Master's, and why I eventually decided to continue on to a Ph.D. under his supervision despite coming in with no intention of doing so. Two years ago, I left undergrad feeling like a didn't have a clear path into the future, and now I'm looking forward to working together for another four years.

I would also like to thank the other members of PVL, both past and present, for helping me feel like I had a community at my side even when we couldn't work in the same office. My special thanks go to Dr. Jake Kloos, who helped guide me through the introductory phases of my lunar work, as well as Charissa Campbell, Alex Innanen, and Grace Bischof for helping me quickly pivot to Mars.

Finally, I would like to thank my family, without whom none of this would have been possible. Thank you for your love and support, and for letting me ramble on at length about clouds during family Zoom calls.

Table of Contents

List of Tables

List of Figures

Chapter 1

Introduction

Our planet is home to a truly astonishing collection of living beings, so varied in their physical characteristics that one might be disinclined to believe that they all share a single common ancestor. There is, however, a small set of basic needs that all life discovered to date on Earth has in common. Perhaps the most fundamental of these needs is liquid water. Although we have found forms of life that have adapted to survive in extremely arid environments for extended periods of time, every living creature will eventually die without sufficient water. For this reason, the presence of water is the first thing that we look for when assessing the potential habitability (either past or present) of extraterrestrial worlds.

Astronomy occupies a special place among the sciences because, unlike those who choose to study other fields, astronomers are generally unable to directly interact with the subjects of their research. The subfield of planetary science is an occasional exception to this rule, as it is possible to retrieve samples from other worlds and bring them back to us, but this is rarely exercised for practical reasons of cost and mission complexity. As a result, we must rely almost exclusively on remote sensing. To properly interpret our data, we need to develop models of the ways in which light interacts with the various forms of matter present in the universe. The development and implementation of a few of these models forms the core of this thesis.

Specifically, we will be examining interactions between scattered sunlight and water on the Moon and Mars. The first half of the thesis, which focuses on the Moon, looks at how sunlight scattered off of illuminated terrain into regions of permanent shadow at its poles influences temperatures (and thus the potential distribution of water and other volatile molecules) at small scales. In the second half, which focuses on Mars, we will be deriving a scattering phase function for Martian water-ice clouds and seeing if our results can tell us anything about the shape of the ice crystals that compose the clouds.

1.1   Searching for Water on the Moon

Because the Moon is located relatively near to Earth and its surface is viewable in fairly high detail with even a small telescope, its generally dry nature was inferred without much difficulty. Although radical ideas were occasionally put forward, such as Peter Andreas Hansen's 1854 proposal that the Moon's centre of gravity was offset from its physical centre by 59 kilometres, thus allowing an Earth-like atmosphere with liquid water and life to exist on its far side (Hansen, 1854), it was widely accepted by the end of the 19th century that the Moon was devoid of water.

This state of affairs continued until the mid-20th century, when Harold Urey, a Nobel Prize-winning chemist who played a significant role in convincing NASA to prioritize lunar exploration (Newell, 1973), began to publish a series of papers based on data returned from the Ranger probes in the 1960s. Urey claimed that these images, the first taken of the Moon at close range, contained substantial evidence of features formed by liquids interacting with the surface (Urey, 1956, 1965; Urey et al., 1967). Needless to say, Urey's willingness to challenge the status quo on lunar water was extremely controversial and made him the subject of harsh criticism and ridicule from other members of the planetary science community. Despite the criticism, Urey continued to defend his theories until the Apollo missions returned the first lunar rock samples to Earth.

The Apollo program returned ample evidence suggesting that not only was the Moon presently devoid of water, it likely never had any substantial amount of water present on its surface. For example, Apollo 15 landed near Rima Hadley, a sinuous rille similar to rilles elsewhere on the Moon's surface that Urey had argued were formed by flowing water due to their resemblance to terrestrial river channels. However, returned samples from the rille and surrounding area were igneous in origin, suggesting that the rille (and presumably others like it) were carved by lava rather than water (Apo, 1972).

Apollo also returned samples of lunar vesicular basalt. This is basalt that formed through the cooling of lava containing dissolved gases that expanded as the lava cooled, leaving behind a rock full of vesicles (holes). If the dissolved gas was water vapour, one would expect to see hydrated minerals like amphiboles. The returned samples are almost completely devoid of these minerals, instead being composed largely of pyroxene, olivine, and plagioclase feldspar (Lucey, 2006).

Although Urey's theories of flowing water on the lunar surface were thoroughly disproven, another of his theories motivates much of modern lunar exploration, including the base camp site selection for the upcoming Artemis missions and the first half of this thesis. In Urey (1952), he proposed the existence of large permanently-shadowed regions (PSRs) near the lunar poles. Based on simple geometry, Urey realized that the maximum elevation angle that the Sun reaches on the sky is determined by the difference in latitude between an observer on the surface and the subsolar point. The latitude of the subsolar point is itself controlled by the time of year and the angle between the body's rotational axis and its orbital plane around the Sun. Though the Moon does not (directly) orbit the Sun, its obliquity of 6.68° combines with the 5.15° inclination of its orbit around the Earth to produce an angle of just 1.53° between its rotational axis and the plane of the ecliptic (Watson et al., 1961). Consequently, near the lunar poles, the Sun will never appear more than a few degrees above the zero-elevation horizon. If local topographic features create a horizon that is significantly higher than this in all directions (e.g. at the floor of an impact crater surrounded by steep walls),

then the Sun will never rise.

This theory of PSRs provoked scientific interest because, without an atmosphere to facilitate heat transfer between illuminated and shadowed portions of the lunar surface, PSRs can be exceptionally cold ($< 110K$; Vasavada et al., 1999). Furthermore, because the Moon's current rotational and orbital parameters have remained stable near their current values for at least the past billion years (Siegler et al., 2015), lunar PSRs have maintained these low temperatures long enough for a potentially significant volume of volatile materials like water ice that would otherwise rapidly sublimate away to become "cold-trapped" within them.

In the ~ 30 years following Urey (1952), great efforts were made to estimate how much water ice might be trapped near the lunar poles. Using estimates of crater sizes and spatial distribution, Watson et al. (1961) concluded that the Moon may have formed with 3.0×10^4 grams of water per square centimetre, assuming that the Moon and Earth followed similar evolutionary paths (For reference, they cite the Earth as having a water abundance of 1.8×10^5 g cm^{-2}, or ~ 6 times as much as the Moon). More quantitative estimates were provided by Öpik (1962), who argued that the sublimation into PSRs of water molecules formed solely through interactions between the solar wind and lunar regolith was sufficient to form water ice deposits ~ 100 metres thick; as well as Arnold (1979), whose analysis of the sources, transport methods, and destructive mechanisms of lunar water concluded that there may be $10^{16} - 10^{17}$ grams of water present on the Moon (approximately $5 - 6$ orders of magnitude less than was estimated by Watson et al. (1961)).

It should be noted that not everyone was so optimistic about the possibility of lunar glaciers. For example, Lanzerotti et al. (1981) used laboratory measurements of water ice erosion to find a loss rate due to ions in the solar wind and Earth's magnetosphere of $\sim 10^6$ molecules cm^2 s^{-1}, comparable to the deposition rate of $\sim 10^7$ molecules cm^2 s^{-1} calculated by Arnold (1979). Because the ion-eroded water molecules would have sufficient energy to jump ≥ 500 km across the lunar surface, they conclude that the interplanetary ion flux is sufficient to prevent ice from accumulating in PSRs in significant amounts.

1.1.1 Exploring the Volatile Content of Lunar PSRs

The only way to resolve the question of whether or not water ice existed at the lunar poles and, if so, in what quantities, was to actually survey the polar regions. This effort is still ongoing today, with the upcoming Volatiles Investigating Polar Exploration Rover (VIPER) mission set to perform the first *in-situ* analysis of the Moon's volatile resources by late 2023 (Colaprete et al., 2021).

Radar Measurements

The first attempts at quantifying the abundance of water ice present on the Moon used radar measurements, both from Earth-based observatories and from spacecraft in lunar orbit. Radar can be used to identify water ice because water ice is both highly reflective at radar wavelengths and has a high circular polarization ratio (CPR), which describes the ratio of reflected light that is polarized in the same versus opposite direction as the transmitted signal. Each time that a circularly-polarized beam of light scatters off of a surface, its polarization direction changes. A radar signal incident upon a relatively smooth, ice-free surface will generally scatter once before returning to the detector, resulting in a measurement that is mostly opposite-polarized from the source. A rocky, ice-covered surface will scatter the signal several times, causing the returning signal to be a mix of both same- and opposite-polarized light.

The Clementine spacecraft (Nozette et al., 1994) was the first to conduct these measurements via a bistatic radar experiment that was improvised after arriving at the Moon. Though Clementine was not equipped to make radar measurements, it used its radio communication equipment to bounce signals off of the lunar surface, which were then detected on Earth by the various antennae that comprise the Deep Space Network. The results of this experiment were promising, though far from conclusive. Of the four orbits during which the experiment was conducted, the one that took the spacecraft over the south pole showed a significantly higher CPR than the three that did not, which is consistent with polar ice

deposits (Nozette et al., 1996). However, Nozette et al. (1996) do concede that their results could be explained by surface roughness effects rather than water ice – a sufficiently rough surface can scatter the radar signal multiple times in a similar way to what is observed with ice, leading to an apparent detection of ice on a dry surface. Additionally, the large and imprecise footprint of the improvised instrument cannot distinguish between surface-exposed ice and ice that has been mixed in with the regolith.

Further radar measurements using the Arecibo Telescope (Stacy et al., 1997) cast additional doubt on the conclusions of Nozette et al. (1996). Specifically, Arecibo measured CPR values in sunlit craters similar to those that Nozette et al. (1996) found in the polar regions, suggesting that these results were more likely than not due to surface roughness rather than water ice, as water ice would rapidly sublimate away when exposed to sunlight.

Neutron Spectroscopy

Another way that water ice can be detected from orbit is through neutron spectroscopy. This technique takes advantage of the fact that the hydrogen atoms in a water molecule are roughly the same mass as the spallation neutrons that are created when high-energy cosmic rays impact the lunar regolith. As a result of this mass equivalence, a collision between a spallation neutron and a hydrogen atom will see a significant portion of the neutron's momentum transferred to the hydrogen atom (Lingenfelter et al., 1961). Consequently, a spacecraft observing an area with a high concentration of hydrogen atoms will see a suppressed rate of spallation neutrons compared to an area lacking hydrogen, particularly in the epithermal range (0.5 eV $< E_n < 0.5$ MeV; Feldman et al., 1991).

As with radar measurements, a major limitation of this method is that it is not uniquely sensitive to the presence of water. Epithermal neutron counts will be suppressed due to a high concentration of any compound containing hydrogen. However, if neutron suppression regions correspond to areas where water can plausibly exist (i.e. within PSRs), then an argument can be made that the suppression is due to water rather than, for example,

hydroxyl.

A neutron spectrometer was included as part of the Lunar Prospector mission (Binder, 1998), which aimed to conduct a survey of the Moon's surface composition more generally. As seen in Fig. 1.1, the Lunar Prospector Neutron Spectrometer (LP-NS) did observe a significant suppression of epithermal neutron rates near the poles – 4.6% below the low-latitude average at the north pole and 3.0% at the south pole (Feldman et al., 1998). These data were interpreted as being consistent with water ice deposits buried approximately 40 centimetres below the surface. However, due to the low resolution of the LP-NS data (56–80 km per pixel; Maurice et al., 2004), it was not possible to definitively say that the PSRs were the source of the suppressed epithermal neutron rates.
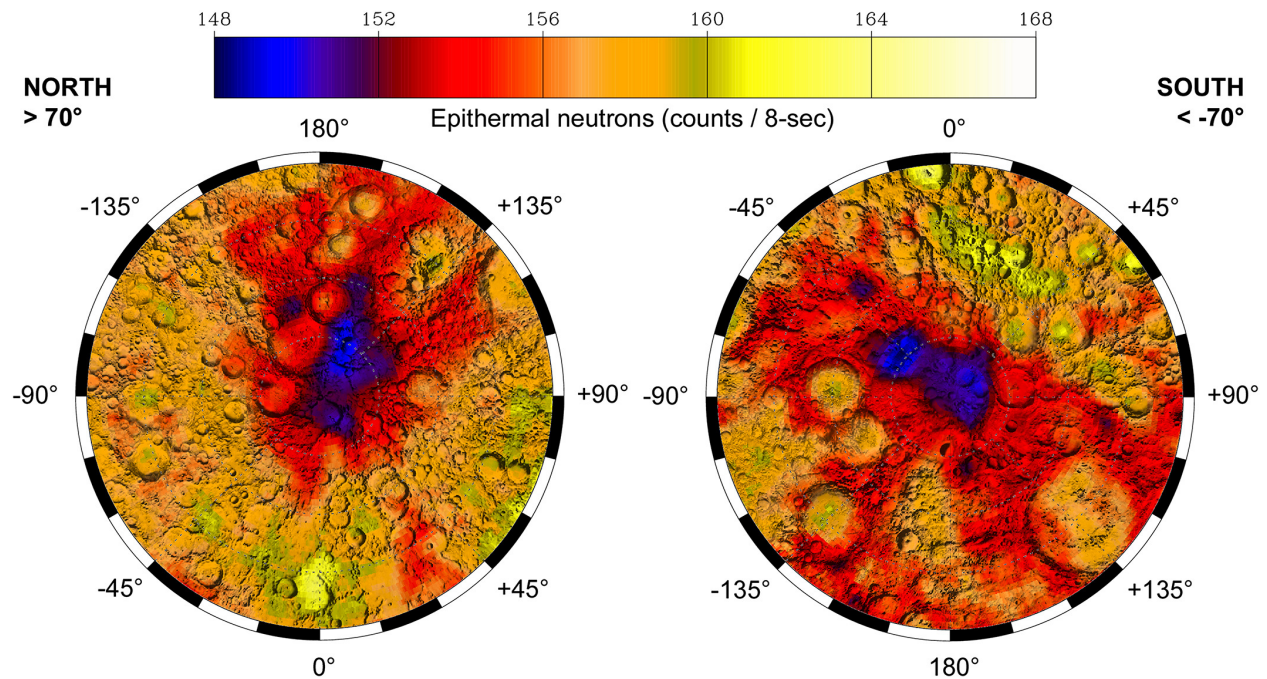
Figure 1.1: Reproduced from Lucey (2006): Epithermal neutron counts as measured by the Lunar Prospector Neutron Spectrometer. Regions of suppressed counts, indicative of enhanced hydrogen concentration, are obvious at both poles.

Results from LP-NS were later backed up by measurements made by the Lunar Exploration Neutron Detector (LEND; Mitrofanov et al., 2010) onboard LRO. LEND has improved spatial resolution relative to LP-NS (10 km per pixel; Mitrofanov et al., 2010), which allows

for a more convincing correlation to be made between neutron-suppressed regions and PSRs (See Fig. 1.2). From these measurements, it was estimated that several of the south polar PSRs (Cabeus, Haworth, and Shoemaker; see Fig. 1.3) contain water-equivalent hydrogen concentrations of up to 0.5% by weight, or about eight litres of water per cubic metre of regolith (Sanin et al., 2017).
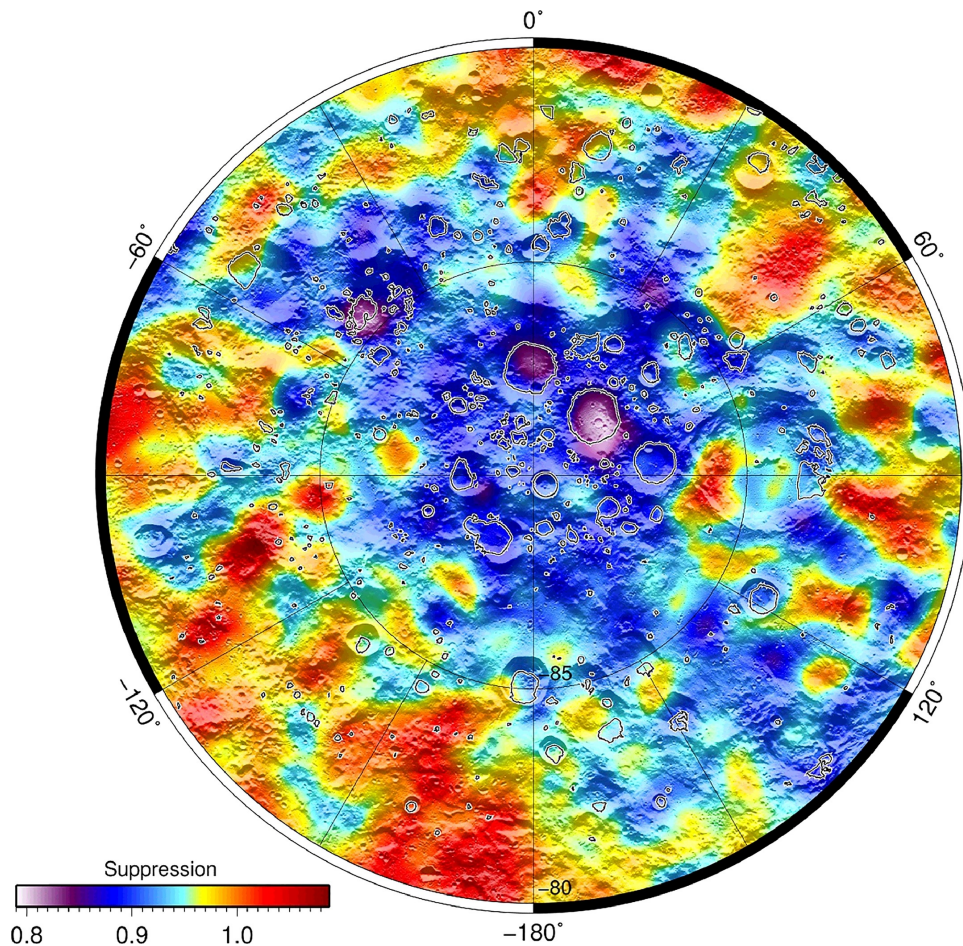
Figure 1.2: Reproduced from Sanin et al. (2017): Neutron suppression rates within 80° of the lunar south pole as measured by LEND. The higher resolution of these data as compared to those from LP-NS make it clear that the areas with the highest neutron suppression rates are generally coincident with PSRs (outlined in black), particularly those located in Cabeus, Haworth, and Shoemaker Craters. An additional notable neutron suppression region is located just outside of Nobile Crater, at the future VIPER landing site.
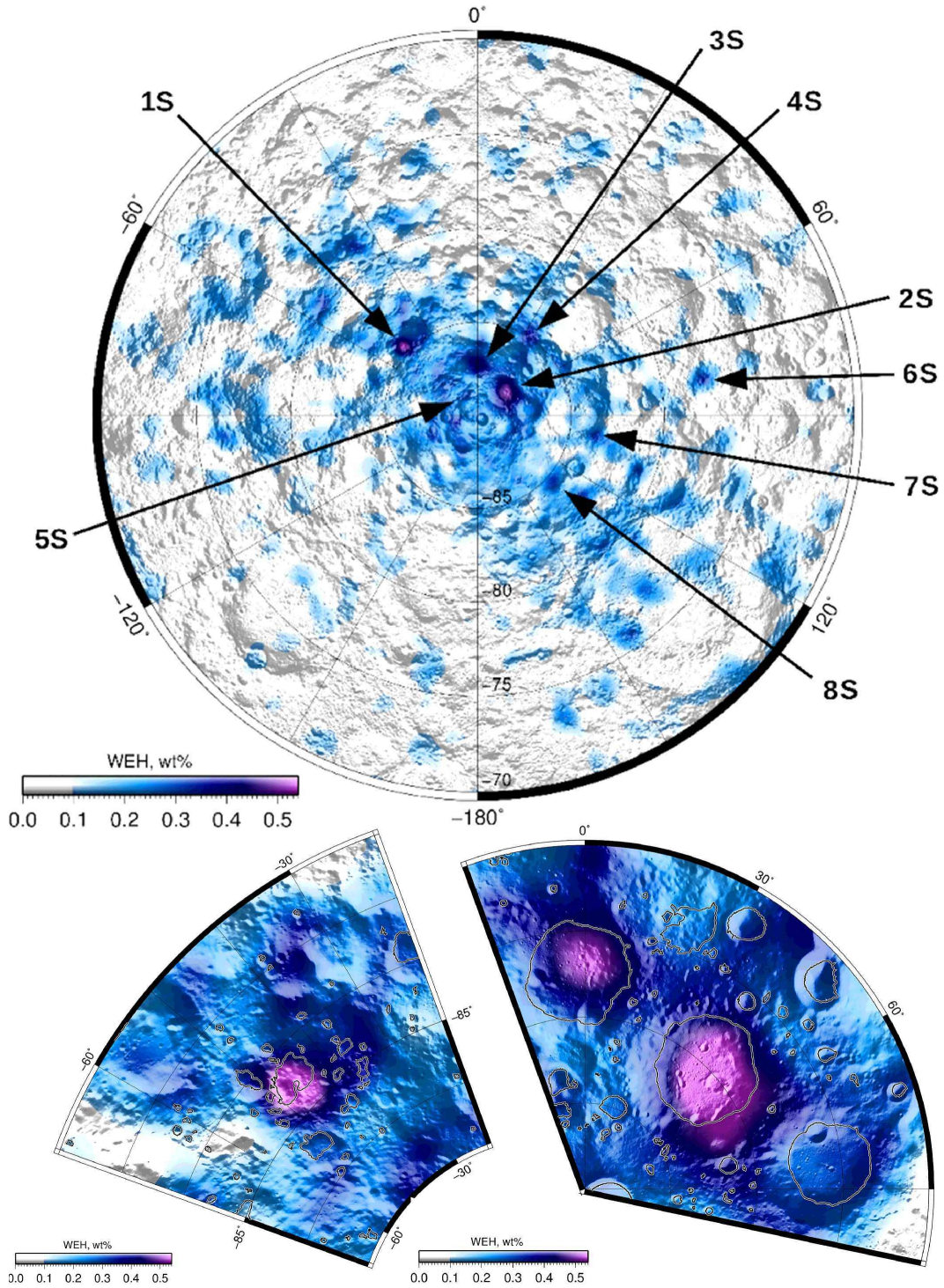
Figure 1.3: Reproduced from Sanin et al. (2017): Water-equivalent hydrogen (WEH) estimates out to 70° from the lunar south pole from LEND, with zoom-ins on Cabeus (left) and Faustini/Haworth/Shoemaker (right), showing the clear spatial correlation between WEH estimates and PSRs.

Of course, not everyone was willing to accept the LEND results at face value. In particular, Lawrence et al. (2010) and Lawrence et al. (2011) argued that the initial analysis of LEND data (Mitrofanov et al., 2010) did not sufficiently account for the background signal of uncollimated high-energy epithermal neutrons. Consequently, the data from hydrogen-enhanced PSRs would be contaminated by neutrons originating from illuminated terrain. If this is indeed the case, LEND would have a horizontal resolution of $50 - 75$ kilometres per pixel, rather than the $10 - 15$ kilometre per pixel resolution claimed by Mitrofanov et al. (2010), precluding the possibility of identifying hydrogen-enhanced regolith within specific PSRs. Despite vigorous debate between the original authors and others (e.g. Mitrofanov et al., 2011; Mitrofanov and Boynton, 2012; Boynton et al., 2012; Litvak et al., 2012; Eke et al., 2012; Miller, 2012a,b), no clear consensus has yet been formed regarding whether or not LEND achieved the spatial resolution claimed. Although the LEND results do make intuitive sense given what we know about water stability in PSRs, there certainly are legitimate reasons to doubt the precision of the data.

Direct Imaging

Central to this thesis is the fact that while PSRs are shielded from direct sunlight, they are not completely dark. They are subject to a number of alternate sources of illumination, including sunlight scattered off of nearby terrain, Earthshine, starlight, and Lyman-alpha photons from the interplanetary medium. Using these sources that contribute relatively little to directly-illuminated surfaces but that dominate the energy budget of PSRs, it may be possible to exploit the different reflective and absorptive properties of ice and lunar regolith in various wavelengths to directly image ice deposits.

The Japanese spacecraft Kaguya was the first to carry out reflectance measurements of a lunar PSR. Kaguya imaged the entirety of the Shackleton Crater PSR using its Terrain Camera, taking advantage of the weak indirect illumination provided by sunlight scattered off of the crater wall. No regions of anomalously-high albedo were observed, which would
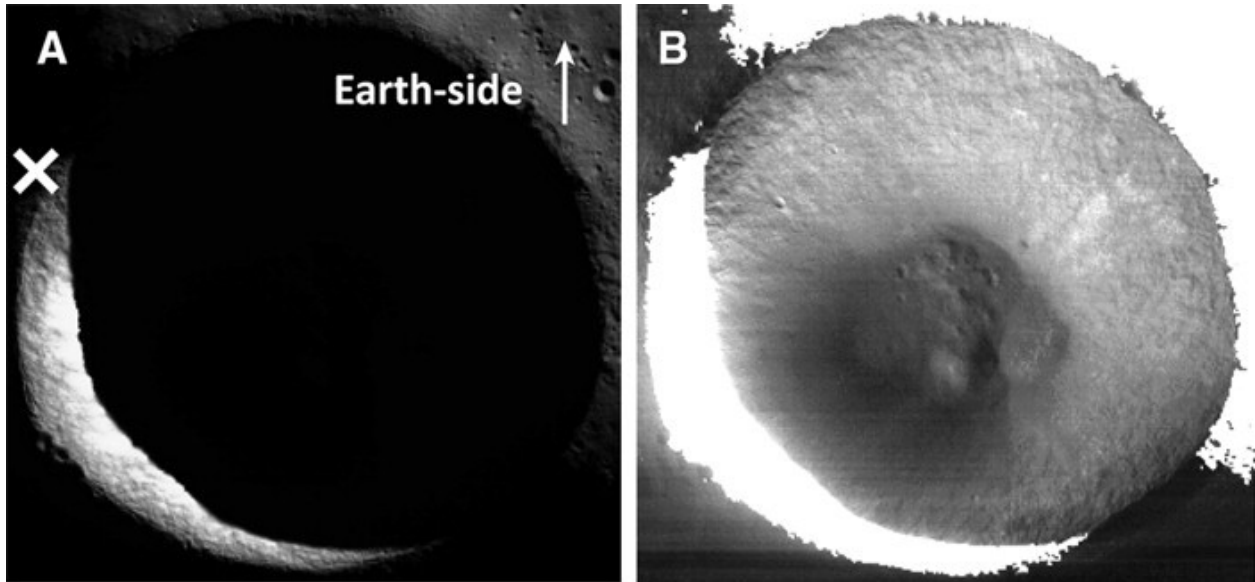
Figure 1.4: Reproduced from Haruyama et al. (2008): Images of the Shackleton PSR from Kaguya. On the left is the raw data, and on the right is the data stretched to enhance the scattered light illuminating the PSR.

have indicated the presence of surface-exposed water ice. The authors note that this doesn't necessarily mean that Shackleton contains no ice. Instead, any ice must be mixed with the regolith at concentrations of a few percent, as such a mixture would not have a strong effect on the observed albedo of the surface (Haruyama et al., 2008).

Since the arrival of the Lunar Reconnaissance Orbiter (LRO) at the Moon in June 2009, several of its instruments have made both active and passive reflectance measurements of PSRs in multiple wavelengths. In the visible, LRO's Narrow Angle Camera (LROC/NAC; Robinson et al., 2010) built on the work started by Kaguya by constructing long-exposure mosaics of as many PSRs as possible. Similar to what was observed at Shackleton, none of the PSRs observed by LROC seem to show any clear evidence for surface-exposed water ice, once again suggesting that any ice that does exist is likely mixed with the regolith (Koeber et al., 2014; Mitchell et al., 2016).

Although the primary scientific mission of LRO's Lunar Orbiter Laser Altimeter (LOLA; Smith et al., 2010) is to construct high-resolution digital elevation models (DEMs) of the lunar surface, it is also capable of measuring the difference in intensity between the laser

11

pulses it emits and the return pulse that is reflected from the surface. This allows it to actively probe the reflectivity of the surface at its operational wavelength of 1064 nanometres, in the near-infrared. Zuber et al. (2012) and Lucey et al. (2014) found that PSRs are systematically brighter at this wavelength than illuminated terrain. Focusing on Shackleton, Zuber et al. (2012) concluded that the brightness difference was primarily due to mass wasting on the crater walls (downward movement of vacuum-exposed regolith that exposes the younger, brighter regolith beneath) and decreased space weathering (bombardment of micrometeorites and solar wind that darkens the regolith by producing iron and dark glass) of the crater floor relative to illuminated surfaces, though they point out that a micron-thick layer of 22% ice mixed with the regolith is also sufficient to explain their results. Lucey et al. (2014) controlled for mass wasting effects and found that PSRs are still systematically brighter than illuminated terrain, attributing the difference to either 3-14% frost/ice by weight or significantly reduced space weathering. Haruyama et al. (2013) refuted these concentrations as inconsistent with spectral data from Kaguya, which suggested that brightness anomalies in Shackleton are more plausibly caused by anorthosite deposits rather than water ice.

The final LRO instrument that has made reflectance measurements of lunar PSRs is the Lyman Alpha Mapping Project (LAMP; Gladstone et al., 2010). LAMP images PSRs using solar Lyman-α photons scattered by the interplanetary medium as well as those from UV-bright stars. Using LAMP data, Gladstone et al. (2012) found that PSRs are both darker in the FUV generally and more reflective at the longest FUV wavelengths than illuminated terrain. They attribute the darkness to PSR soils having larger porosities (a measure of how much of a rock's total volume is occupied by void space rather than mineral grains) than their illuminated counterparts, and the increased reflectivity to 1-2% water frost by area.

Hayne et al. (2015) combined LAMP reflectance measurements with surface temperatures from the Diviner Lunar Radiometer to see if the supposed frost-related anomalous reflectance features occur in areas where water ice can be stable. If they are located in regions that are insufficiently cold for ice to resist sublimation, then alternate explanations must be

found. Hayne et al. (2015) found that as the surface temperature decreases, LAMP observes a decreasing Lyman-α and on-band (129.57-155.57 nm) albedo and an increasing off-band (155.57-189.57 nm) albedo, all of which are consistent with the presence of at least 100 nm of water ice. Based on their modeling, these results imply ice concentrations of 0.1-2% by mass or 10% by area. They note that the potential distribution of water is highly heterogeneous – some PSRs (i.e. Haworth) show strong UV signals consistent with water while others (i.e. Shackleton) show none. Their data also show two peaks: one at 110 K, suggestive of water ice; and another at 65 K, suggestive of carbon dioxide ice. Alternately, the peaks could indicate deposits of two different ages, with the 110 K peak being an older deposit driven towards the surface by subsurface temperature gradients and the 65 K peak being a younger deposit that has not yet been mixed into the subsurface by impact gardening.

Perhaps the most provocative evidence for the presence of lunar volatiles came from the Moon Mineralogy Mapper (M³; Green et al., 2011), a NASA-led instrument onboard India's Chandrayaan-1 spacecraft. M³ was an imaging spectrometer that operated in the near-infrared (NIR) with the primary goal of creating high resolution maps of the Moon's mineral resources. The wavelength range over which M³ operated allowed for the observation of three absorption features that arise from the vibrational modes of water ice molecules. This means that unlike the other datasets we have discussed so far, the M³ data are able to differentiate between water ice and other hydrogen-bearing compounds, as well as between water ice and water that is adsorbed to the surface or in the form of hydrated minerals. M³ found that approximately 3.5% of lunar PSR pixels have these spectral features consistent with the presence of surface-exposed water ice. The ice-bearing pixels correlate well with data from the various LRO instruments, with nearly all having Diviner maximum temperatures below 110 K, anomalously high LOLA reflectances, and high LAMP on/off band ratios (Li et al., 2018).
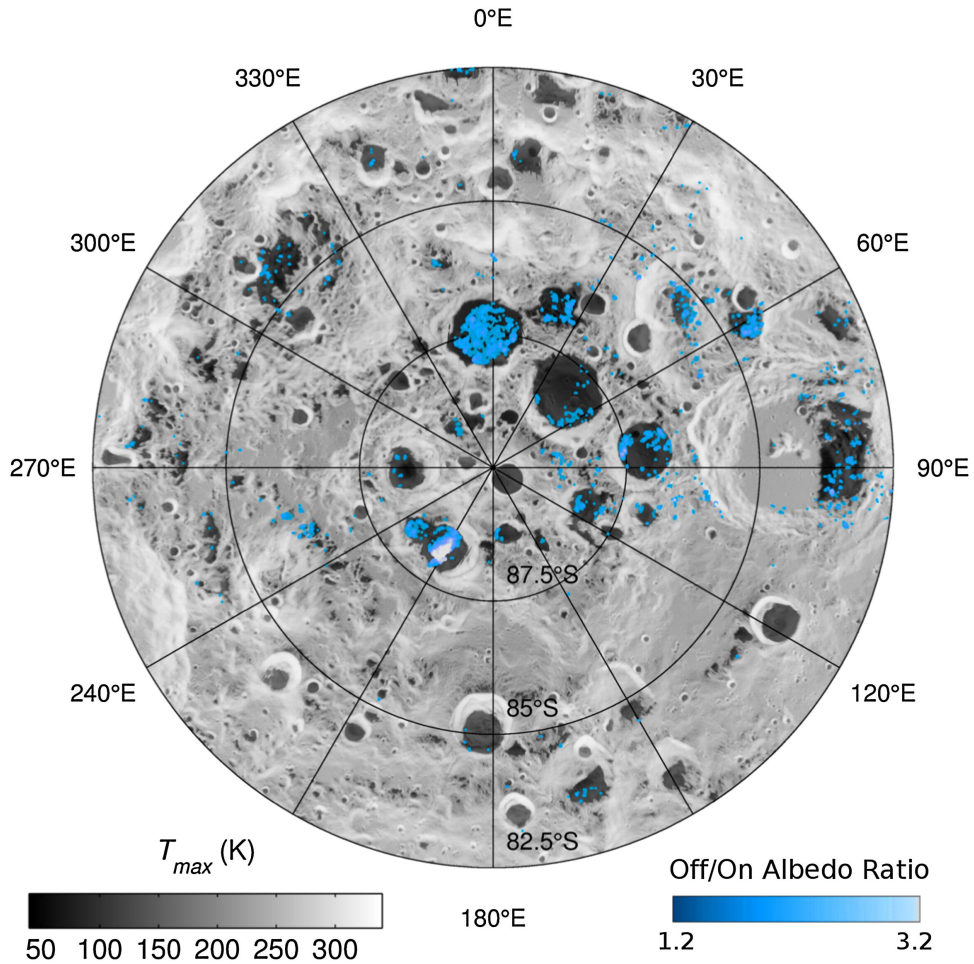
Figure 1.5: Reproduced from Hayne et al. (2015): LAMP measurements consistent with the presence of water ice.

In-situ Measurements

To date, there has only been a single measurement directly confirming the existence of volatile materials within a lunar PSR. This measurement was performed by the Lunar Crater Observation and Sensing Satellite (LCROSS), which accompanied LRO to the Moon. The goal of the LCROSS mission was to use the fuel-depleted upper stage of the Centaur launch vehicle as a kinetic impactor to kick up material from within a PSR. The mission's Shepherding Spacecraft, which contained the instrument payload, would then fly through the resulting plume to perform a spectral analysis of its contents.

Impact occurred on October 9, 2009, in the Cabeus Crater PSR. Cabeus was chosen as the
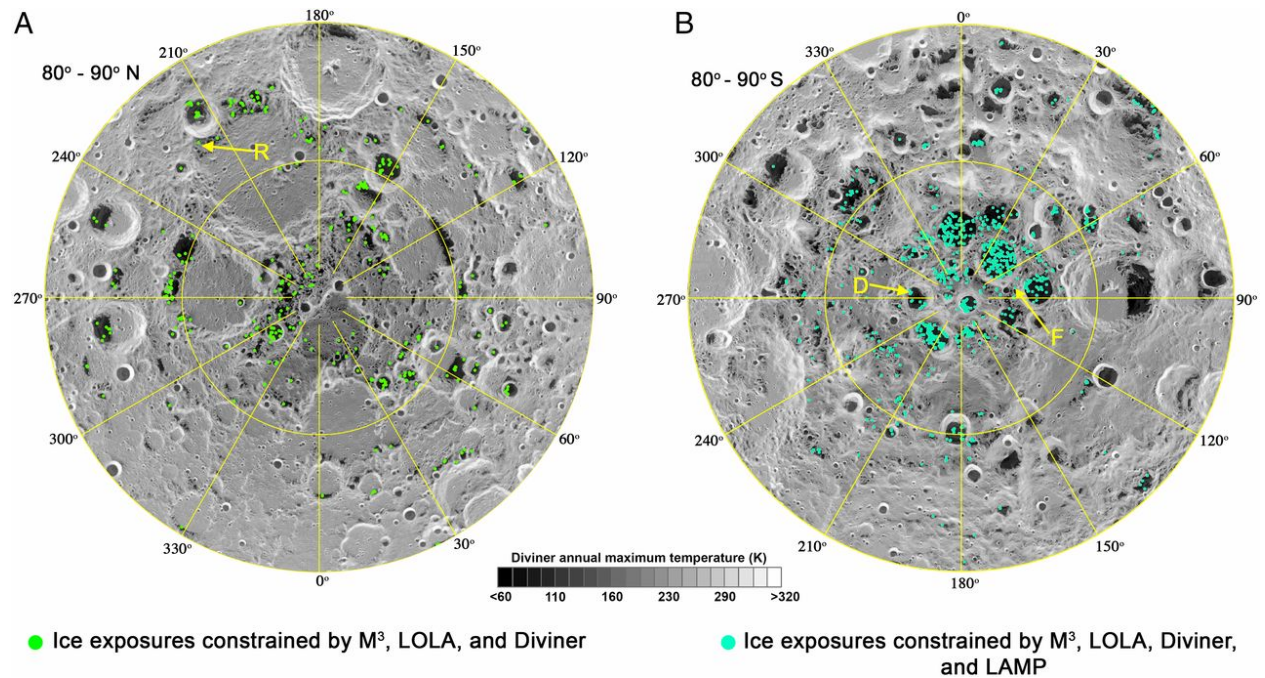
Figure 1.6: Reproduced from Li et al. (2018): Likely locations of surface-exposed water ice at both of the Moon's poles as constrained by data from M³, LOLA, Diviner, and LAMP.

target because data from Kaguya, Chandrayaan-1, and LRO all indicated ideal conditions for water ice stability (see Fig. 1.7 for a context temperature map). Though the impact plume was not as visually stunning as had been predicted, the Shepherding Spacecraft successfully gathered its data, directly confirming the presence of water ice on the lunar surface for the first time, along with a number of other volatile species. A list of the major detected species along with their abundances relative to water can be seen in Table 1.1.
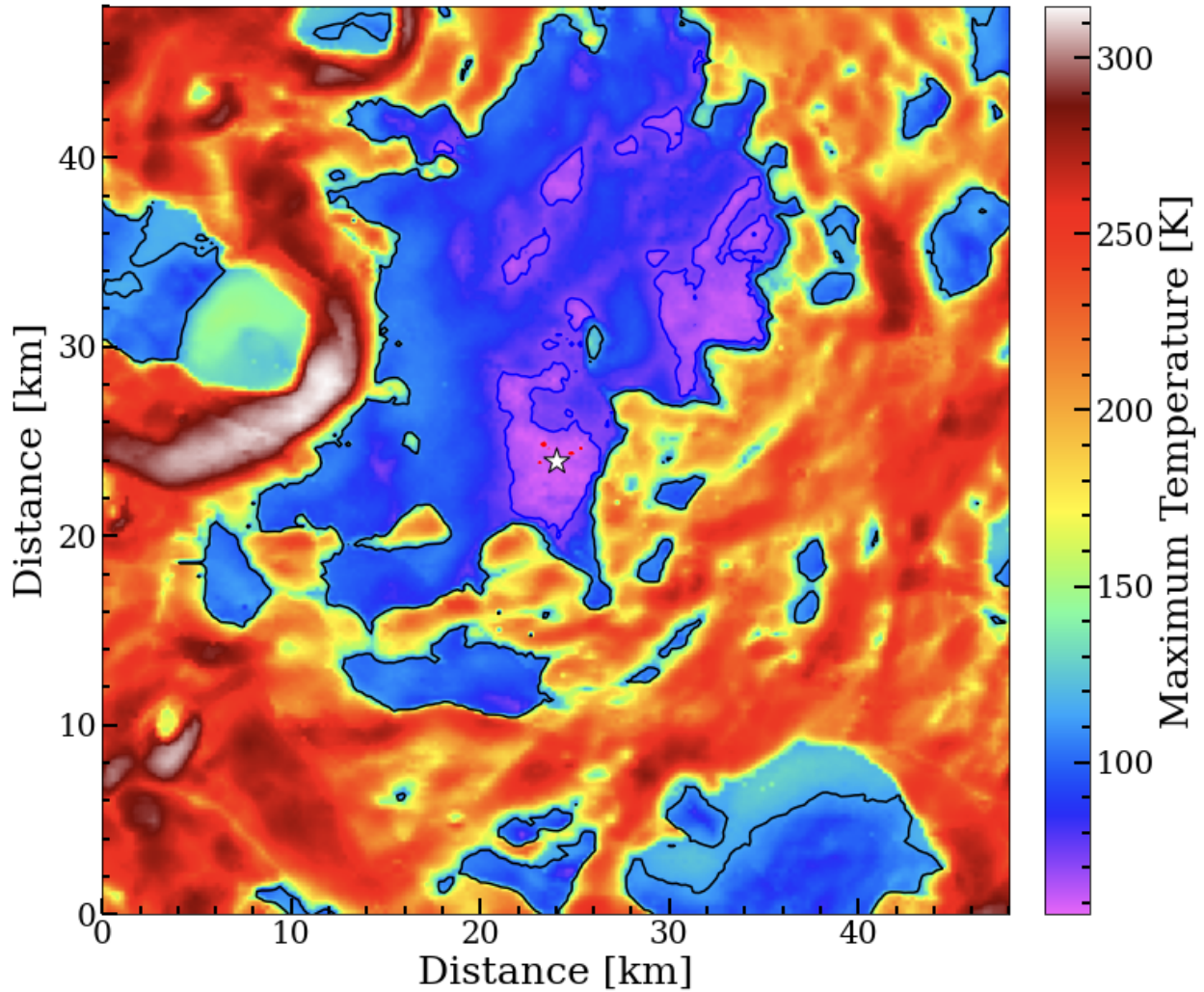
Figure 1.7: Maximum summer temperatures in the vicinity of the LCROSS impact site (marked with a white star) as measured by Diviner. The black, blue, and red contour lines mark the stability thresholds of water, ammonia, and carbon dioxide, respectively, illustrating the particularly cold temperatures prevalent in this region.

1.1.2 Motivation: The Importance of Small-Scale Terrain

The major shortcoming of existing orbital datasets is their relatively low resolution. Due to practical limitations on data volume, one can either have high-resolution data covering a small area (e.g. the Apollo landing sites), or lower-resolution global data. Diviner and

LOLA polar data products are binned at 240 metres per pixel, a resolution that is sufficient for global studies but averages over a lot of fine detail at smaller scales. Figure 1.8 illustrates this problem using an Earth-based DEM. Downsampling the high-resolution data preserves the general shape of the terrain, but the features responsible for the most significant changes in local illumination conditions are completely lost.
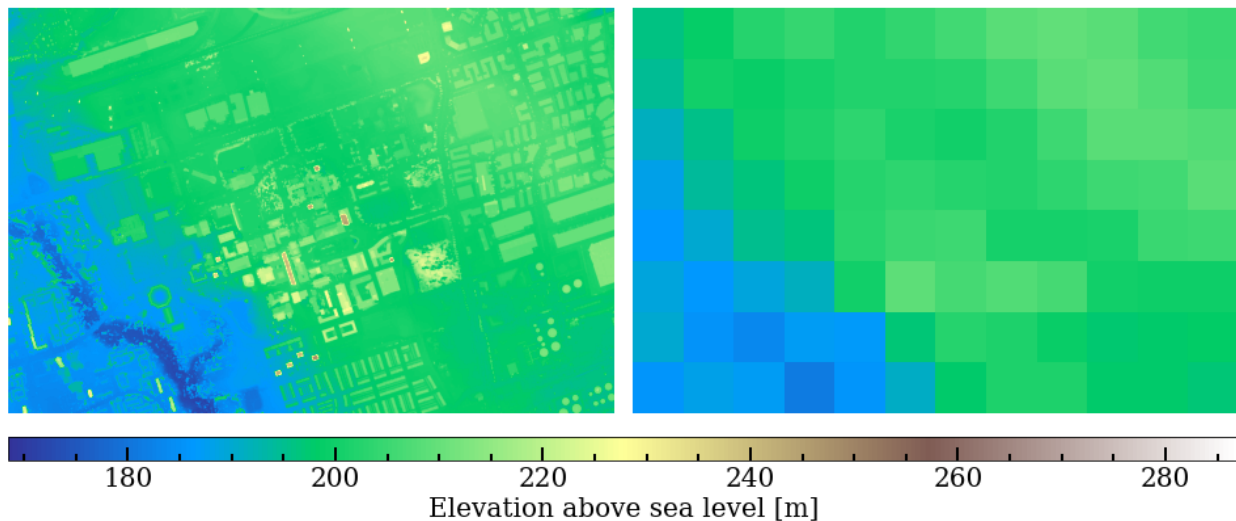
Figure 1.8: A DEM of the York University area produced by the Government of Ontario (left) and downsampled to match the LOLA resolution (right). General features are preserved in the downsampled data but the fine detail is lost, illustrating why higher-resolution data are necessary when using DEMs to conduct illumination studies.

Compound	Molecules cm^{-2}	% Relative to H_2O (g)
H_2O	$(5.1 \pm 1.4) \times 10^{19}$	100.0
H_2S	$(8.5 \pm 0.9) \times 10^{18}$	16.75
NH_3	$(3.1 \pm 1.5) \times 10^{18}$	6.03
SO_2	$(1.6 \pm 0.4) \times 10^{18}$	3.19
C_2H_4	$(1.6 \pm 1.7) \times 10^{18}$	3.12
CO_2	$(1.1 \pm 1.0) \times 10^{18}$	2.17
CH_3OH	$(7.8 \pm 42) \times 10^{17}$	1.55
CH_4	$(3.3 \pm 3.0) \times 10^{17}$	0.65
OH	$(1.7 \pm 0.4) \times 10^{16}$	0.03

Table 1.1: Abundances of various compounds detected in the LCROSS impact plume (Colaprete et al., 2010).

The magnitude of this effect on the Moon has been demonstrated by Hayne et al. (2021), who conducted temperature modeling on Gaussian rough surfaces representative of the terrain outside of PSRs. They found that small-scale terrain features create "micro cold traps" – small regions of otherwise sunlit terrain that are permanently shadowed by surface roughness effects, and thus are cold enough to contain volatiles. These micro cold traps can exist down to a scale of ~ 1 cm, at which point lateral heat conduction tends to overwhelm the effects of shadowing. As a result of their analysis Hayne et al. (2021) conclude that the Moon's cold-trapping area could be $10 - 20\%$ larger than previous estimates using lower resolution illumination models and temperature data.

The goal of the lunar section of this thesis is to conduct a preliminary examination of the effect that small-scale terrain features have on temperature conditions within the PSRs themselves. Much like how subpixel surface roughness creates small areas of permanent shadow outside of PSRs, there may be similarly small areas within PSRs that are shielded from both direct sunlight and the singly-scattered sunlight that LROC exploited to create its PSR mosaics. Lacking the two primary sources of illumination on the lunar surface, these areas could be significantly colder than the temperatures measured by Diviner, expanding the area available for the cold-trapping of non-water volatiles.

To complete this analysis, we will be modeling the singly-scattered sunlight and thermal emissions incident upon a realistic rough terrain derived by upscaling a terrain map of the LCROSS impact site created using Lunar Orbiter Laser Altimeter (LOLA) data. The incident fluxes will be run through a thermal model to convert them into temperatures. Our focus will be on the LCROSS impact site because it provides a unique opportunity for us to connect the observed volatile abundances in the impact plume with the fractional subpixel area available for the cold-trapping of each observed species. By comparing the two values, we can make inferences about the horizontal and vertical distribution of the volatile deposits present before the impact occurred.
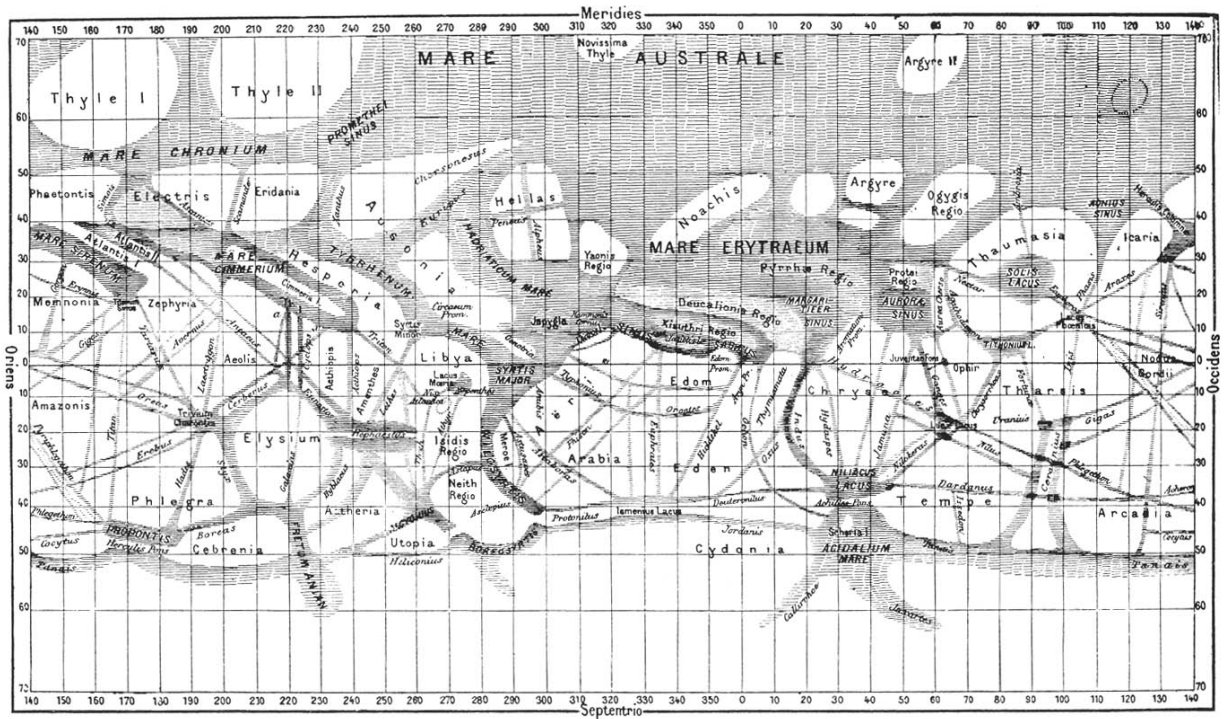
Figure 1.9: Reproduced from Ezell and Ezell (1984): A map of the Martian surface as observed by Giovanni Schiaparelli in the late 19th century.

1.2 Searching for Water on Mars

As Mars is much more distant from Earth than the Moon, it has had a more storied history of theories involving water on its surface. Early telescopic observations by Giovanni Cassini, William Herschel, and others in the 17th and 18th century revealed the presence of clouds and polar ice caps that grew and shrank with the seasons, implying that Mars had an atmosphere that contained at least some amount of water (Cassini, 1666; Herschel, 1784).

The first detailed maps of the Martian surface were compiled by Giovanni Schiaparelli during Mars' 1877 opposition. His maps (seen in Fig. 1.9) included a number of linear features, which he dubbed (in Italian) *canali*. Although this term does not refer to artificial canals, it was often translated as such, leading to a proliferation of theories about the presence of intelligent life on Mars.

These theories were popularized by Percival Lowell, who founded the still-extant Lowell

Observatory to study the supposed canals. Lowell produced his own maps (Fig. 1.10) and fanciful stories to accompany them, in which he discusses a civilization on a rapidly-drying planet building canals from the polar ice caps to provide water to cities in the equatorial regions (Lowell, 1895, 1906, 1908).

Although they never gained serious traction among the wider scientific community, Lowell's theories of a Martian civilization became increasingly implausible as more evidence emerged that Mars' atmosphere is very much unlike Earth's, with a surface pressure approximately 1% that at terrestrial sea level and a composition that is dominated ($\sim 95\%$) by carbon dioxide with only a small amount ($\sim 0.2\%$) of oxygen (Williams, 2020). Any remaining doubts were finally erased by the arrival of the Viking spacecraft in the 1970s, which relayed back images of a desolate and arid planet, completely devoid of visible liquid water or signs of intelligent civilization (either present or past).

It is now well-established that Mars has no persistent surficial water at the present day, though this almost certainly was not the case in the geologically recent past. Despite modern conditions being hostile to the existence of liquid water, Mars does still have an active water cycle that is driven by the seasonal heating and cooling of the atmosphere. During each winter, temperatures in the polar regions become sufficiently cold that the water vapour in the atmosphere is forced to condense, forming large polar ice caps. As the atmosphere warms back up in the spring, the polar caps sublimate, releasing their water back into the atmosphere, where it plays an important role in the climate through the formation of water-ice clouds (WICs). Though they are generally optically thin, Martian WICs have been shown to have a measurable impact on Mars' radiative balance through the reflection of incoming solar radiation and the absorption and re-emission of infrared radiation from the surface (Richardson et al., 2002; Hinson and Wilson, 2004; Montmessin et al., 2004; Wilson et al., 2007). To properly develop models of the Martian climate, we must understand how these clouds interact with the light incident upon them.

North Pole.   South Pole

$\lambda = 0°$. $\lambda = 90°$.

$\lambda = 180°$.   Lowell Observatory Photographs of Mars in 1909. $\lambda = 270°$.
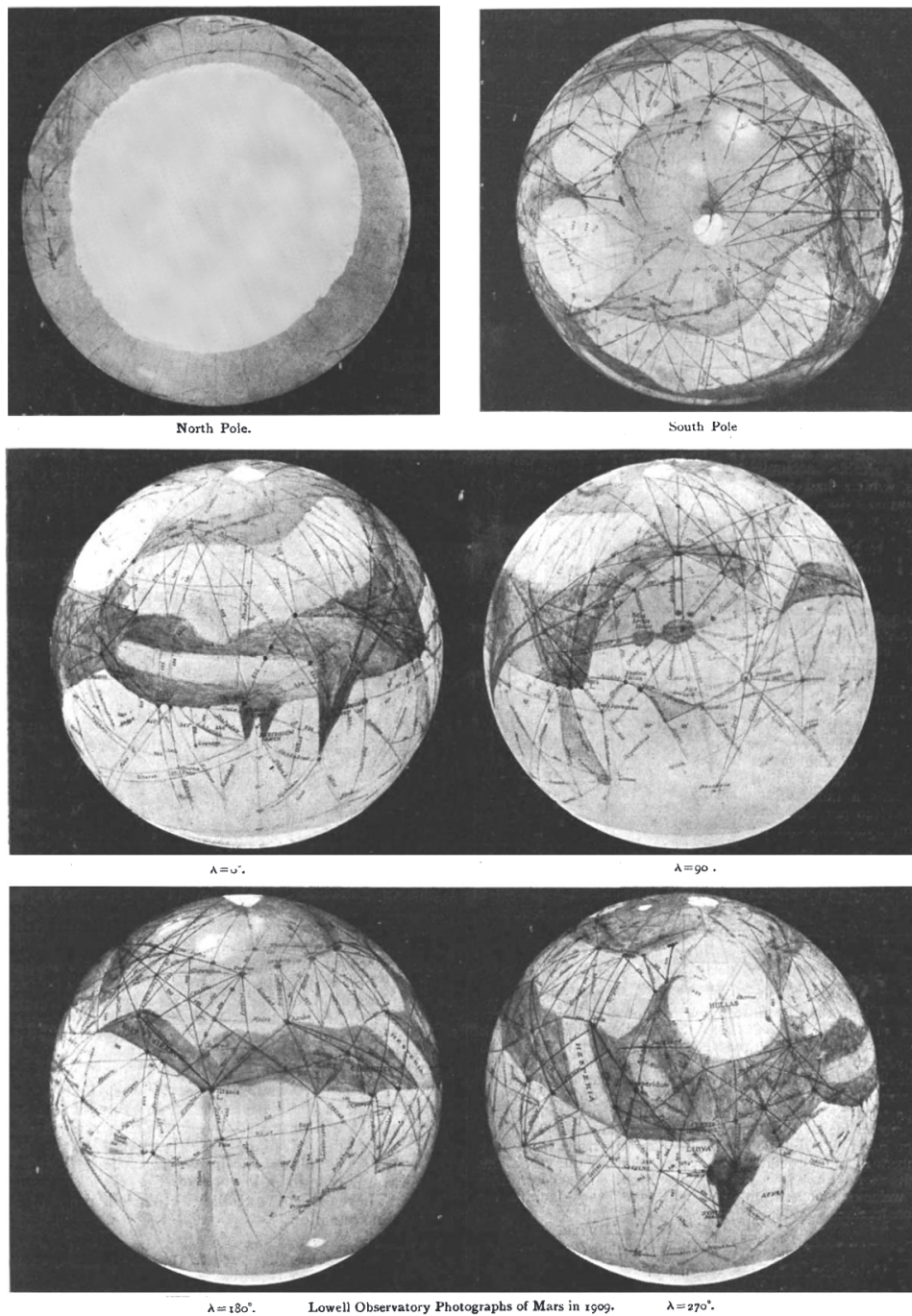
Figure 1.10: Reproduced from Lowell (1910): Lowell's maps of Martian "canals".

1.2.1 The Aphelion Cloud Belt

The Martian climate is dominated by the competing seasonal effects of the planet's comparatively high orbital eccentricity (0.0935) and Earth-like obliquity (26.19°). As on Earth, Mars' obliquity creates seasons in each hemisphere due to the changing maximum incidence angle of the Sun on the surface. Unlike Earth, the seasons in the northern versus southern hemisphere because Mars' orbital eccentricity takes the planet $\sim 20\%$ closer to the Sun at perihelion than at aphelion. The resulting difference in solar insolation drives atmospheric processes that divide the Martian year into two halves: the perihelion dusty season and the aphelion cloudy season. The individual and combined effects of the planet's eccentricity and obliquity can be seen in Fig. 1.12 for a latitude of 4.6°S (corresponding to the landing site of the Mars Science Laboratory Curiosity rover). In Fig. 1.11 we illustrate the peak solar irradiance during one Martian year for all latitudes.
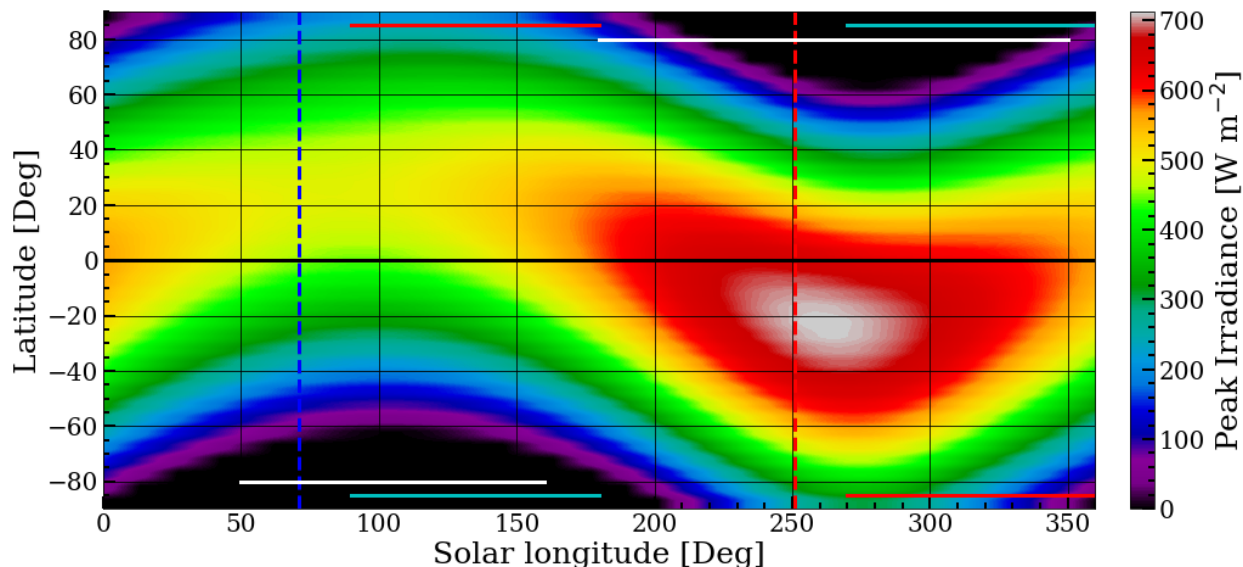
Figure 1.11: Peak irradiance of the Martian surface (ignoring the attenuating effects of that atmosphere) as a function of latitude and solar longitude. The blue and red dashed lines represent aphelion and perihelion, respectively. The red and cyan lines represent the summer and winter periods in each hemisphere. The white lines denote the aphelion cloudy season and the perihelion dusty season. The competing seasonal effects of Mars' axial tilt and orbital eccentricity are clearly visible, with the southern hemisphere experiencing much higher peak irradiances than the northern hemisphere during its summer. The MSL Curiosity rover landed at a latitude of 4.6° S; a plot for that latitude can be seen in Fig. 1.12.
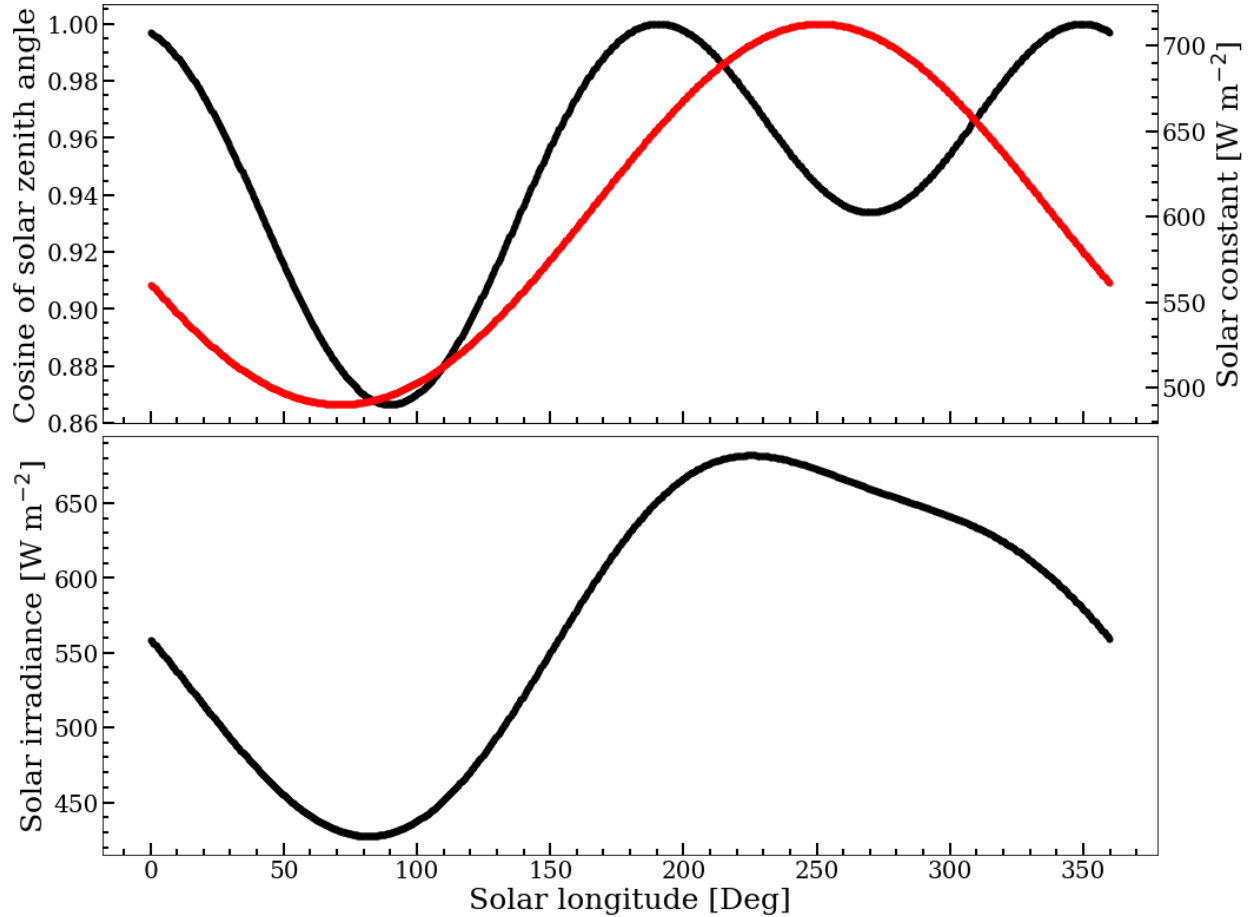
Figure 1.12: Top panel: In black is the cosine of the solar zenith angle at local noon, which changes as the subsolar point moves with the seasons. In red is the approximate value of the solar constant due to Mars' orbital eccentricity. Bottom panel: The combined effect of the two components in the top panel, showing how the peak irradiance of the surface (ignoring the atmosphere) changes dramatically over the course of the year.

Mars reaches aphelion at a solar longitude (L_s) of 71°, shortly before the northern summer equinox. During this time, the north polar ice cap is sublimating due to increased near-surface temperatures. Simultaneously, the lower atmosphere is cooling down, as the solar insolation received at the top of the Martian atmosphere is $\sim 70\%$ of that received at perihelion. The combination of higher atmospheric water vapour concentration and lower atmospheric temperature means that the air quickly becomes saturated. When that occurs, the water vapour condenses into a belt of water-ice clouds that surround the planet's equatorial latitudes, appropriately named the Aphelion Cloud Belt (ACB; Wolff et al., 1999).

The discovery of the ACB upended the widely-held belief from the Viking era that WICs played a negligible role in the Martian climate (Tamppari et al., 2003). It is now understood that those observations were taken during a period that was unusually dusty, and that understanding the ACB is an important part of understanding the dynamics of the Martian atmosphere as a whole (Clancy et al., 1996).
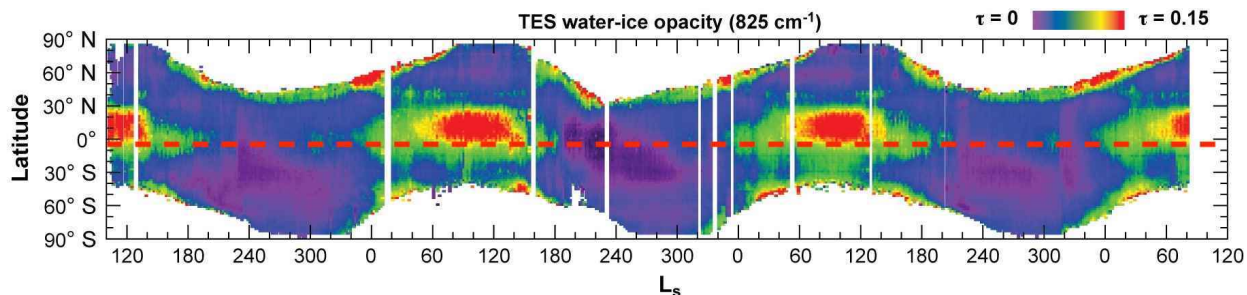
Figure 1.13: Reproduced from Smith (2008): TES observations of water-ice opacities over three MYs. The ACB is the red blob that appears each year, centred around 10°N and $L_s = 100°$. We have added the dashed red line at the latitude of the MSL landing site, illustrating how the rover can view the southern edge of the ACB.

1.2.2 Motivation

MSL Observations of the ACB

Although the thickness of the ACB peaks around 10°N, the equatorial latitude of the Mars Science Laboratory (MSL) Curiosity rover's landing site ($\sim 4.6°$S) allows for observations of the southern edge of the ACB to be conducted from the ground. For this purpose, MSL has been undertaking a cloud observation campaign since sol 24 (see Fig. 3.1). This campaign has produced numerous and varied results, including records of cloud opacities and spacing (Moores et al., 2015; Kloos et al., 2016, 2018), wind direction and angular velocity (Campbell et al., 2022), cloud altitudes (Campbell et al., 2020), and the scattering phase function (Cooper et al., 2019; Innanen et al., 2021, 2022).

The work to be presented in the second half of this thesis was motivated by a combination of results from MSL's cloud observation campaign. Specifically, the opacities presented by

Moores et al. (2015), Kloos et al. (2016), and Kloos et al. (2018) were all calculated under the assumption that Martian WICs have a constant, flat phase function, fixed at a value of 1/15. However, Cooper et al. (2019), Innanen et al. (2021), and Innanen et al. (2022) have all found that this assumption is only valid beyond a certain scattering angle; closer to the Sun, the phase function deviates significantly from the flat assumption. Although the cloud movies that make up the bulk of the observation campaign are specifically intended to look away from the Sun, operational constraints result in their occasional execution outside of their ideal timing windows. When that happens, we observe clouds at scattering angles where the phase function is apparently not flat, invalidating the assumptions made in our model. Consequently, we became interested in examining the extent to which this breakdown affects our opacity results by taking advantage of the known low interannual variability of the ACB (Tamppari et al., 2003; Liu et al., 2003; Smith, 2004; Hale et al., 2011) to determine our own phase function.

As previously noted, the results presented herein are not the first time that a phase function for Martian WICs has been determined from MSL observations. For the past three ACB seasons, MSL has implemented a Phase Function Sky Survey observation (PFSS), which consists of nine three-frame movies forming a dome around the rover. This observation has allowed us to obtain near-simultaneous measurements of the phase function of WICs present over Gale Crater over a wide range of scattering angles.

If MSL-derived phase functions already exist, one may justifiably ask why we are deriving our own rather than using the PFSS results. One major limitation of the PFSS is that the phase function is derived using an equation originally developed by Moores et al. (2015) and Kloos et al. (2016) for measuring cloud opacities (see Sec. 3.1.3 for more detail). As a result, the cloud opacities are required as an input, creating a "chicken and the egg" problem – the phase function calculation needs the cloud opacities, but we cannot determine the cloud opacities without already having the phase function.

The PFSS cannot make this assumption (as doing so would defeat the entire purpose of

the observation), so cloud opacities measured from MSL can't be used without developing an entirely new radiative transfer model. Instead, water-ice column depths from the Mars Climate Sounder (MCS) taken in the vicinity of Gale Crater and averaged over 10° of solar longitude are assumed to be representative of the cloud opacities present at the time the PFSS is executed.

The usage of MCS data is potentially problematic for several reasons. First, MCS has difficulty retrieving values near the surface due to increased dust opacity in the lower atmosphere, with the water-ice column depths often limited to an altitude of 30 km. The clouds we observe over Gale Crater are frequently lower than that (Campbell et al., 2021), so MCS may not be observing the same clouds. Indeed, we know that MCS and MSL are not observing exactly the same clouds, since the MCS measurements are not taken simultaneously with the PFSS. Even if the two spacecraft are observing the same *type* of cloud (which, again, is not necessarily the case), not every cloud of the same type is exactly identical. Second, the Mars Reconnaisance Orbiter (MRO), to which MCS is mounted, is in a Sun-synchronous orbit, meaning that it observes each part of the surface at the same time each day. We know that cloud opacities vary over the course of the day (Kloos et al., 2018), so the MCS data are almost certainly not capturing this detail. Finally, the footprint of MCS measurements is quite large, with typical nadir observations having a horizontal resolution of 1-6 kilometres (Hayne et al., 2012).

Importance of the Phase Function

Determining a scattering phase function for Martian WICs is an exercise that has consequences beyond our opacity calculations. As previously mentioned, WICs play an important role in the Martian climate, despite their low optical depths at visible wavelengths. WICs on Mars can be most directly compared to terrestrial cirrus clouds, as both are created by the deposition of water ice onto cloud condensation nuclei in similar temperature and pressure conditions (Petrosyan et al., 2011). It is known that the presence of cirrus clouds on Earth

results in a net warming effect of the atmosphere (Hong et al., 2016; Yu et al., 2018), and there is ample evidence that the same is true on Mars (e.g. Wilson et al., 2007; Wilson and Guzewich, 2014; Lee et al., 2018; Cooper et al., 2021; Bischof et al., 2022).

Although Martian WICs clearly do have an effect on the climate, we do not yet understand the microphysics underlying their interaction with incoming solar radiation and IR emissions radiating from the ground. Consequently, global climate models (GCMs) of Mars can have difficulty replicating observations even when WICs are included. In their investigation into the impact of terrestrial cirrus clouds on solar radiative fluxes, Schlimme et al. (2005) found that the most important properties governing the interaction of clouds with light are (in order) optical thickness, ice crystal geometry, particle size, and the macrophysical cloud structure. Determining the shape of the scattering phase function allows us to directly probe two of these properties (ice crystal geometry and particle size) and indirectly probe optical depth. Thus, constraining the shape of the phase function of Martian WICs can assist in the work of climate modelers who currently assume that they are composed of spherical ice crystals (Clancy et al., 2003; Wolff et al., 2009).

Chapter 2

Lunar Micro Ultra-Cold Traps

2.1 Methods

2.1.1 Terrain Upscaling

Our terrain generation begins with the digital elevation models (DEMs) produced by the Lunar Orbiter Laser Altimeter (LOLA). LOLA measurements are taken using a Q-switched Nd:YAG laser operating at a wavelength of 1064 nm. Each laser pulse produced by the instrument passes through a diffractive optical element, which splits the pulse into a five-beam X-pattern, with each beam spaced approximately 0.5 milliradians apart (12 metres on the ground from a nominal orbit of 50 kilometres). The time of flight for each beam is measured and used to produce high-resolution maps of surface topography, roughness, and reflectance (Smith et al., 2010).

The LOLA data products that we are interested in for this work are the gridded polar elevation maps, shown in Fig. 2.1. These maps were created by interpolating the binned elevation data at a resolution of 240 metres per pixel (true at the pole), a resolution that was chosen as it represented the best compromise between having high accuracy and requiring low computational resources (Mazarico et al., 2011). The maps use a polar stereographic projection and extend to 75° from each of the poles.
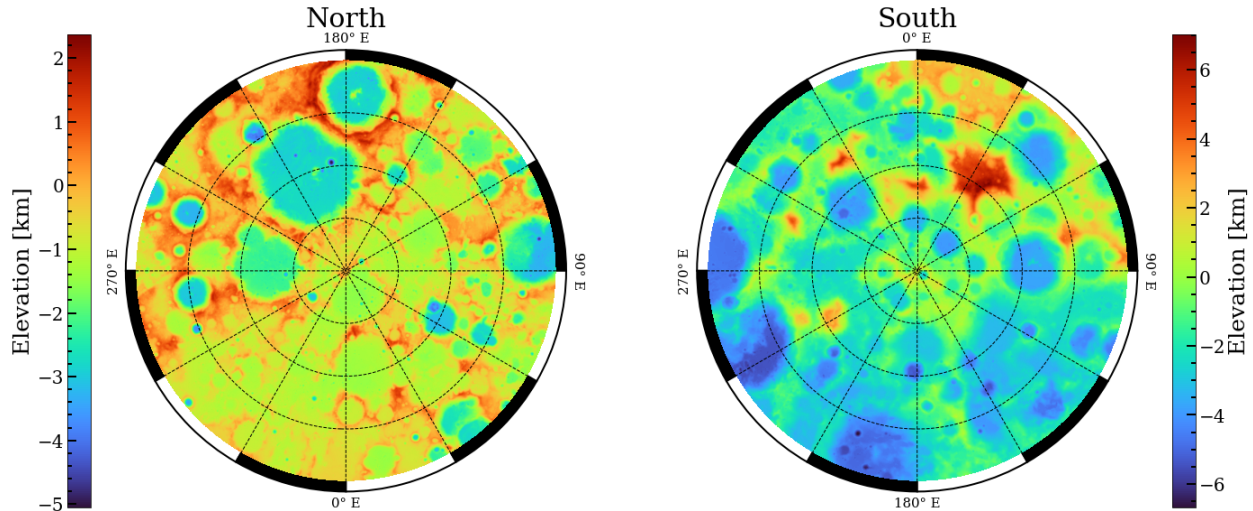
Figure 2.1: LOLA digital elevation models for each of the Moon's polar regions. The elevation is with reference to a sphere of radius 1737.4 km (note the different scales for each pole). Each map is centred on the pole and uses a polar stereographic projection. Lines of latitude are shown every 2.5°.

To begin the upscaling process, we select an 11-by-11 pixel region around our point of interest. Once again, this size is chosen as a compromise between accuracy and computational efficiency. We then interpolate the region to our desired resolution (1 metre per pixel) using bivariate splines. Because splines create smooth curves, the resulting terrain is not representative of real-world conditions, as planetary surfaces are not perfectly smooth. The surface of airless bodies like the Moon are often modeled as random rough terrain with a Gaussian distribution of heights and slopes (e.g. Bandfield et al., 2015; Davidsson et al., 2015; Rubanenko and Aharonson, 2017; Davidsson and Hosseini, 2021). These surfaces are usually characterized by the root-mean-square (RMS) slope, σ_s, which describes the vertical magnitude of the roughness; and the Hurst exponent ($0 < H < 1$), which laterally scales the roughness. In keeping with this practice, we add roughness to our upscaled terrain by overlaying it with a Gaussian surface.

The surface is generated by seeding a matrix of the same size as the upscaled terrain with a random Gaussian field with a zero mean and unitary standard deviation. Using a 2D Fast Fourier Transform (FFT), we find the field's power spectral density (PSD), which is then

scaled by the Hurst exponent. Because we want to create a surface that is representative of the conditions that one could plausibly find on the Moon, the value of the Hurst exponent is set to 0.95, consistent with what previous studies have measured using LROC and LOLA data (Rosenburg et al., 2011; Cai and Fa, 2020) for the lunar highlands. We note that Rosenburg et al. (2011) found that the Hurst exponent is often lower (~ 0.7) within large craters, which could impact our final results (see Fig. 2.3). This effect seems to be less prevalent in the south polar region, particularly in those craters containing PSRs (incuding Cabeus), so we argue that our use of $H = 0.95$ is justified. The PSD is then filtered to remove short and long wavelength features that are inconsistent with lunar terrain. Finally, the PSD is transformed back into a terrain map using an inverse FFT and then vertically scaled to match our target RMS slope.

Selecting the target RMS slope is more challenging as its value depends on the baseline scale over which it is calculated. In general, roughness appears to increase with decreasing scale. At decametre scales, LOLA has measured median slopes between $2°$ in the maria and $7.5°$ in the highlands (Rosenburg et al., 2011). Stereophotogrammetry of Apollo imagery has suggested that the RMS slope on submillimetre to decimetre scales is much larger, averaging around $25°$ (Helfenstein and Shepard, 1999). This is backed up by Bandfield et al. (2015) who found that brightness temperature differences between Diviner's thermal channels are best explained by a Gaussian surface with a sub-millimetre RMS slope of 20–$35°$. Using high-resolution DEMs constructed from LROC NAC imagery, Cai and Fa (2020) found that the mean value of the bidirectional slope at metre-scales ranges from $3.4°$ and $8.2°$ between the maria and highlands, with observed values as small as $1.8°$ and as large as $22.2°$. With such a wide range of observed values, we choose to model our surface with an intermediate RMS slope of $15°$.

The values chosen here for both the Hurst exponent and the RMS slope will ultimately drive the rest of our results, as they determine the shape of the small-scale terrain features that will create micro ultra-cold traps. In Fig. 2.3, we show how varying both of these

30
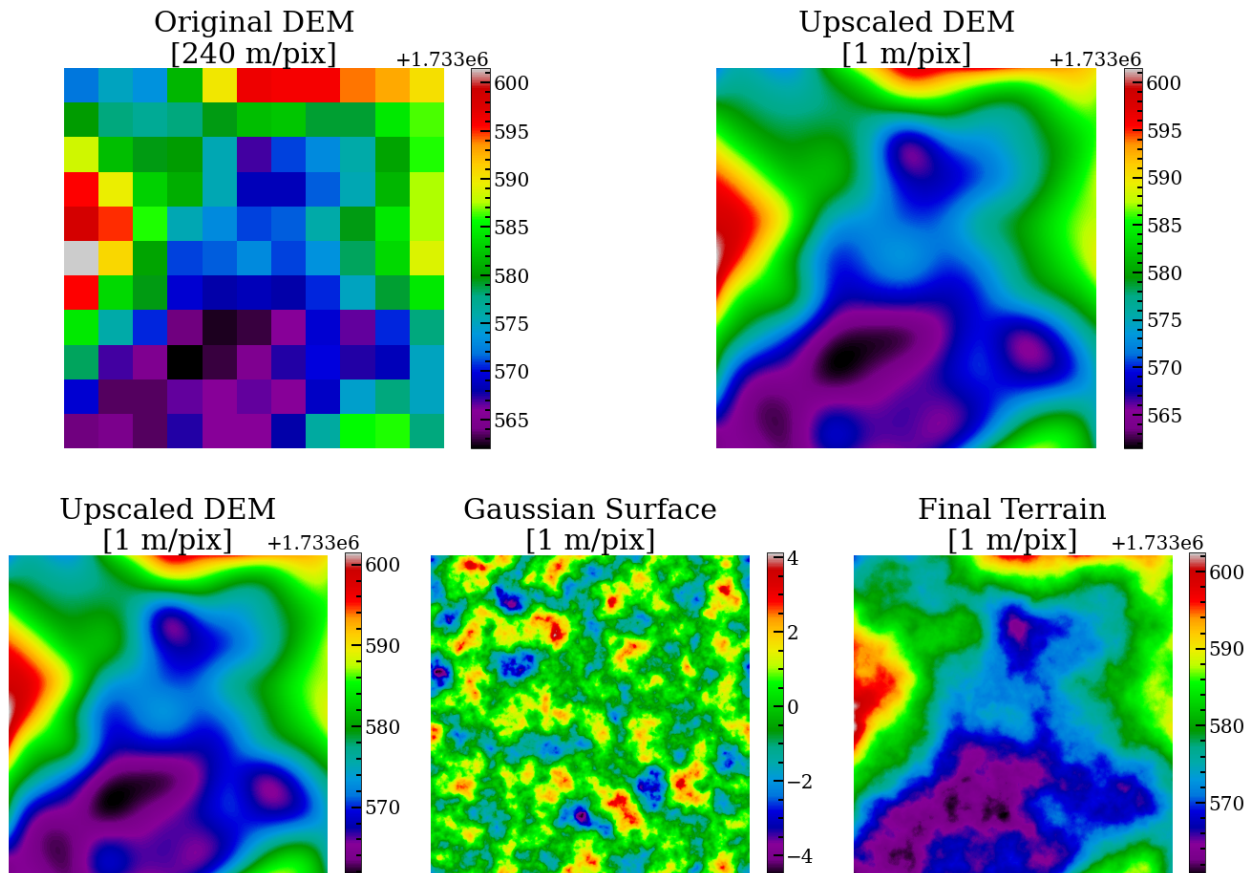
Figure 2.2: An overview of the upscaling process. The top two panels show the original LOLA DEM (left) and the spline-interpolated terrain (left). The bottom three panels show the interpolated terrain (left), Gaussian surface (centre), and interpolated terrain with the Gaussian overlay (right).

parameters changes the resulting surface. Increasing the RMS slope increases the vertical scale of the roughness, increasing the extent to which the low-lying regions are shielded from indirect illumination. Reducing the Hurst exponent shrinks the horizontal scale of the roughness, which would create smaller doubly-shadowed regions.
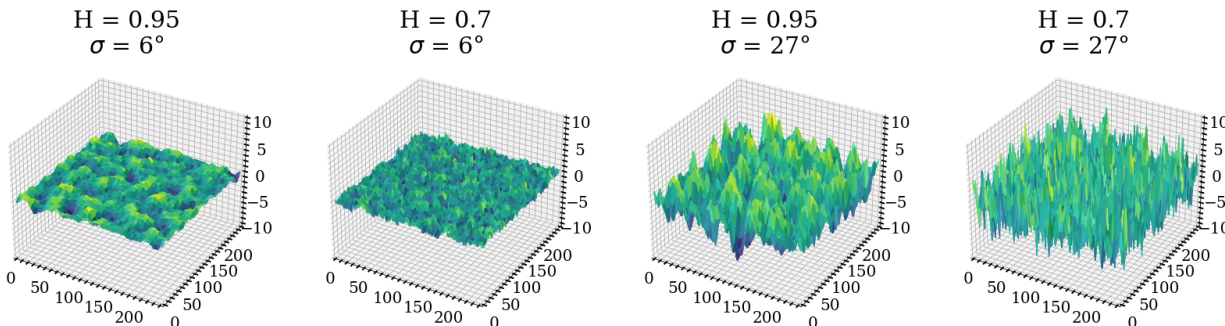
Figure 2.3: Four Gaussian surfaces created by varying the values of the RMS slope and Hurst exponent. In broad terms, the RMS slope controls the vertical scale of the surface's roughness while the Hurst exponent controls the horizontal scale. The values of both will ultimately determine how much of the surface is subject to indirect illumination.

2.1.2 Terrain Illumination

Determining the illumination conditions experienced by a terrain facet at a particular time is a purely geometric exercise. The amount of light scattered by a terrain facet k towards another facet j is a function of four vectors (the solar incident vector at k, the surface normals at k and j, and the vector between the two facets) and the angles between them. A schematic illustration of these terms is shown in Fig. 2.4.

Of these terms, only two are time-dependent: the solar incident vector and the angle that it makes with the light-scattering terrain normal. Consequently, all of the other (time-independent) terms can be combined into a single value known as the *view factor*:

$$F_{k \to j} = \frac{v_{jk} s_k \cos i_j \cos e}{\pi d^2}$$

where v_{jk} is a *visibility factor* (1 if the facets have a direct line of sight, 0 if they are obscured
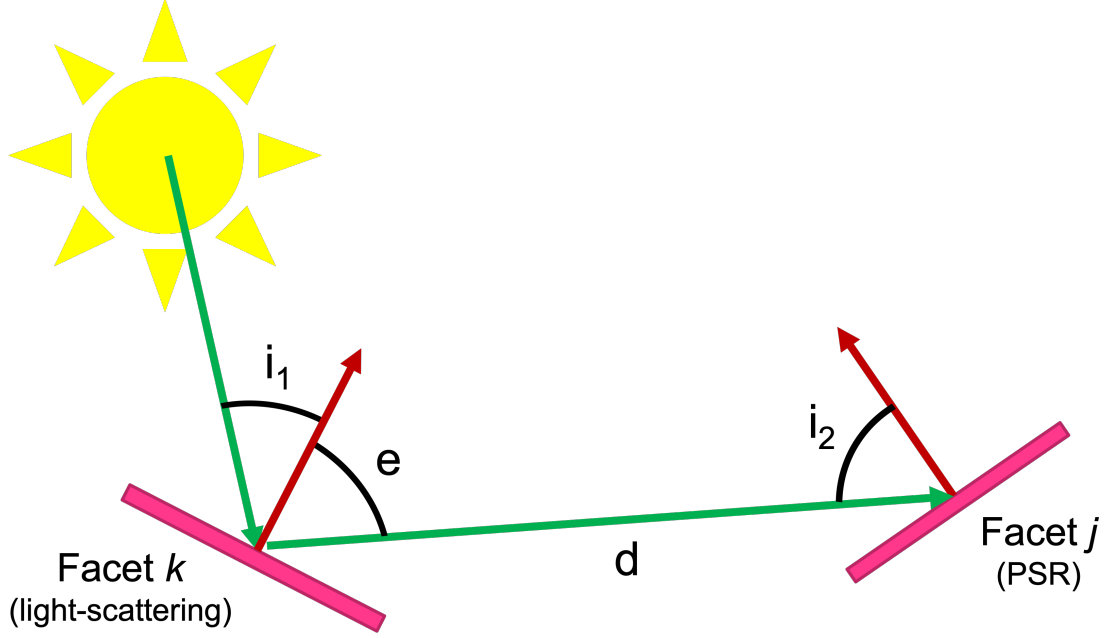
Figure 2.4: A 2D illustration of the vectors and angles involved in calculating the illumination conditions.

by terrain or self-shadowing) and s_k is the surface area of k. See Fig. 2.5 for an illustration of how the viewing geometry impacts the viewfactor value.

Assuming Lambertian scattering, the total scattered flux received by j (summed across all light-scattering terrain facets) is then:

$$\sum_k S_0 V_\odot F_{k\to j} A_k \cos i_k$$

Here, S_0 is the solar constant (1361 W m^{-2}) and $V_\odot$ is the visible fraction of the solar disc.

Similarly, the thermal self-heating incident at j can be described as:

$$\sum_k \epsilon \sigma T_k^4 F_{k\to j}$$

with ϵ being the emissivity, σ being the Stefan-Boltzmann constant, and T_k being the temperature of each of the light-scattering terrain facets.

33
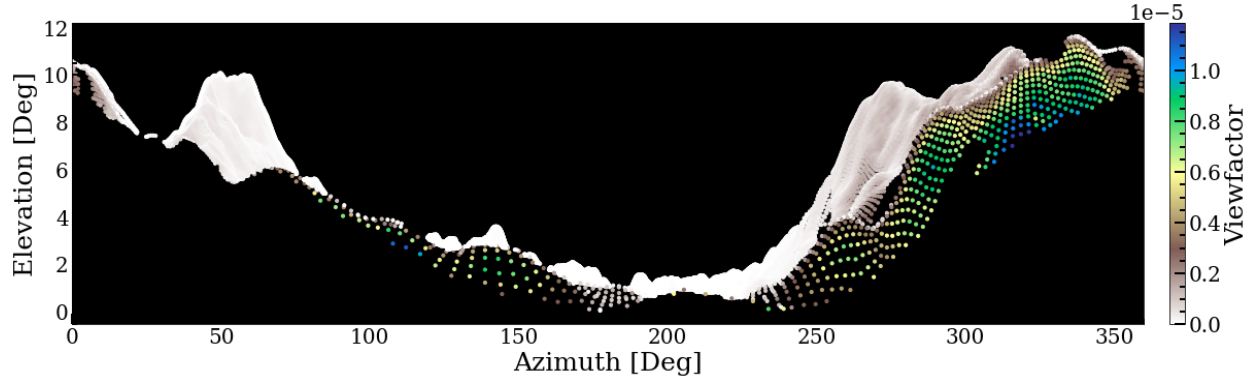
Figure 2.5: A 3D illustration of the light-scattering terrain points visible from the LCROSS impact site, coloured by the value of the viewfactor at each point. This visualization makes it clear how the viewfactor depends on distance (closer points have higher values) and the relative angle between the terrain facets (facets facing "towards" each other have higher values).

Directly-Illuminated Terrain

To determine which terrain points are capable of scattering light into the PSRs, we use the light-scattering terrain maps created by Kloos et al. (2021). An example of one of these maps for Haworth Crater is shown in Fig. 2.6. Note that these maps indicate those terrain elements visible from *at least one point* within the PSR. We will still need to determine whether a line-of-sight exists from each point we examine; these maps serve to reduce the number of calculations that must be performed for each point.

For each point in the light-scattering terrain, we must find i_k and $V_\odot$. i_k depends on the location of the Sun in the sky at each point, as well as the angle that the solar incident vector makes with the surface normal. To locate the Sun, we first determine the coordinates of the subsolar point using the DE421 lunar ephemeris (Williams et al., 2008). The altitude
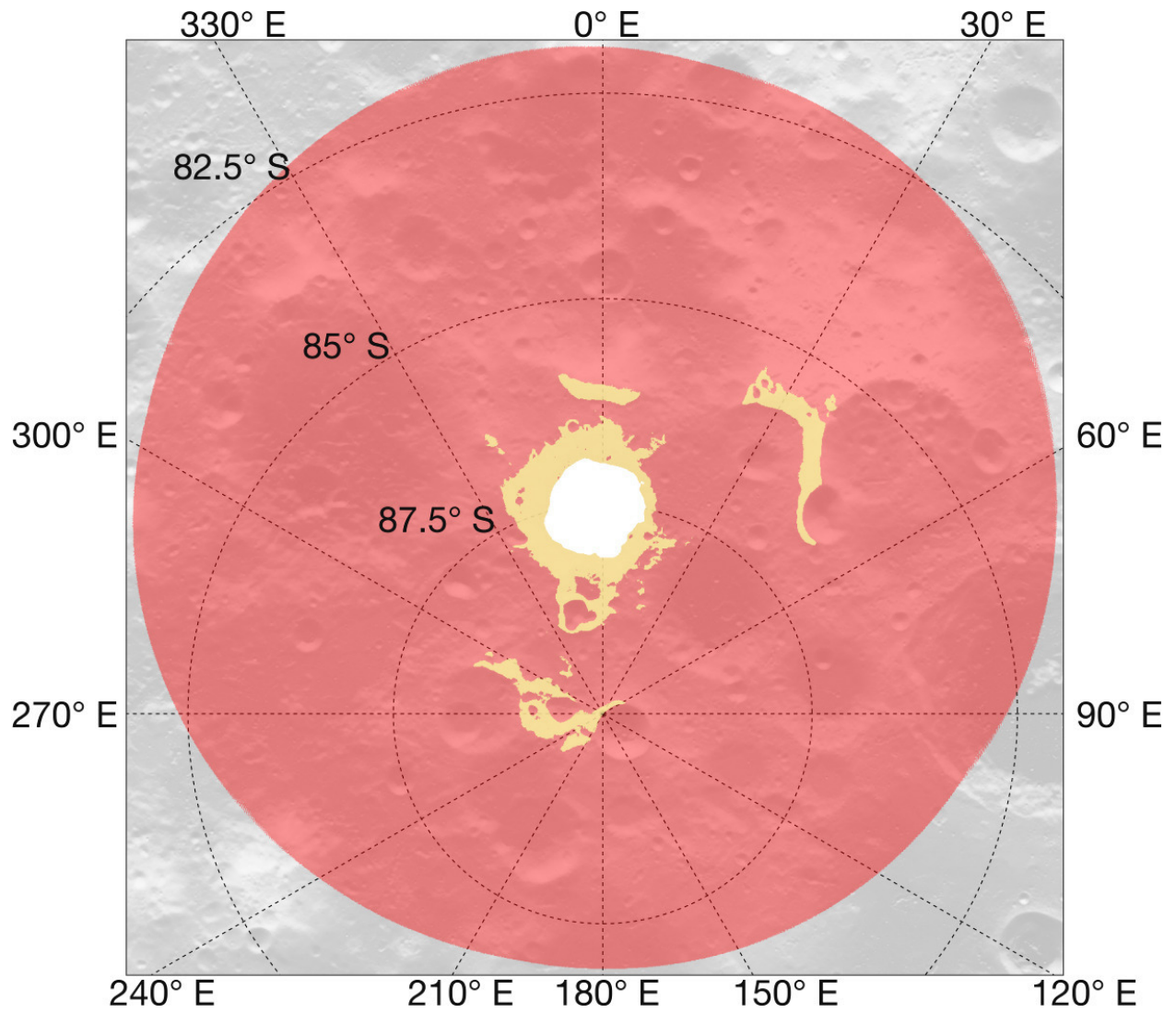
Figure 2.6: Reproduced from Kloos et al. (2021): A light-scattering terrain map for Haworth Crater. The irregular white shape at the centre is the PSR itself, and the light-scattering terrain is indicated in yellow. The red circle indicates the region that was searched for visibility.

and azimuth of the Sun from a point at $(\text{Lat}, \text{Lon}) = (\theta, \phi)$ is then:

$$sx = \cos\theta_{subsol}\sin\left(\phi_{subsol} - \phi\right)$$

$$sy = \cos\theta\sin\theta_{subsol} - \sin\theta\cos\theta_{subsol}\cos\left(\phi_{subsol} - \phi\right)$$

$$sz = \sin\theta\sin\theta_{subsol} + \cos\theta\cos\theta_{subsol}\cos\left(\phi_{subsol} - \phi\right)$$

$$\text{alt} = \frac{\pi}{4} - \arccos sz$$

$$\text{az} = \left(\arctan\frac{sx}{sy}\right) \mod 2\pi$$

The surface normal vectors can then get defined using LOLA-derived maps of terrain slope and aspect angles. The slope angle defines how "steep" the terrain is at a point, with $0°$ indicating a completely horizontal slope and $90°$ indicating a completely vertical slope. The aspect angle defines the direction in which the slope is facing, with $0°$ being a north-facing slope and $180°$ being a south-facing slope. Combined, these two angles create a vector normal to the surface in polar coordinates. i_k is then the angle between the surface normal and the solar position vector.

To determine $V_\odot$, we use the horizons method (Mazarico et al., 2011, See Fig. 2.7). From each point, we project 360 evenly-spaced 150 kilometre-long rays along the LOLA topography and calculate the elevation angles along the array using vector geometry, assuming the Moon is a perfect sphere with a radius of 1737.4 km. The maximum elevation angle defines the height of the horizon in that direction. We then linearly interpolate between each of these points to create a horizon map.

At each timestep, we compare the location of the Sun to the horizon map. The Sun is modeled as an extended source with an angular diameter of $0.5°$, though we do not take into account limb darkening. If the centre of the Sun is more than $0.25°$ above or below the horizon, then $V_\odot$ is set to 1 or 0, respectively. If the centre of the Sun is within $0.25°$ of the horizon, then we assume the horizon is locally flat and horizontal and remove the area of the
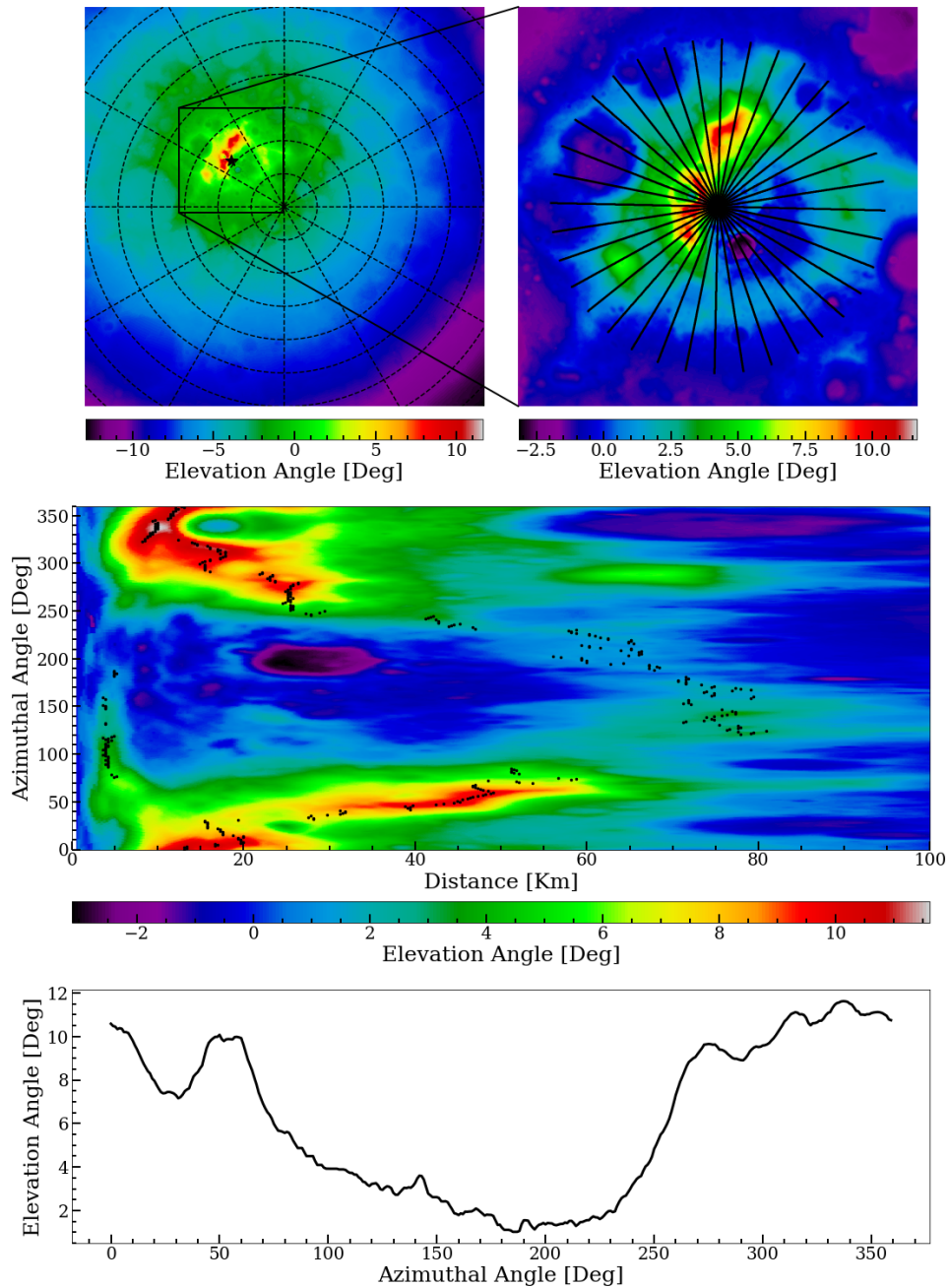
Figure 2.7: The horizons method of Mazarico et al. (2011). Beginning at the top left, we see the elevation angle of each point in the south polar DEM relative to the LCROSS impact site (marked with a black star). At the top left is a zoom-in on the region marked with a black square. Here, several line-of-sight rays are projected across the terrain. For clarity, only 360 of the 360 rays are shown. In the middle panel, we see the elevation angle profile across each of the LOS rays. The black points mark the location of the maximum angle in each direction. At the bottom is the horizon extracted from the maximum elevation points.
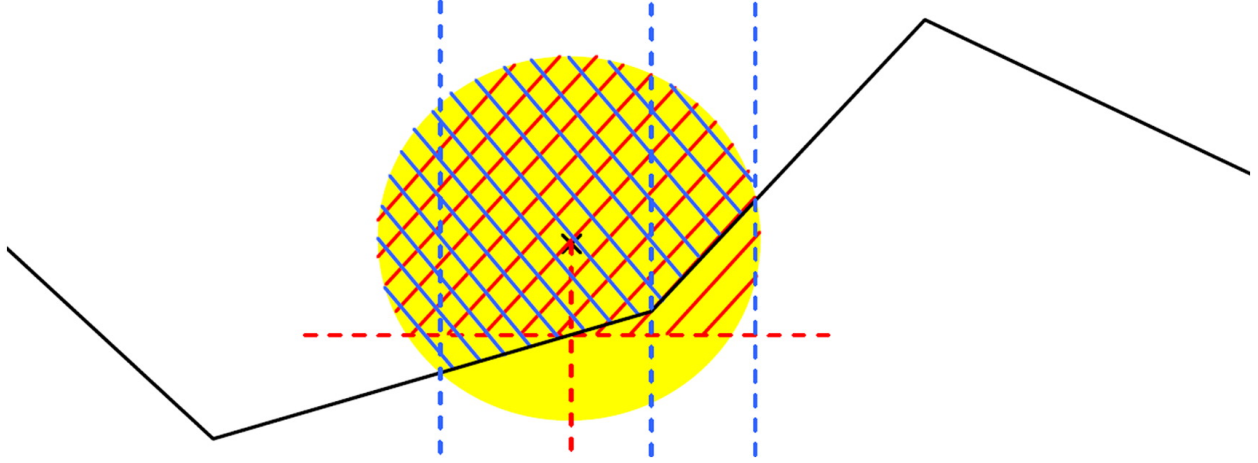
Figure 2.8: Reproduced from De Rosa et al. (2012): Determining the visible fraction of the solar disc using the horizon maps. The yellow circle is the Sun and the solid black line is the horizon map. The horizontal dashed red line is the horizon used in the calculation, which is assumed to be flat and horizontal at the elevation of the actual horizon in line with the centre of the Sun. The upward-facing red hatching represents the calculated visible portion of the Sun, while the downward-facing blue hatching represents the "actual" visible portion, calculated using the real horizon.

obscured segment from the total area of the Sun (see Fig. 2.8 for an illustrative diagram). Although this assumption introduces some error into the calculated value of $V_\odot$, since the horizon is very rarely actually flat and horizontal, De Rosa et al. (2012) found that this error is minimal ($\sim 0.4\%$ of the visible fraction over the course of a year, with very rare instances of errors over 1%). Note that if $i_k > 90$, then that terrain element is "self-shadowed" and has $V_\odot$ set to 0 regardless of whether or not the Sun is above the horizon.

Finally, we need the albedo A_k at each facet. Although the albedo is typically assumed to be a constant value (approximately 0.12 for the lunar highlands), we instead use an incident angle-dependent albedo initially derived by Keihm (1984) using lunar samples returned by the Apollo missions and refined by Vasavada et al. (2012) using Diviner temperature measurements:

$$A(\theta) = 0.12 + 0.045(\theta/45)^3 + 0.14(\theta/90)^8 \tag{2.1}$$

This formulation will be applied both to the directly-illuminated and PSR terrain. It will generally have the effect of increasing the amount of scattered sunlight while decreasing the
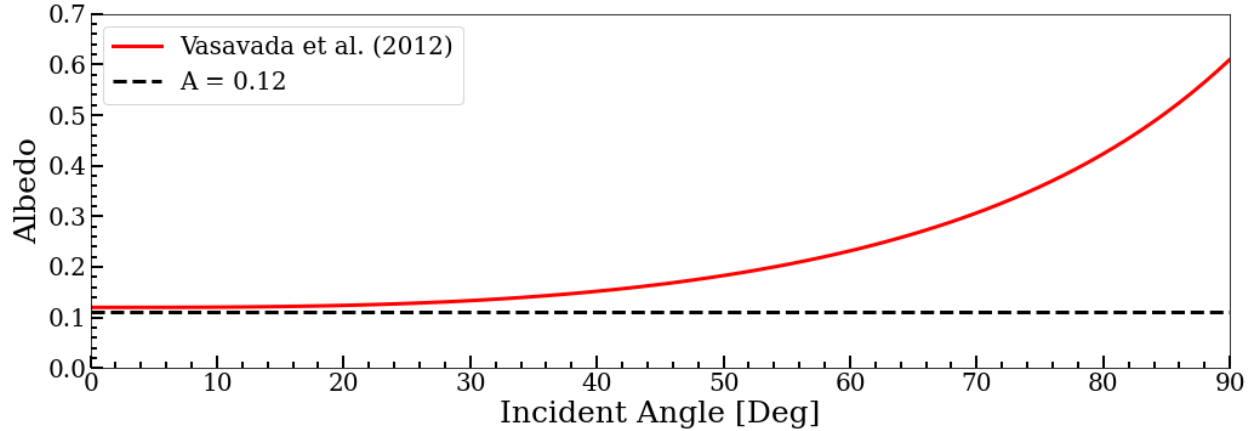
Figure 2.9: Variability of the lunar surface albedo with incident angles as described by Vasavada et al. (2012). A constant albedo of 0.12 is provided for reference.

IR emission, since the terrain geometry leads to a preference for high incidence angles (Kloos et al., 2021), where the albedo differs most greatly from the constant value (see Fig. 2.9).

PSR Terrain

Once we have the upscaled rough terrain maps, we need to assess how the light-scattering terrain visibility has been impacted. We begin by creating a nominal visibility map; that is, determining which portions of the light-scattering terrain are visible at the original 240 m pix^{-1} resolution. This is done by casting a ray between the two terrain facets and determining if any intervening pixels intersect this ray.

While we could use this raytracing method with the upscaled terrain as well, it was ultimately determined that doing so was too computationally expensive given the number of points under examination. Instead, we employ the horizons method once again, albeit in a somewhat unconventional manner. For comparison, at an upscaled resolution of 1 m pix^{-1}, using the horizons method requires casting approximately 20.7 million rays (360 rays for each of the 57,600 subpixel terrain elements). Using the direct raytracing method would require 57,600N rays, where N is the number of light-scattering terrain facets. Shackleton Crater, which contains the smallest number of pixels in its light-scattering terrain map (2041) would thus require almost 117.7 million rays. Because the horizons method is only dependent on
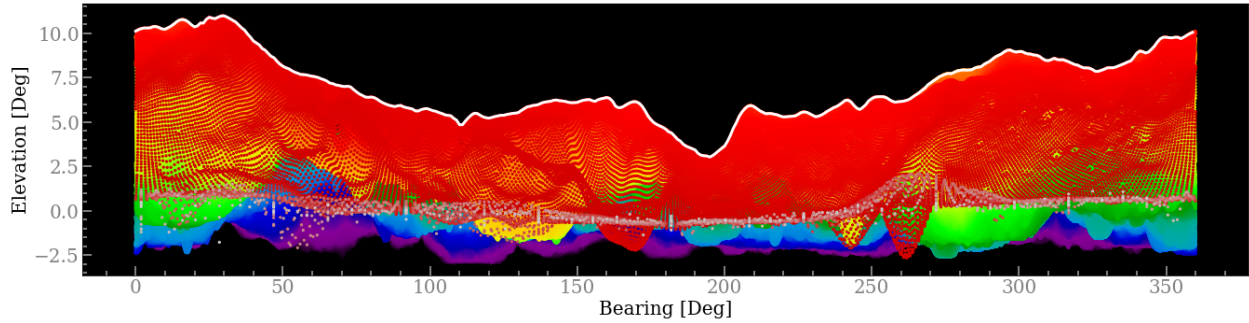
Figure 2.10: Calculated bearings and elevation angles for a point near the centre of Haworth Crater. Colours represent distance. Note that this figure includes all points within the visibility search area (the circle in Fig. 2.6) and thus includes terrain that would not actually be visible. The white line represents the horizon calculated for this point, which is in excellent agreement with the observed horizon.

the number of subpixel points used, it is thus always more far more efficient at this resolution.

For each subpixel point, we find the "local horizon" using the upscaled DEM. This does not represent an "actual" horizon (i.e. one that blocks the Sun); instead, it quantifies the effect of nearby terrain on the visibility of terrain located further away. Rather than determining the location of the Sun as we did when illuminating the light-scattering terrain, we instead are interested in the location of the light-scattering terrain facets themselves, in terms of an elevation angle and azimuth as viewed from the PSR point under investigation. Because we know the coordinates (latitude, longitude, and elevation) of both points, these values can be found through simple vector geometry. For simplicity, we assume that the distances involved are sufficiently large and the elevation changes over the upscaled terrain are sufficiently small that relocating the observer to different subpixel points on the PSR terrain pixel does not significantly impact the calculated locations of the light-scattering terrain. Once these values have been found, we compare them to the elevation of the local horizon at the same azimuth as we did with the Sun. Light-scattering terrain points below the local horizon are no longer capable of scattering light to that particular subpixel point; the line of sight that existed at 240 m/pix has been blocked by small-scale topographic features.

2.1.3 Thermal Modeling

On the surface of an airless body like the Moon, the energy balance equation is as follows:

$$(1 - A)(Q_{\text{direct}} + Q_{\text{scattered}}) + k\frac{\partial T}{\partial z} + \epsilon Q_{\text{IR}} = \epsilon\sigma T^4 \tag{2.2}$$

This equation depends on the albedo and emissivity of the surface (A and ϵ, respectively), the thermal conductivity of the material comprising the surface (k), and the incident radiation in the form of direct (Q_{direct}) and scattered ($Q_{\text{scattered}}$) light as well as thermal emissions from nearby terrain (Q_{IR}).

In our two illumination regimes, we can make different assumptions that will simplify our calculations. Within a PSR, $Q_{\text{direct}} = 0$, by definition. For the light-scattering terrain, we assume that $Q_{\text{direct}} \gg Q_{\text{scattered}}$ and $Q_{\text{direct}} \gg Q_{\text{IR}}$. This allows us to ignore the singly-scattered light and IR emissions incident upon the light-scattering terrain. To take these into account, we would need to calculate the viewfactors for all terrain points visible from each of the light-scattering terrain facets, which would significantly increase the computational load. It should be noted that this assumption holds during the day, when direct sunlight dominates other illumination sources. However, when the Sun sets, there will be zero illumination incident upon the light-scattering terrain, which will necessarily lead to the model underestimating nighttime temperatures.

To convert our modeled fluxes into temperatures, we use a semi-implicit thermal model that implements the Crank-Nicolson solution to the 1D heat equation (Crank and Nicolson, 1996):

$$\rho c\frac{\partial T}{\partial t} = \frac{\partial}{\partial z}\left(k\frac{\partial T}{\partial z}\right) \tag{2.3}$$

The model was developed by Schorghofer (2021) and has been successfully applied to airless bodies like the Moon and Ceres, as well as those with atmospheres. It does have some difficulties at low temperatures, which is problematic considering that that is the regime we are interested in. More accurate low temperature models do exist (e.g. Martinez and Siegler,
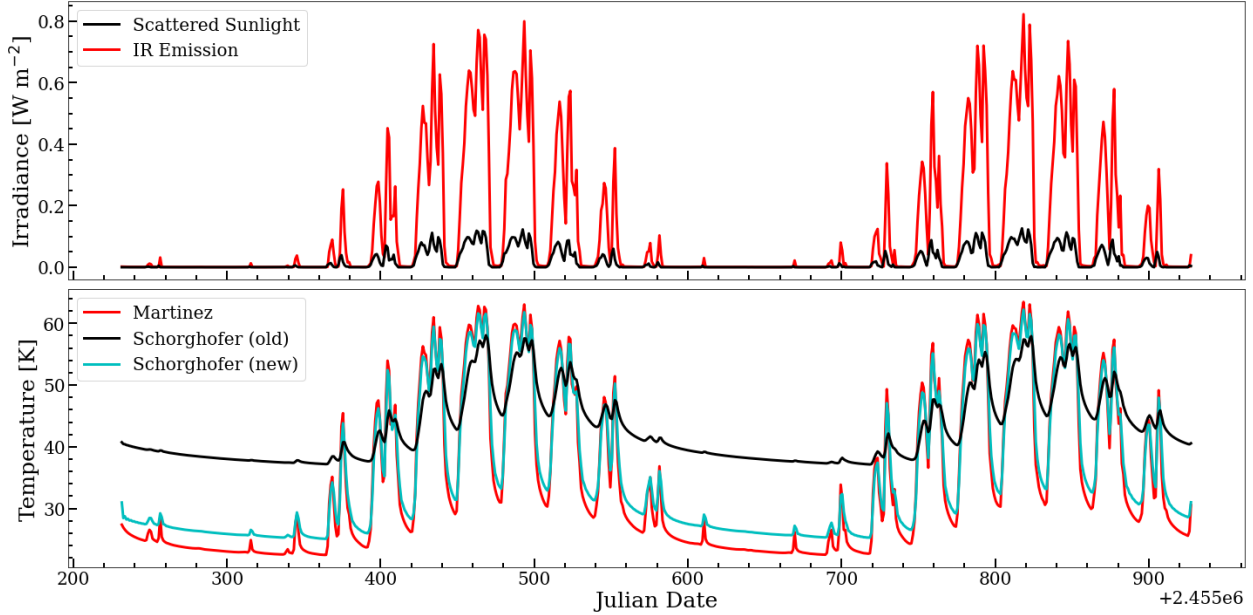
Figure 2.11: Top: Scattered sunlight and IR emission as modeled by Martinez and Siegler (2021) for a pixel located in the Shoemaker PSR. Bottom: A comparison of the three different thermal models when the Martinez and Siegler (2021) irradiances are used as an input. The inadequacy of the Schorghofer (2021) model in this temperature regime is evident; however, when the thermophysical properties are appropriately adjusted, it is capable of replicating the Martinez and Siegler (2021) results almost exactly.

2021), but they come with a significant hit to computational speed, which is not ideal given the large number of points that the model will be applied to.

Because Martinez and Siegler (2021) provide the data that they used to validate their model, we have been able to explore modifications to the model of Schorghofer (2021) that would allow us to exploit its speed while improving its accuracy at low temperatures. We have found that including the temperature- and depth-dependence of the model's physical parameters (density, heat capacity, and thermal conductivity) improved the agreement between the two models without significantly impacting performance.

The specific modifications that we adopted from Martinez and Siegler (2021) are as follows, with the values of various constants given in Table 2.1. The density profile is set to be:

$$\rho(z) = \rho_d - (\rho_d - \rho_s)e^{-z/H} \qquad (2.4)$$

42

ρ_s and ρ_d are the densities at the surface and at depth, respectively, and H is the density scale factor. The effective thermal conductivity of the regolith is defined as:

$$k_{eff}(T, \rho) = (A_1\rho - A_2)k_{am}(T) + (B_1\rho - B_2)T^3 \qquad (2.5)$$

The term "effective thermal conductivity" is used because the thermal conductivity is the sum of a solid conduction term (the A constants) and a radiative conduction term (the B constants). The radiative conduction term depends on the cube of the temperature, while the temperature dependence of the solid conduction term $(k_{am}(T))$ is more complex:

$$k_{am}(T) = A_c + B_cT^{-4} + C_cT^{-3} + D_cT^{-2} + E_cT^{-1} + F_cT + G_cT^2 + H_cT^3 + I_cT^4 \qquad (2.6)$$

Finally, the heat capacity of the regolith is:

$$c_p(T) = c_0 + c_1T + c_2T^2 + c_3T^3 + c_4T^4 \qquad (2.7)$$

The model is run on a set of points representing the lunar subsurface at several depths. The density of points decreases with increasing depth (i.e. most of the points are located near the surface), as the near-surface layers are most sensitive to changes in the incident flux on the surface. The spacing is defined as such (Hayne et al., 2017):

$$\Delta z_0 = z_s/m \qquad (2.8)$$

$$\Delta z_i = \Delta z_{i-1}\left(1 + \frac{1}{n}\right) \qquad (2.9)$$

where Δz_0 and Δz_i are the spacing between the surface and first subsurface points and the spacing between subsequent subsurface points, respectively. m and n are numerical factors

Symbol	Description	Value	Units
A_0	Normal albedo	0.12	Dimensionless
dt	Timestep	10800	s
F_{geo}	Geothermal heat flux	0.018	W m^{-2}
H	Density scale factor	0.056	m
k_d	Deep layer conductivity	3.8×10^{-3}	W m^{-1}K^{-1}
k_s	Surface layer conductivity	8.0×10^{-4}	W m^{-1}K^{-1}
m	Grid parameter	20	Dimensionless
n	Grid parameter	5	Dimensionless
P	Diurnal period	2.55024×10^6	s
S	Solar constant	1361	W m^{-2}
z_{max}	Maximum grid depth	2.5	m
ϵ	Infrared emissivity	0.95	Dimensionless
ρ	Regolith density	$\rho_d - (\rho_d - \rho_s)e^{-z/H}$	Kg m^{-3}
ρ_d	Deep layer bulk density	1800	Kg m^{-3}
ρ_s	Surface layer bulk density	1100	Kg m^{-3}
A_1	Solid conduction constant	5.0821×10^{-6}	_^{1}
A_2	Solid conduction constant	5.1×10^{-3}	_^{1}
B_1	Radiative conduction constant	2.0022×10^{-13}	_^{1}
B_2	Radiative conduction constant	1.953×10^{-10}	_^{1}
A_c	Solid conduction coefficient	-0.203297	_^{1}
B_c	Solid conduction coefficient	-11.472	_^{1}
C_c	Solid conduction coefficient	22.5793	_^{1}
D_c	Solid conduction coefficient	-14.3084	_^{1}
E_c	Solid conduction coefficient	3.41742	_^{1}
F_c	Solid conduction coefficient	0.01101	_^{1}
G_c	Solid conduction coefficient	-2.8049×10^{-5}	_^{1}
H_c	Solid conduction coefficient	3.35837×10^{-8}	_^{1}
I_c	Solid conduction coefficient	-1.40021×10^{-11}	_^{1}

Table 2.1: A summary of the thermophysical parameters used in the thermal model. k_d, k_d, and H are from Martinez and Siegler (2021), ρ_d and ρ_s are from Hayne et al. (2017), and F_{geo} is from Langseth et al. (1976). [1]The units of the solid and radiative conduction constants and the solid conduction coefficients are chosen such that k_{eff} has units of W m^{-1}K^{-1}.

controlling the vertical distance between grid points, and z_s is the skin depth:

$$z_s = \sqrt{\frac{\kappa P}{\pi}} \tag{2.10}$$

The skin depth describes how far into the subsurface the diurnal heat wave penetrates. It depends on the diurnal period P and the thermal diffusivity κ, which itself depends on the thermal conductivity K, density ρ, and heat capacity c_p:

$$\kappa = \frac{K}{\rho c_p} \tag{2.11}$$

We calculate the skin depth using a simplified temperature-independent form of the thermal conductivity:

$$k_c(z) = k_{c,d} - (k_{c,d} - k_{c,s}) \left(\frac{\rho_d - \rho(z)}{\rho_d - \rho_s} \right) \tag{2.12}$$

To ensure convergence, we initialize the temperatures as such:

$$T_s = \sqrt[4]{\frac{Q_{total}}{\epsilon \sigma}} \tag{2.13}$$

$$T_d = \frac{T_s}{\sqrt{2}} \tag{2.14}$$

$$T(z) = T_d - (T_d - T_s)e^{-z/H} \tag{2.15}$$

where T_s and T_d are the temperatures at the surface and the deepest layer, respectively. The model is run over one draconic year, at which point the illumination conditions at the end are (approximately) the same as at the beginning, so the model is run again using the output temperatures as the input. This process is repeated five times. Ideally, we would want to simulate the entire lunar precessional cycle of 18.6 years to ensure that the illumination at the beginning and end are exactly the same, but the difference is relatively small and we see rapid convergence regardless.

For expediency, we only apply the thermal model to the PSR terrain. We do not use it

to find the temperature of the light-scattering terrain, which is needed as an input to Q_{IR}. Instead, we assume that the temperature of the light-scattering terrain facets is equal to their equilibrium temperature, given by:

$$T_{eq} = \sqrt[4]{\frac{(1-A)Q_{direct}}{\epsilon\sigma}} \tag{2.16}$$

Note that we are implicitly assuming here that the direct solar insolation is the only source of thermal energy on the light-scattering terrain. Although the light-scattering terrain facets are also subject to scattered sunlight and thermal emissions, direct illumination is by far the dominant energy source during the lunar day. Combined with the facts that the regolith responds quickly to changes in direct insolation and that the Moon's slow rotational period causes the direct insolation to change gradually, the equilibrium temperature provides an impressively close fit to Diviner temperatures during the day, despite being a very simple model (see Fig. 2.12).

During the lunar night, however, the situation is quite different. Because the equilibrium temperature does not account for the regolith gradually releasing its heat and cooling down when in shadow (and because we have assumed that there are no other illumination sources), the temperature immediately drops to 0 K as soon as the Sun is no longer visible. Consequently, our illumination model will underestimate the amount of light incident upon the PSR terrain facets during the night. Fortunately, because we are only interested in the *maximum* temperatures reached in the PSR, which occur during the day, inconsistencies at night should not affect our analysis.

There is one point worth considering in this model. In Fig. 2.12, one can see a collection of points where the model is significantly overestimating the maximum temperature. Notably, nearly all of these points are clustered just below the water stability threshold of 110 K. Because these are PSR-like temperatures on non-PSR terrain, we can hypothesize that these points are just barely exposed to the Sun. They are illuminated by the Sun for
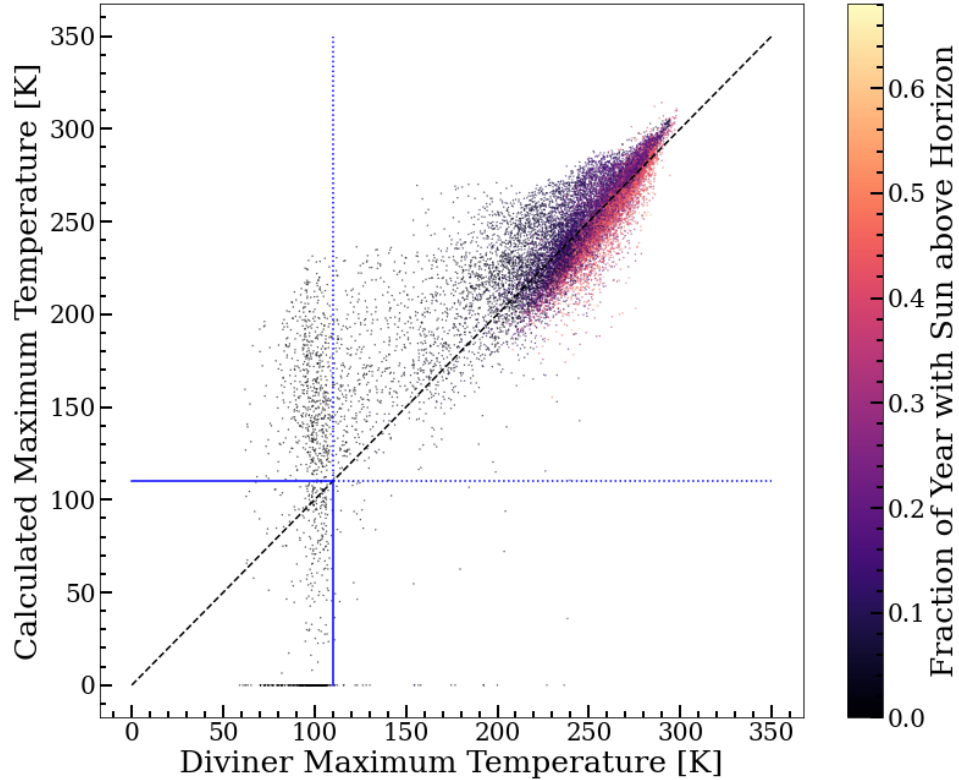
Figure 2.12: A comparison of our equilibrium maximum temperatures with the maximum temperatures measured by Diviner, coloured by the fraction of each year that each point experiences direct solar illumination. Ideally, all points would lie along the 1:1 correspondence line, and most are quite close, with the notably exception of a group of points just below the water stability threshold (the blue lines).

just long enough to not be considered permanently-shadowed, but not long enough for the temperatures to reach the equilibrium values generated by the model.

If we exclude points that are illuminated for less than 5% of the year, we can quantify how well the model replicates Diviner observations in the regime where its assumptions are valid. In Fig. 2.14, we plot linear fits to the data when we include all points and only those with $> 5\%$ illumination. In the former case, the fit is nowhere near the 1:1 correspondence line. However, in the latter case our fit has a slope of 0.97 and a y-intercept of 2.03, very close to the expected 1:1 values of 1 and 0. Although the spread around the fit does increase substantially towards lower temperatures (as expected), it remains < 50 for nearly all points. Taken together, these two measures indicate that the model produces results that are closely-
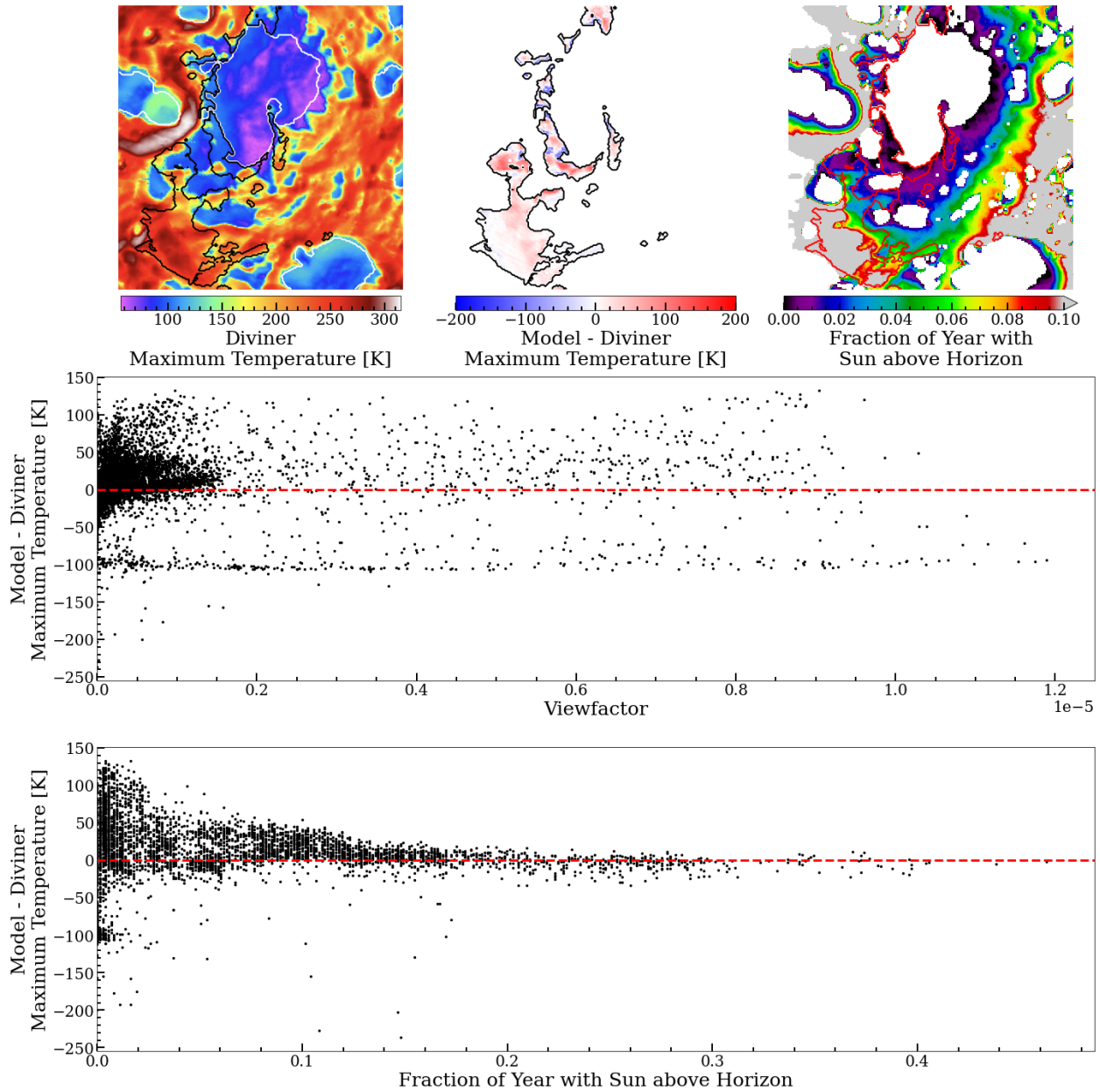
Figure 2.13: Top left: Maximum temperatures from Diviner. PSRs are outlined in white and the light-scattering terrain is outlined in black, showing how much of the light-scattering terrain has PSR-like temperatures. Top middle: The difference between the modeled and Diviner maximum temperatures for the light-scattering terrain, with the extent of the light-scattering terrain outlined in black. Top right: The faction of the year that each terrain facet spends illuminated, the light-scattering terrain outlined in red. The colorscale is chosen to highlight those points that are illuminated for < 10% of the year. Middle: The temperature difference as a function of the viewfactor, showing that many of the overmodeled points contribute significantly to the total IR illumination of the LCROSS impact site. Bottom: The temperature difference as a function of fractional illumination, showing how the difference increases rapidly for points that experience minimal illumination.
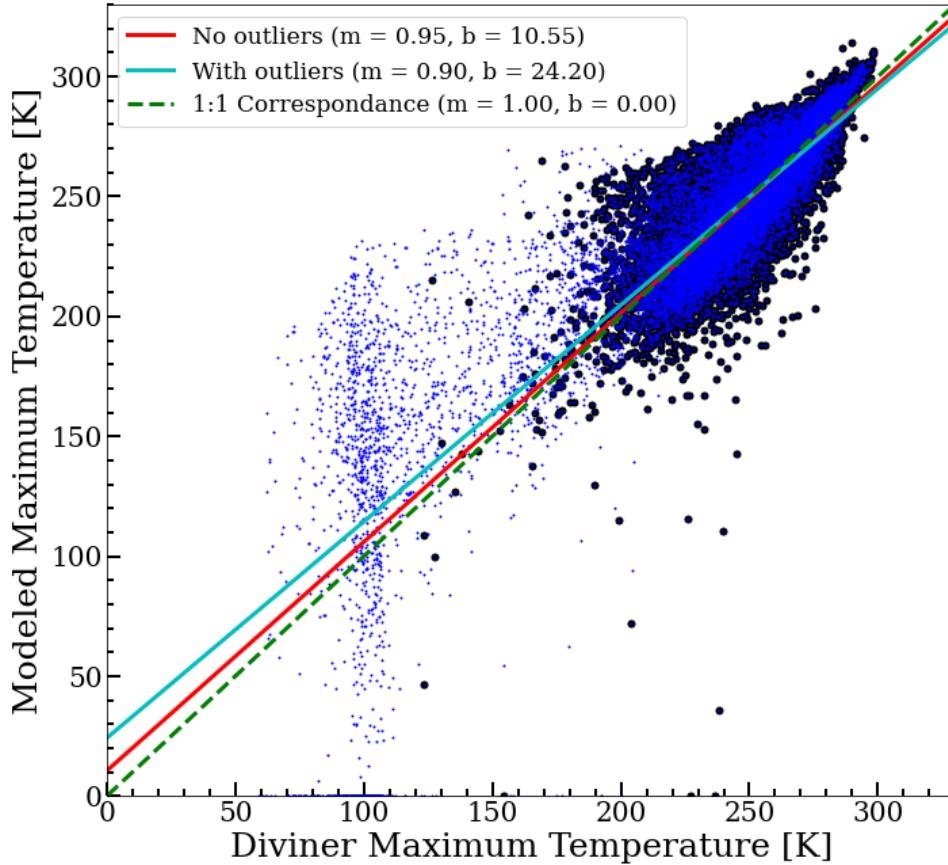
Figure 2.14: Linear fits to our modeled maximum temperatures of the light-scattering terrain as a function of Diviner maximum temperature. When we fit only those points that are illuminated for $> 5\%$ of the year (black points), the fit (red solid line) closely follows the 1:1 correspondance line (green dashed line). When we fit all points (blue points), the fit (cyan line) is slightly worse, though the spread is visually much larger.

aligned with expectations in the appropriate illumination regime.

Should we be worried about the overmodeled temperatures? If we look at the middle panel of Fig. 2.13, we can see that there is a significant overlap between the set of terrain facets with large viewfactors and the set of terrain facets with excessively high temperatures. Because the viewfactor is a measure of how influential a particular terrain facet is to the sum of scattered light, this suggests that we could be significantly overestimating how much IR radiation is being directed towards the LCROSS impact site. To quantify the magnitude of this effect, we can re-run our illumination model as before, but capping the maximum temperature of these seasonally-shadowed regions at 110 K. In Fig. 2.15, we can see that

the difference in IR emission caused by this correction is negligible.
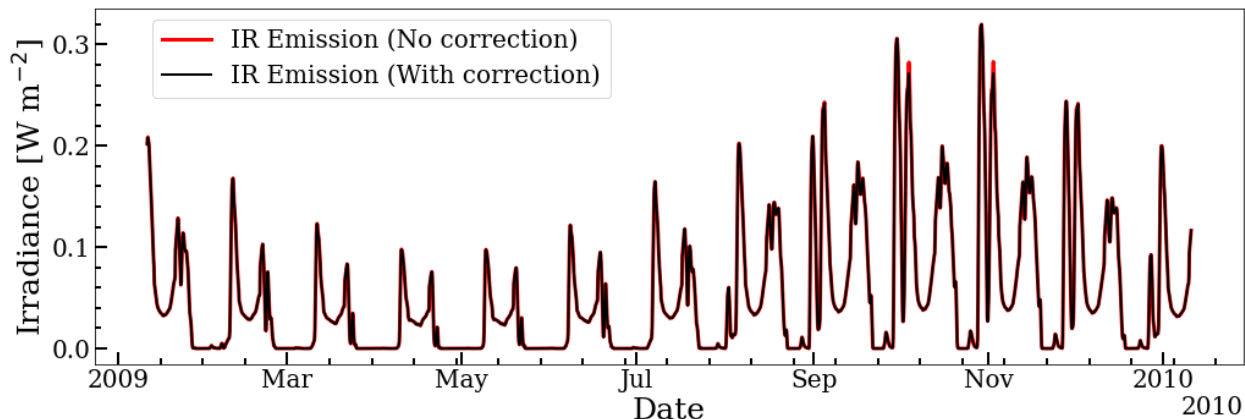
Figure 2.15: A comparison of the IR emissions incident upon the LCROSS impact site at 240 metres per pixel before and after applying a simplified correction accounting for the colder than expected temperatures of seasonally-shadowed regions surrounding the Cabeus PSR.

We can also see in Fig. 2.12 that there is a small number of points for which the instantaneous thermal equilibrium assumption is actually *undermodeling* the temperatures. Running through the same examination as we did for the overmodeled points, these points appear to be located mostly at the edge of the Cabeus PSR. The illumination conditions in this area are very PSR-like, being dominated by IR emission and scattered sunlight for the vast majority ($> 99\%$) of the year. Because our model ignores these light sources for non-PSR terrain points (even those that are nearly permanently-shadowed), it will output a temperate of 0 K at all times other than those brief moments of direct illumination. We know that PSRs are not that cold, so it makes sense that the terrain in this transition zone would not be either. If we once again correct our IR emission values, this time setting both the overmodeled and undermodeled terrain points to 110 K, we can see in Fig. 2.16 that the difference is larger than that created by correcting for just the overmodeled temperatures.
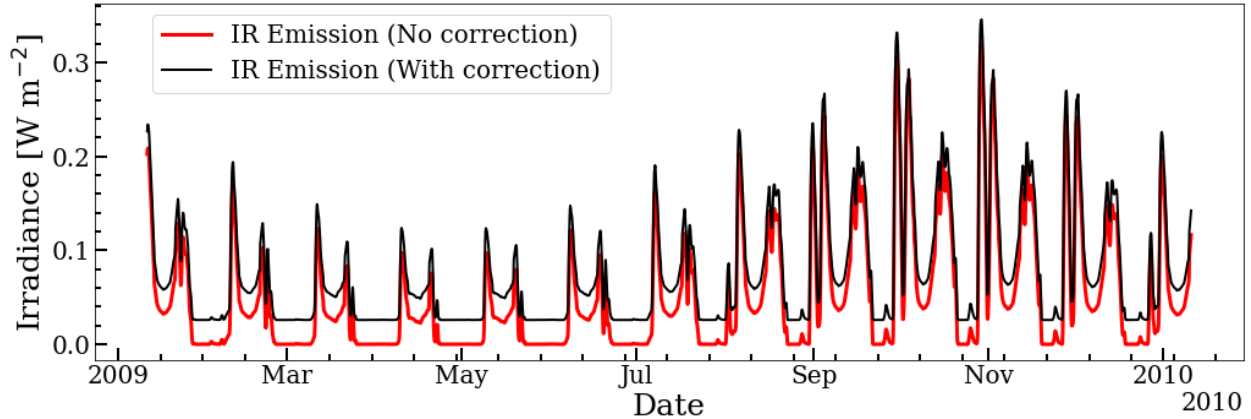
Figure 2.16: A comparison of the IR emissions incident upon the LCROSS impact site at 240 metres per pixel before and after applying a simplified correction accounting for both the colder and warmer than expected temperatures of seasonally-shadowed regions surrounding the Cabeus PSR.

2.2 Results and Analysis

We begin our model on January 11, 2009 and run it through one draconic year (346.6 Earth days) with three hour timesteps. We chose this point in time because it encompasses the LCROSS impact event, which occurred on October 9, 2009. Because lunar nodal precession causes illumination conditions to vary slightly from year to year over a single precessional cycle of 18.6 years, we can be assured that our results are representative of the conditions present at the time of impact.

2.2.1 Model Validation

In this section, we will provide validation of our thermal and illumination models by comparing our derived results to real-world observed conditions. Our comparison dataset will be Diviner polar temperature maps created by binning the first ~ 10 years of Diviner measurements first into 240 metre pixels and then again into 96 timesteps each spanning $3.75°$ of subsolar longitude.

As seen in Fig. 2.17, our model follows the Diviner measurements reasonably closely, replicating the approximate range of temperatures as well as the double-peaked shape with
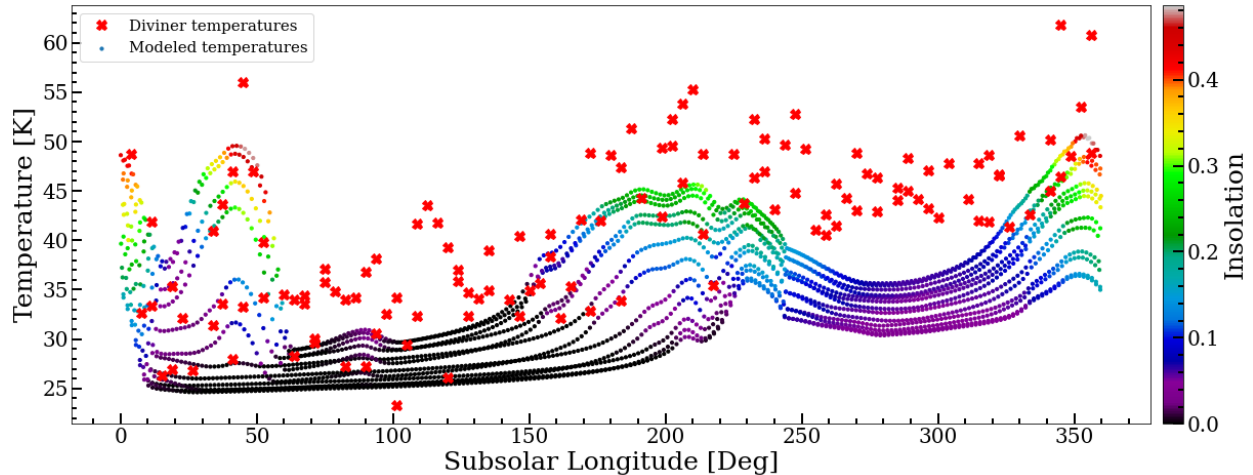
Figure 2.17: A comparison of our model's output temperatures at 240 m/pix with binned temperature measurements of the LCROSS impact site from Diviner. Although there are small inconsistencies between the model and measurements at extreme illumination conditions, the two generally follow each other reasonably closely.

local maximums between 0–50° and 200–250°. The largest disagreement between the model and Diviner measurements occurs after 200°, when the model underestimates temperatures by approximately 10 K.

There are several potential reasons for the small differences between our modeled temperatures and those measured by Diviner. First, as was previously noted, our illumination model does not include all illumination sources, focusing solely on singly-scattered sunlight and thermal emission. When combined with the fact that we used instantaneous equilibrium temperatures for the directly-illuminated terrain, this could account for the underestimated temperatures while the system is in shadow. With no direct illumination on any surfaces, our model assumes that the total flux upon the PSR terrain facet is exactly zero; in reality, we would expect to see non-zero values due primarily to the fact that all surfaces in view would still be putting out IR emission. Some of the difference could also be explained by the fact that the model assumes that the PSR terrain facet is perfectly smooth and at a single temperature. We know for a fact that this is not the case; the measurements made by Diviner are a weighted average of many temperatures.

Regardless of these differences, we can say with confidence that our illumination model,

despite making a number of simplifying assumptions, does a reasonably good job of replicating the Diviner temperatures when used as an input to the thermal model.

2.2.2 Small-Scale Temperatures

The maximum temperature map of the LCROSS pixel at a subpixel resolution of 1 m/pix as output by our model is presented in Fig. 2.18. When comparing with the stability temperatures of the LCROSS volatiles given in Table 2.2, several points are immediately obvious. First, the maximum temperature reached is 46 K. This is sufficiently low for the cold-trapping of nearly all of the volatiles detected in the LCROSS impact plume. Second, the temperature distribution is highly heterogeneous, with the vast majority of the coldest pixels concentrated at the centre-right edge of the pixel. The heterogeneity is a consequence of our choice to use LOLA elevation maps rather than an idealized terrain model. We can see proof of that in Fig. 2.19. For the point that experiences the highest modeled maximum temperature, most of the high-viewfactor light-scattering terrain facets lie above the upscaled local horizon. Conversely, the high-viewfactor facets lie almost entirely below the local horizon of the point with the lowest modeled maximum temperature.
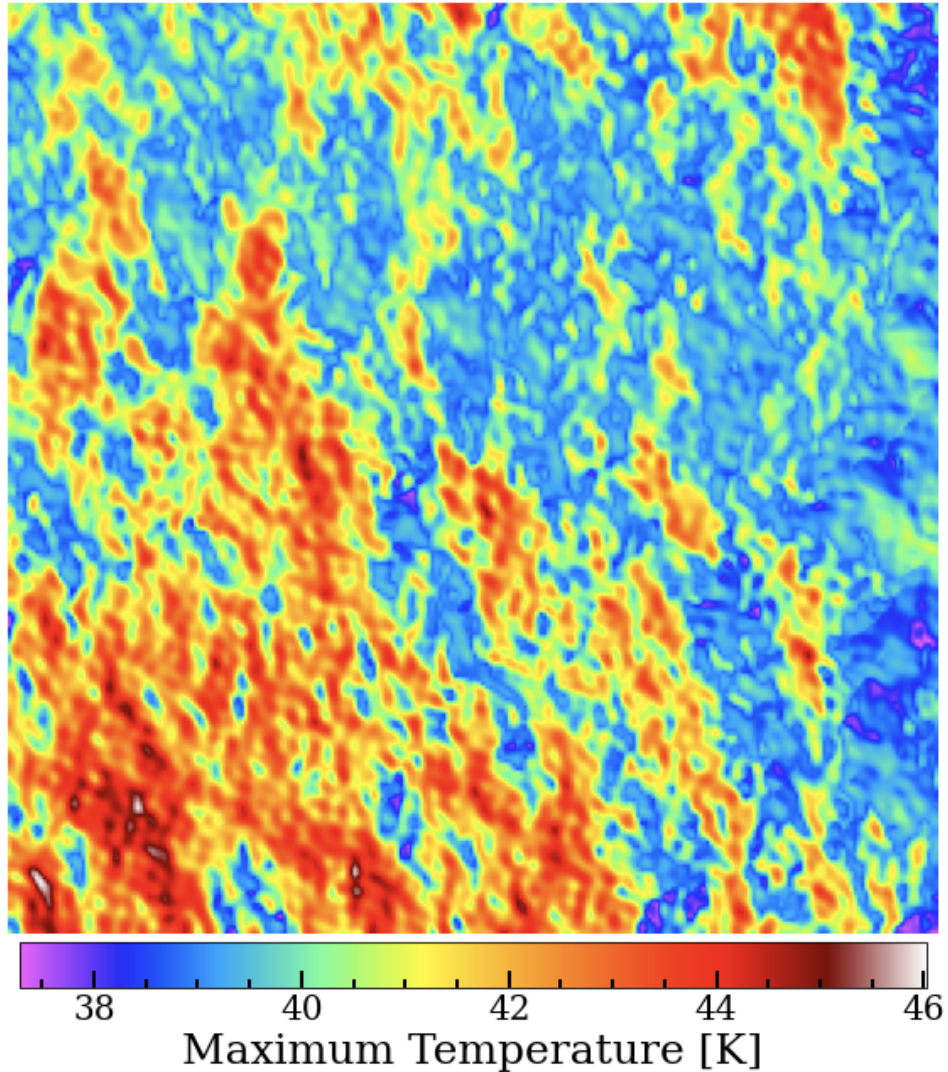
Figure 2.18: The output maximum temperature map output by our model at the upscaled resolution of 1 m/pix. The temperature ranges from a minimum of 37 K to a maximum of 46 K. The heterogeneity of the temperature distribution is evident.

If the abundances of the various volatiles detected in the LCROSS impact plume, one would expect that the abundances would follow the available cold-trapping area. This is clearly not the case, as C_2H_4 and CH_4 are the only detected species that are not stable across the entire upscaled pixel. The fact that the other species are detected at concentrations of a few percent relative to water suggests that the area available for cold-trapping is not the dominant factor in determining volatile abundances at the LCROSS impact site.
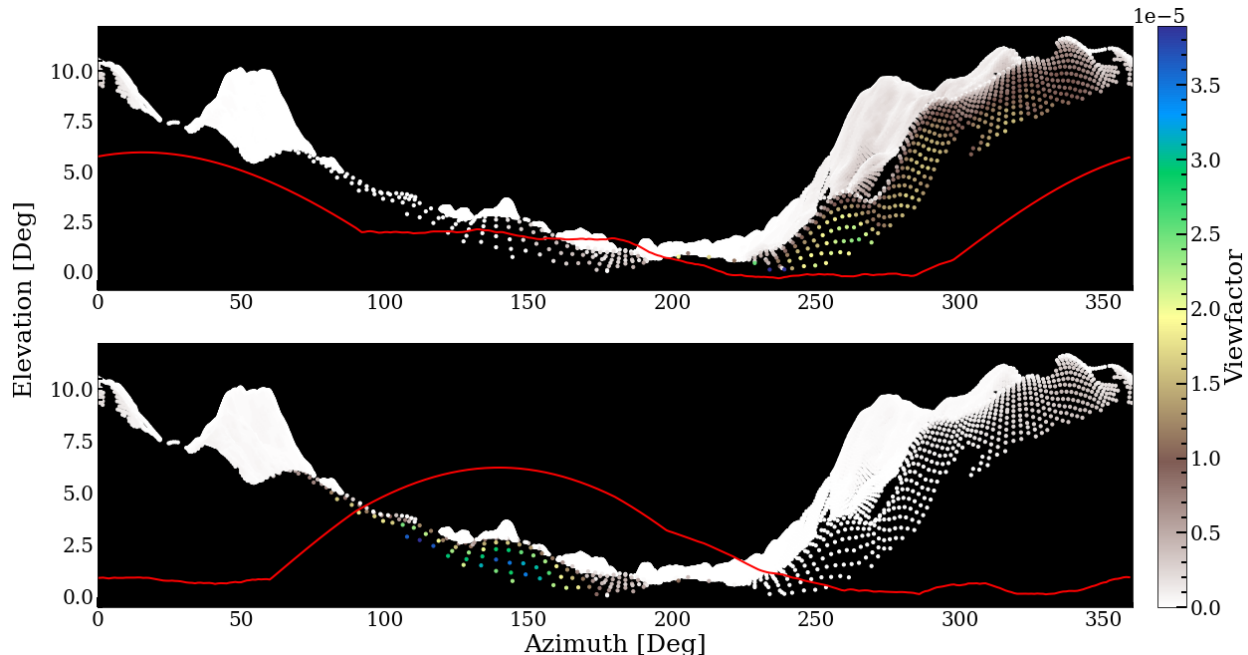
Figure 2.19: Similar to Fig. 2.5: Light-scattering terrain viewfactors for the subpixel points with the highest (top) and lowest (bottom) modeled maximum temperatures. We can clearly see how the temperatures at these points are caused by the positioning of the high-viewfactor points either above or below the local horizon. The different viewfactor values at each facet between the two points is caused by the specific combination of slope and aspect angles at each location in the upscaled terrain.

We should also consider the fact that our model only considers the surficial thermal environment, and thus any conclusions we draw are only relevant at the surface. This is potentially problematic because it is known that LCROSS did not exclusively sample volatiles present at the surface. It is estimated that the impact exhumed an area down to a depth of no more than 10 metres (Hermalyn et al., 2012). Although we did not produce a full sub-surface temperature profile for each of the points in our upscaled terrain for the sake of computational efficiency, we could look at the sub-surface temperature profile at 240 m/pix to examine how depth affects volatile stability.

Unfortunately, temperature is not as direct of a proxy for volatile stability in the sub-surface as it is on the surface. At the surface, we can assume that any volatile molecules residing on a terrain element that is hotter than the volatile's stability temperature is immediately lost because it is free to travel on a ballistic trajectory. When the molecule is buried

Compound	% Relative to H_2O (g)	Stability Temperature (K)	Pixel Stability Fraction
H_2O	100.0	106.6	100.0
H_2S	16.75	50.6	100.0
NH_3	6.03	65.5	100.0
SO_2	3.19	62.3	100.0
C_2H_4	3.12	43.1	92.5
CO_2	2.17	54.3	100.0
CH_3OH	1.55	91.8	100.0
CH_4	0.65	22	0.0
OH	0.03	–	–

Table 2.2: Abundances of various compounds detected in the LCROSS impact plume (Colaprete et al., 2010). We do not calculate a stability temperature for OH because much of the detected hydroxyl likely came from photolysis of water in the impact plume into hydroxyl radicals and free hydrogen atoms. (Some spacecraft observations have found OH adsorbed on the regolith, but the relative abundance here is so small as to be insignificant in our analysis.)

under the regolith, it cannot escape even if it is above the temperature that would cause it to sublimate. Instead, thermally unstable subsurface volatiles undergo vertical migration within the regolith (Schorghofer and Taylor, 2007). This "ice pump" effect driven by the day-night temperature cycle that drives surficial ice deposits into the subsurface has been proposed as a mechanism to explain the lack of a clear correlation between PSRs and areas where neutron spectroscopy reveals H-enhancement (Schorghofer and Aharonson, 2014).

2.3   Discussion

Are our modeled upscaled temperatures consistent with Diviner measurements? To answer this question, we have to understand how the Diviner temperatures are derived. Up until this point, we have been saying that Diviner "averages over" temperatures at smaller scales. Much like the Diviner measurements themselves, this simple phrase ignores the finer details of what's going on. Diviner measures integrated radiances from the lunar surface in nine spectral channels – two to measure reflected sunlight, and seven to measure infrared emission. Channels 6 through 9, covering a wavelength range of $13 - 400$ μm are most sensitive to

surface temperatures (Paige et al., 2010a). If we assume that the surface radiates like a blackbody, then the observed spectrum should follow a Planck function. By comparing the measured radiances to those of an idealized blackbody in the Diviner channels, it is possible to determine a "brightness temperature".

When Diviner observes an area where multiple temperatures are present, there is no way to determine which photons originate from where; a 550 nm photon from a 250 K surface is exactly the same as a 550 nm photon from a 40 K surface. As a result, the observed spectrum is a sum of many Planck functions, each created by a blackbody radiating at a different temperature. Because the intensity of a blackbody's spectrum at a particular wavelength depends on its temperature, this effectively means that the overall spectrum is a weighted average of all the subpixel temperatures, with higher temperatures contributing more since they output more photons at all wavelengths than lower temperatures (Vasavada et al., 2012).

Because Diviner only measures integrated radiances over specific channels, it matters which channel you are using to derive the temperature. At long wavelengths, the difference in the number of photons emitted by a hot and cold blackbody differ only slightly, so the derived temperature will more closely follow a straight average. At short wavelength, the difference in radiances increases dramatically, resulting in a much heaver weight given to the warmer subpixel temperatures. Thus, the short wavelength channels will record a higher brightness temperature than the long wavelength channels. This effect is shown in Fig. 2.21 using a simulated surface that is 75% at 60 K and 25% at 100 K. The short-wavelength Diviner channels 6 and 7 measure brightness temperatures of 84 K and 78 K, while the long-wavelength channels 8 and 9 measure brightness temperatures of 72 K and 70 K. The range of temperatures measured across the four channels can be used as a proxy for the subpixel temperature variability. A pixel with a small range of surface temperatures will show a small range of brightness temperatures and vice versa.
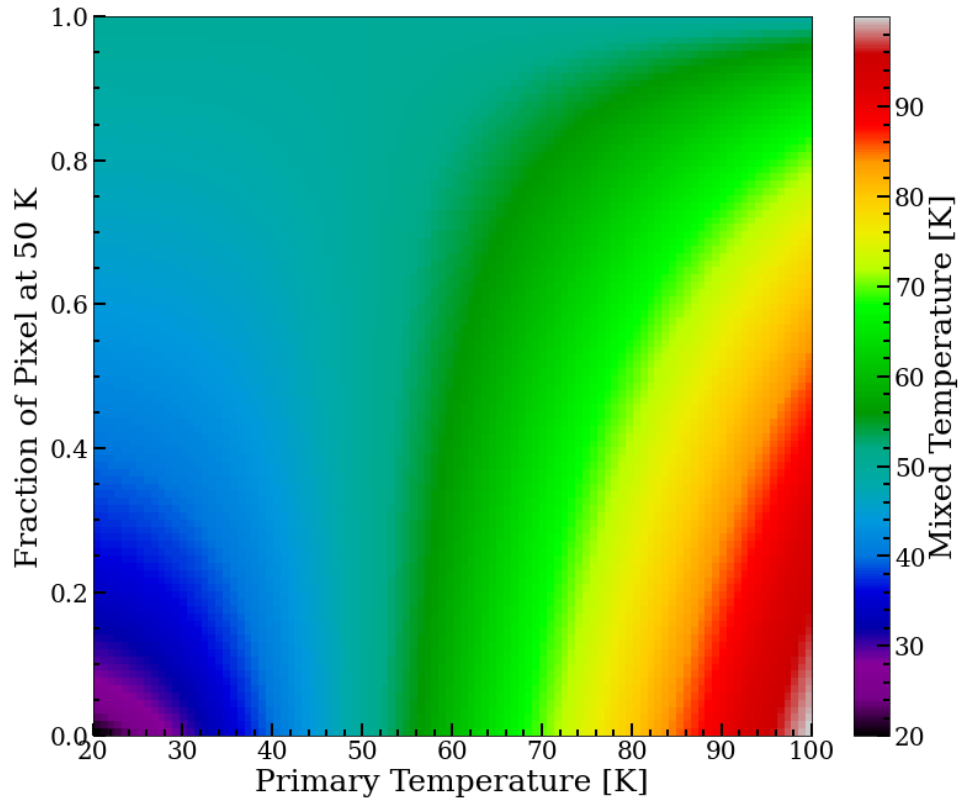
Figure 2.20: Temperature mixing in a two element model where the temperature of one element is allowed to vary between 20 K and 100 K and the other is fixed at 50 K but its coverage is allowed to vary between 0% (the entire pixel is at the primary temperature) and 100% (the entire pixel is at 50 K).
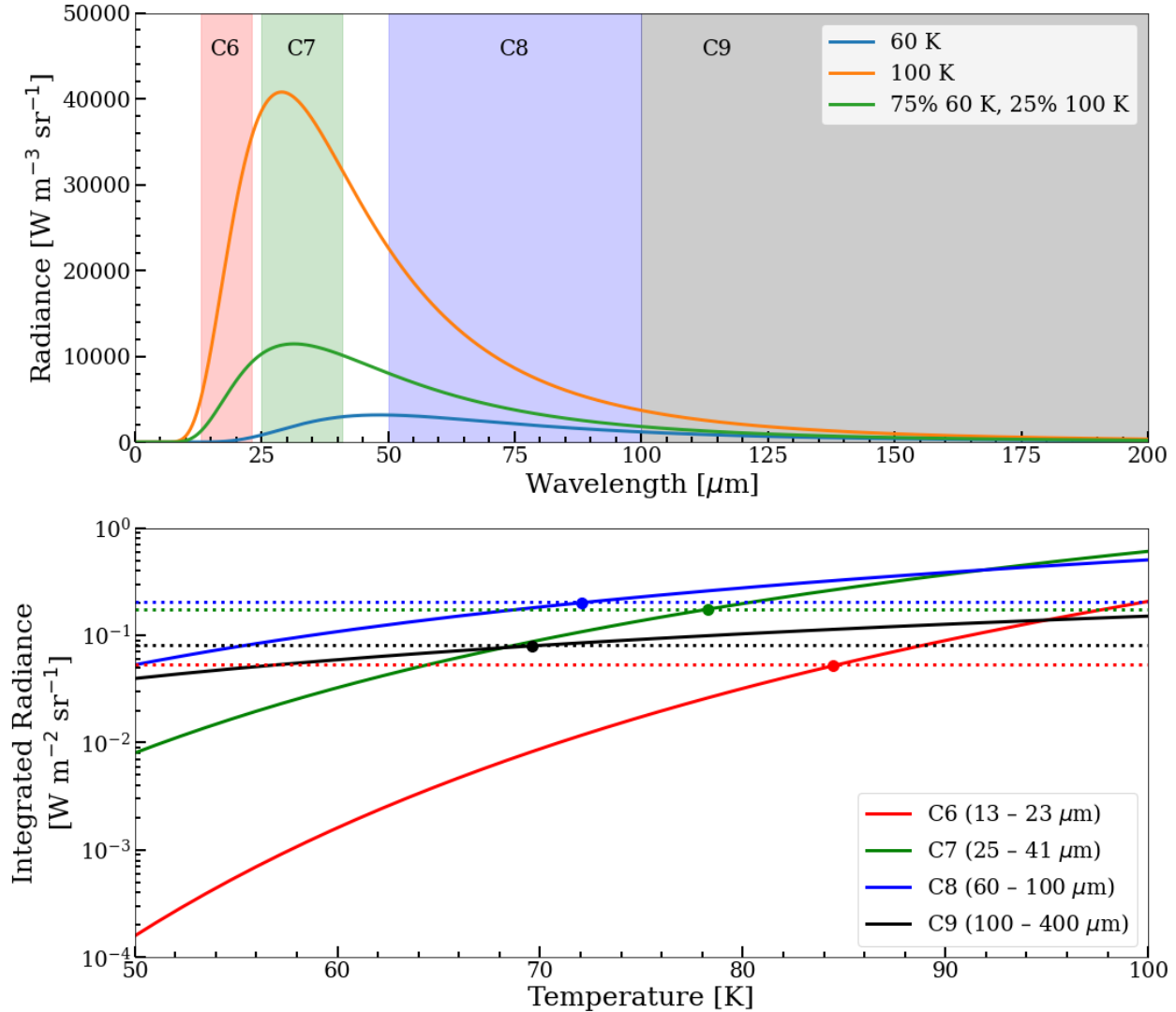
Figure 2.21: Top panel: Planck spectra for three blackbody surfaces - one at 60 K, one at 100 K, and one with 75% of its surface area at 60 K and 25% at 100 K. The ranges of the four Diviner thermal channels are overlaid, showing how the shorter-wavelength channels are more sensitive to temperature than the longer-wavelength channels. Bottom panel: Determining brightness temperatures. The solid curves represent the total integrated radiance in each of the Diviner channels as a function of temperature. The dotted lines are the integrated radiance of the temperature-mixed surface from the top panel. The intersection of each curve represents the measured brightness temperature in that channel. As expected, channels 6 and 7 output higher temperatures than channels 8 and 9.

To account for the different brightness temperatures in each channel, the Diviner temperature maps are produced by calculating a bolometric brightness temperature (Paige et al., 2010b):

$$\sigma T_{bol}^4 = \sum_i \sigma T_i^4 f(T_i, \lambda_1, \lambda_2) \tag{2.17}$$

T_i is the brightness temperature as measured in each channel, λ_1 and λ_2 are the lower and upper wavelength limits of each channel, and $f(T_i, \lambda_1, \lambda_2)$ is defined by integrating the Planck function $B(\lambda, T)$:

$$f(T_i, \lambda_1, \lambda_2) = \frac{\int_{\lambda_1}^{\lambda_2} B(\lambda, T_i) d\lambda}{\int_0^\infty B(\lambda, T_i) d\lambda} \tag{2.18}$$

In Fig. 2.22, we present brightness temperatures that would be measured by Diviner given our modeled subpixel temperatures. As expected, these temperatures are lower than those in Fig. 2.17 due to subpixel temperature mixing. The simulated Diviner measurements now about 15 K lower than the actual measurements, exacerbating the difference that was seen in Fig. 2.17. This could be indicative of several potential problems. First, our illumination model could be wrong. We know that our assumptions result in an underestimation of incident energy upon the PSR terrain while the light-scattering terrain is in shadow, which would likely result in lower than expected temperatures. Second, it could be evidence that our assumptions about the physical parameters of the surface were incorrect. Hayne et al. (2021) found that increasing the RMS slope of the rough surface led to more extreme temperatures. Increasing the peak temperatures experienced by the surface (while simultaneously decreasing the minimum temperatures) could plausibly result in a higher observed brightness temperature.

In the bottom panel of Fig. 2.22, we also present the difference in brightness temperatures between channels 6 and 9. Because these channels are on opposite ends of the wavelength range, the difference between their brightness temperatures represents the largest inter-channel temperature difference. The difference generally increases with increased insolation. As previously mentioned, larger differences are caused by a wider range of subpixel
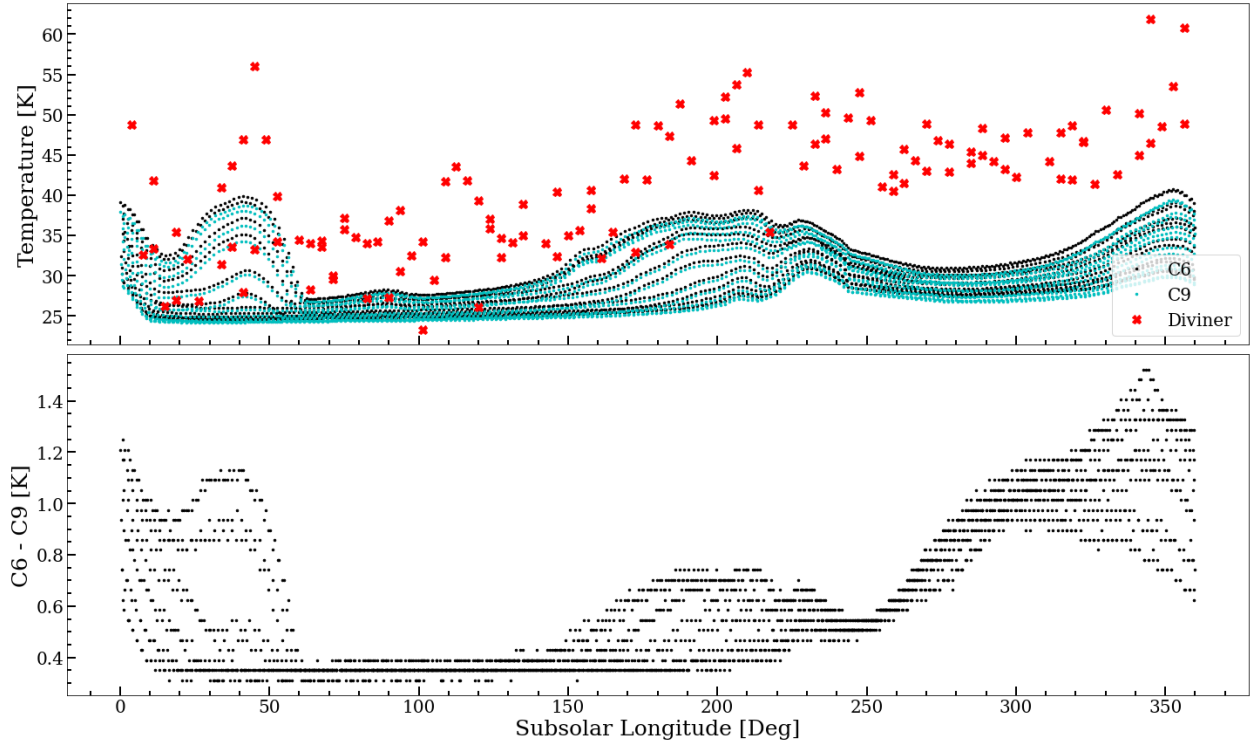
Figure 2.22: Top panel: Calculated Diviner channel 6 and 9 brightness temperatures for our surface. When compared to Fig. 2.17, the peak temperatures in the high insolation regime closely follow the Diviner data, but the low insolation temperatures have dropped below the range of Diviner temperatures. Bottom panel: The difference in brightness temperatures between channels 6 and 9. We choose to plot this value because it represents the greatest difference in brightness temperatures among the four thermal channels. Its value generally increases with increasing insolation, consistent with an increased range of temperatures across the pixel due to doubly-shadowed regions not receiving scattered sunlight. We see that it generally increases with temperature, which is consistent with the idea of sub-pixel topography creating small doubly-shadowed regions.

temperatures. What these data then suggest is that when light is being scattered into the PSR, areas exposed to that scattered light heat up while doubly-shadowed regions remain cold. There does appear to be a large amount of seasonal variability in the magnitude of this difference, particularly in the highest insolation regime from $300 - 50$ °.

This seasonality of temperatures is important to consider because volatile molecules do not immediately sublimate upon being exposed to temperatures above their stability threshold. The stability threshold itself is somewhat arbitrary, being defined as the temperature at which a millimetre-thick deposit would take a gigayear to sublimate away. Consequently,

it is possible that exposed volatiles could survive for an extended period of time on a surface that is periodically exposed to high temperatures, meaning that an analysis based wholly on maximum temperatures is not necessarily representative of a surface's ability to retain volatiles. Of course, any volatile deposit will eventually vanish if the average sublimation rate is greater than the deposition rate, but the timescale over which destruction occurs will be longer on an occasionally hot surface than one that experiences sustained high temperatures. We can call these areas "seasonal ultra-cold traps", as they are similar to the seasonally-shadowed regions (SSRs) that radiate outward from PSRs and provide additional area where volatiles can be temporarily trapped (Kloos et al., 2019).

The results of this analysis are presented in Fig. 2.23 and Fig. 2.24. As expected, we can see a more complex story than that told by the maximum temperature map (Fig. 2.18). For example, we can see that even though the lowest maximum temperature modeled was 37 K, nearly the entire upscaled pixel is colder than that for most of the year, with the coldest regions spending about half the year in the 25 – 30 K range.

The fact that the relative abundances of the various species detected by LCROSS does not follow the pixel stability fraction either means that the abundances are decoupled from the surface temperatures (i.e. through subsurficial burial) or that there are significant differences in the volume of each species being delivered to Cabeus. Although the preponderance of evidence from orbital data strongly suggest the former, it is still interesting to consider the magnitude of the latter effect. If we divide the observed abundances by the pixel stability fraction we can obtain an "abundance per stable pixel", which tells us the concentration of each species (relative to water) that must be present in each pixel below the stability threshold to explain the measurements. Unfortunately, this analysis would not be particularly enlightening at the LCROSS impact site, as nearly all of the observed volatile species share the same cold-trapping area (though this may change if our model is improved to better agree with Diviner measurements).

Our results show that the small-scale structure of the lunar surface plays a critical role
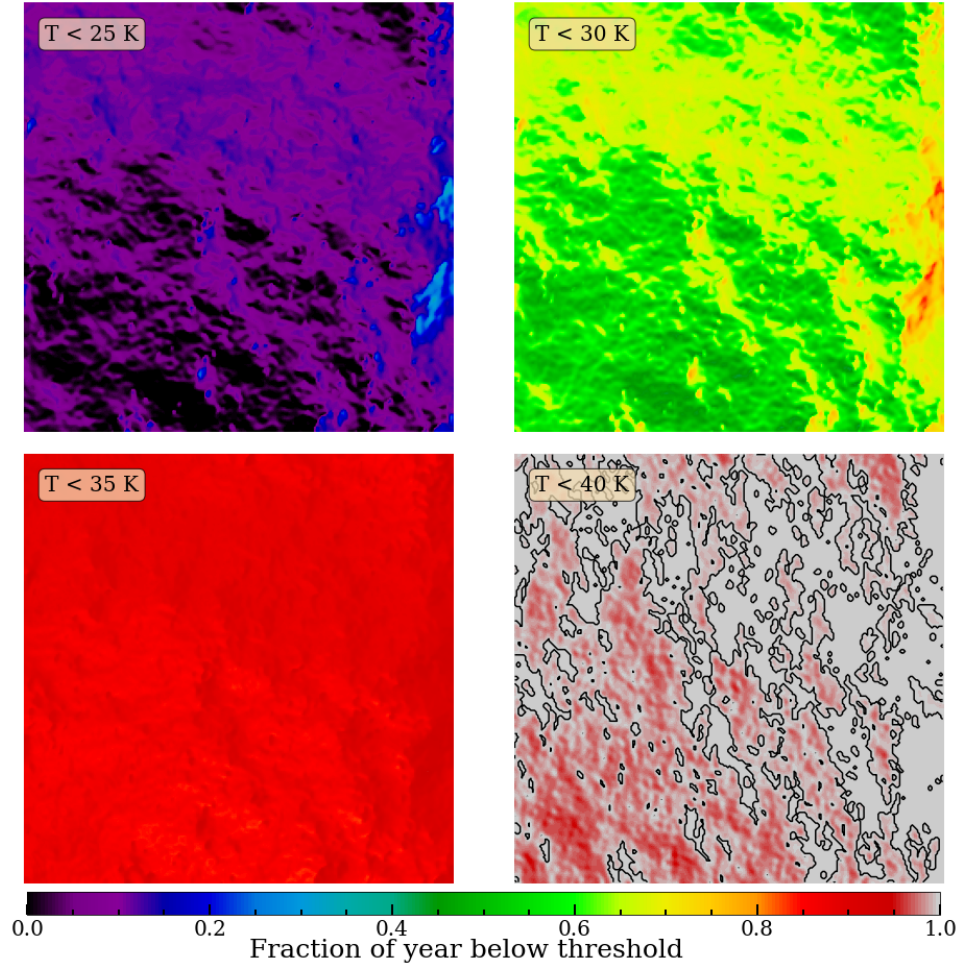
Figure 2.23: Seasonal variability of temperatures, as illustrated by the fraction of a year that each pixel spends below the threshold temperature specified at the top left of each panel. White regions denote the permanent ultra-cold traps, where the temperature never rises above the threshold.

in determining the thermal environment of PSRs, and thus the area available for the cold-trapping of various volatile species. Consequently, it is absolutely critical that we undertake further *in-situ* studies of volatile abundances at these scales before determining the appropriateness of a particular site for a permanently-crewed lunar base. Limiting ourselves to areas where volatiles are detected from orbit is likely too restrictive, and so should not necessarily be the first criteria upon which site selection is based.

It is important to note that our results are limited by the simplifying assumptions we made in our model. Although multiply-scattered light is unlikely to contribute much to the
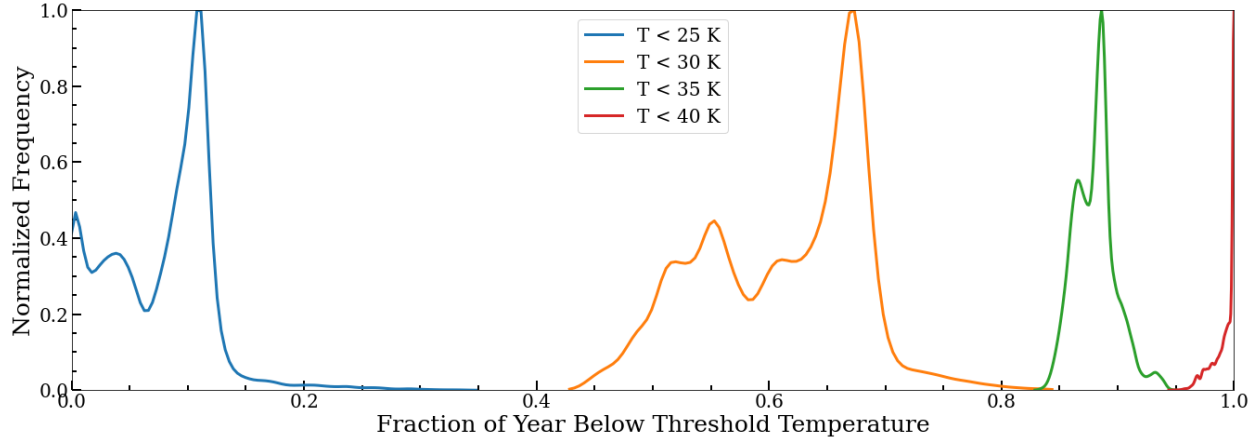
Figure 2.24: Histograms of the results in Fig. 2.23.

energy budget of micro ultra-cold traps, we are ignoring the thermal emissions from PSR terrain. Hayne et al. (2021) found that thermal emissions can increase the temperature of micro cold traps if the RMS slope increases beyond a certain threshold, so presumably a similar effect is at play here, albeit to a lesser degree thanks to the significantly lower temperatures of PSR terrain relative to sunlit terrain. Still, the general point that we cannot necessarily make assumptions about volatile abundances at human scales based on > 100 metre resolution orbital data remains valid.

Chapter 3

The Scattering Phase Function of Martian Water-Ice Clouds

3.1 Datasets and Methods

3.1.1 MSL Navigation Cameras

All of the observations to be discussed in this thesis were taken using MSL's Navigation Cameras (Navcams), of which the rover has two pairs (one pair each for the primary and backup computers) mounted on the remote sensing mast (RSM). Although officially classified as engineering cameras as their primary purpose is to assist in rover navigation, the Navcams are radiometrically calibrated, meaning that they can also be used to conduct scientific observations.

The Navcam sensors are flight-ready spare charge-coupled devices (CCDs) left over from the Mars Exploration Rover missions. They have a useful photosensitive area of 1024 x 1024 pixels and are capable of imaging a 45° x 45° region of the sky. The optical filter bandpass of each Navcam is centered around 650 nm, with sensitivity between 600 – 800 nm. Although this spectral range is less ideal for the imaging of WICs than that of the rover's other cameras (i.e. the Mast Camera), the Navcams were selected for their superior
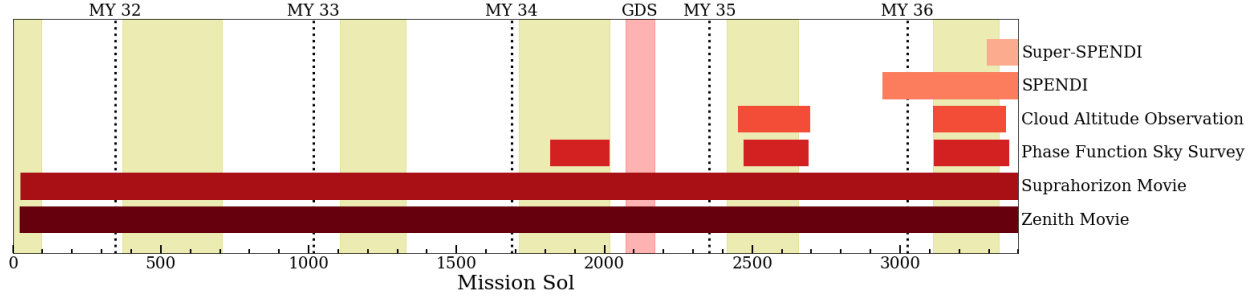
Figure 3.1: Evolution of the MSL cloud observation campaign over the mission to date. Yellow shaded regions indicate the ACB season. The red shaded region indicates the MY 34 GDS.

operational signal-to-noise ratio (>200:1)

3.1.2 Cloud Movies

MSL's cloud observation campaign has evolved significantly over the course of the mission, as can be seen in Fig. 3.1. This thesis will be focusing on the two longest-running portions of the campaign: the Zenith and Suprahorizon movies (ZMs and SHMs).

Since sol 1032, the ZMs and SHMs have been identical, save for their pointings. (Before sol 1032, the size, length, and pointing of the SHMs varied in response to shifting scientific objectives.) Each consists of eight frames taken across 266 seconds. ZMs are pointed at an elevation angle of 85°, while SHMs point just over the crater rim at 26°. Depending on the time of year, the azimuthal angle is adjusted to either due north (0°) or due south (180°) to point away from the general direction of the Sun, which appears in the northern sky during winter and in the southern sky during summer. Since sol 2453, the ZMs and SHMs have been downlinked at their full resolution rather than being subject to the 2x2 pixel binning that had occured up to that point, resulting in half-resolution images with a quarter as many pixels.

Both movies are acquired on a regular cadence (every 3-4 sols for the ZMs and every 2-3 sols for the SHMs). The slower cadence of the ZMs is a consequence of the rover's location close to the equator. At low latitudes, the Sun passes nearly directly overhead each day, well
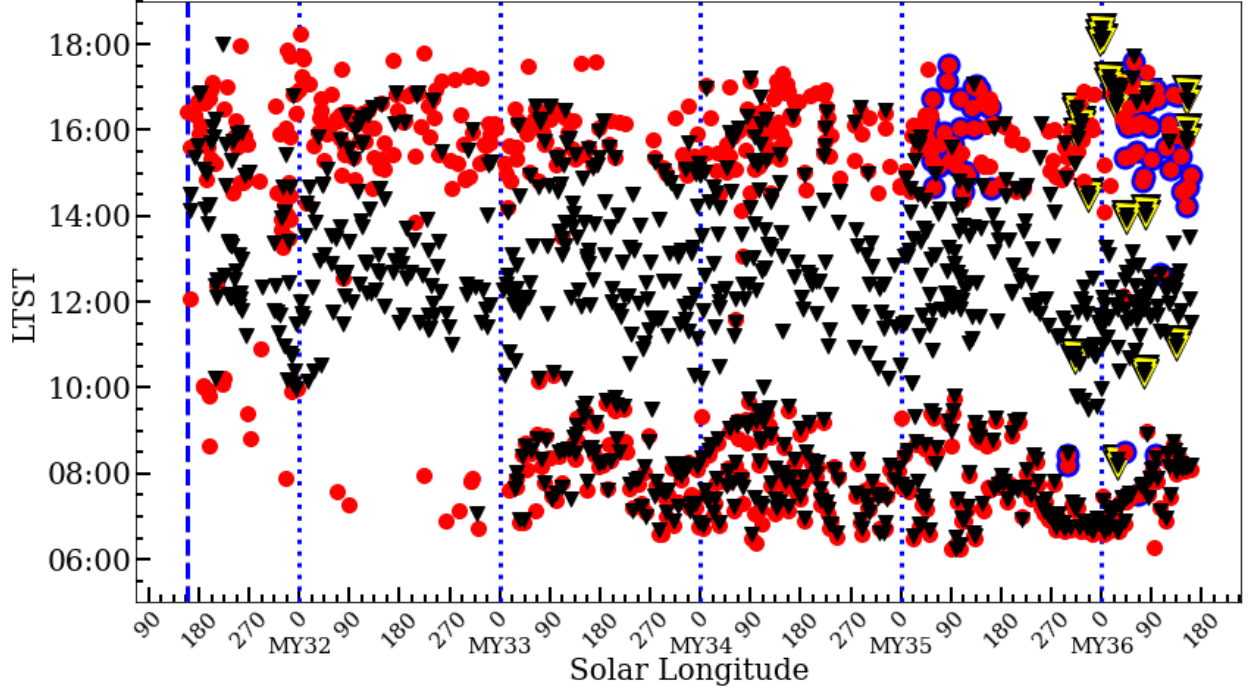
Figure 3.2: The temporal distribution of ZMs (red circles) and SHMs (black triangles) taken during the first five MYs of the mission. The highlighted markers indicate CAO ZMs and SPENDI/Super-SPENDI SHMs.

within the Navcam FOV. As a result, we are limited to taking ZMs more than 2.5 hours from local noon, which can be a challenge given that operational constraints onboard the rover typically result in science time being allocated in the middle of the day. SHMs are not subject to this constraint and thus can be taken at any time of day.

For the first $\sim$ year-and-a-half of the mission, the diurnal coverage of the cloud campaign was further limited by the infrequent availability of science time in the early morning. Beginning in MY 33, a once-weekly science block dedicated to environmental science observations was implemented, allowing us to cover the full day from 06:00 to 18:00 LTST (with the exception of a small period in the late morning that is the result of the rover's uplink schedule precluding science observations). The full temporal distribution of the movies can be seen in Fig. 3.2.

During the most recent two MYs, several new observations were introduced that have allowed us to expand our ZM and SHM cadence during the ACB season: the Cloud Al-

67

titude Observation (CAO) and the Shunt Prevention ENV Navcam Drop-In observation (SPENDI/Super-SPENDI). The CAO is executed once a week between 14:30 and 16:00 LTST during the ACB season, and is designed to measure the altitude of clouds passing above the rover. It consists of two movies taken jointly, one of which is identical to the standard ZMs. The SPENDI/Super-SPENDI observations were designed as "shunt prevention" activities to partially drain the rover's battery to prevent it from sitting fully-charged for an extended period of time. They both take movies at six different pointings, two of which are similar to the SHM pointings: (az, el) = (0°, 15°) and (180°, 25°). The CAO and SPENDI/Super-SPENDI observations are noted on Fig. 3.2 as the outlined markers.

3.1.3 Opacity Determination

Because the clouds observed over Gale Crater are typically very optically thin, it is extremely difficult (if not completely impossible) for the human eye to observe them in the movies as they are delivered to us from the rover. To enhance their visibility, we apply a technique known as mean-frame subtraction (MFS). First, a pixel-by-pixel mean frame is created by averaging all eight frames together. The mean frame is then subtracted from each of the raw frames individually. The end result is that the static portion of each frame is removed, leaving behind only the component that varies with time (i.e. the clouds). As a final step, we stretch each frame using the second and ninety-eighth percentiles of intensities as the minimum and maximum values. (Note that stretching is done solely to assist in the identification of cloud features; all analysis is performed using the un-stretched MFS frames.) An example of a ZM following each of these steps is given in Fig. 3.3.

Once each movie has been processed, it is assigned a quality value between 0 (featureless) and 10 (clouds visible in the raw frames). A value of -1 is also used to indicate movies that are unusable, either due to the presence of the Sun in the frame or an RSM failure that left the Navcams pointing in a direction where the sky could not be observed. Movies with quality values of -1 or 0 are excluded from further analysis.
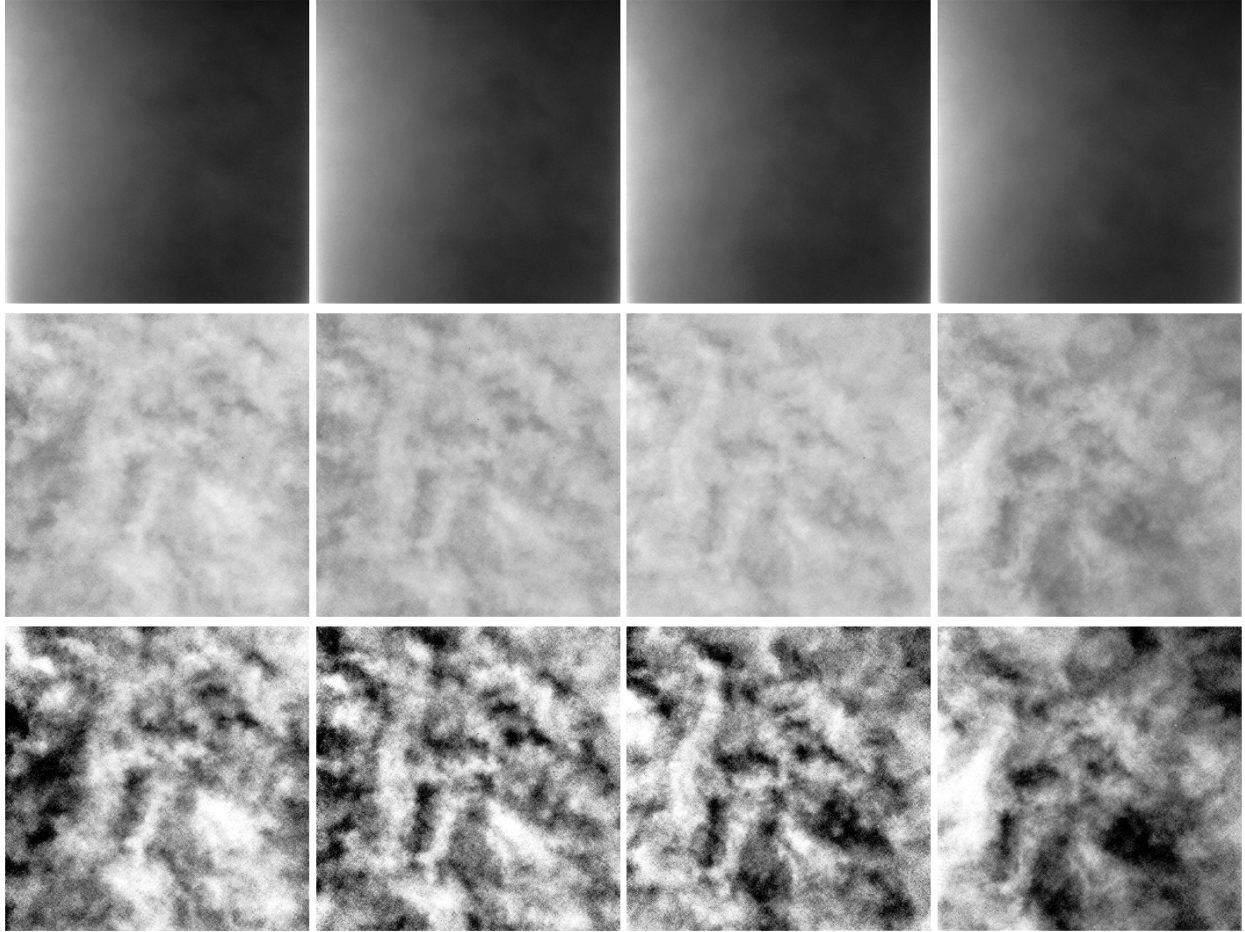
Figure 3.3: Four frames from a ZM, shown before (top) and after (middle) MFS has been performed, as well as once image stretching has been applied (bottom).

To determine the opacity of clouds observed in the movies, one of two equations is used, depending on the time of year when the movie was taken. The two equations, referred to as the *high-clouds* and *whole atmosphere* formulae, make different assumptions about the physical properties of the clouds being observed. For the purpose of this thesis, we will be focusing on the high-clouds formula, which assumes that we are observing high-altitude non-dusty clouds, consistent with what is expected during the ACB season.

To derive the high-clouds formula, we begin with the equation of radiative transfer:

$$\mu \frac{dI(\tau, \mu, \phi)}{d\tau} = I(\tau, \mu, \phi) - J(\tau, \mu, \phi) \tag{3.1}$$
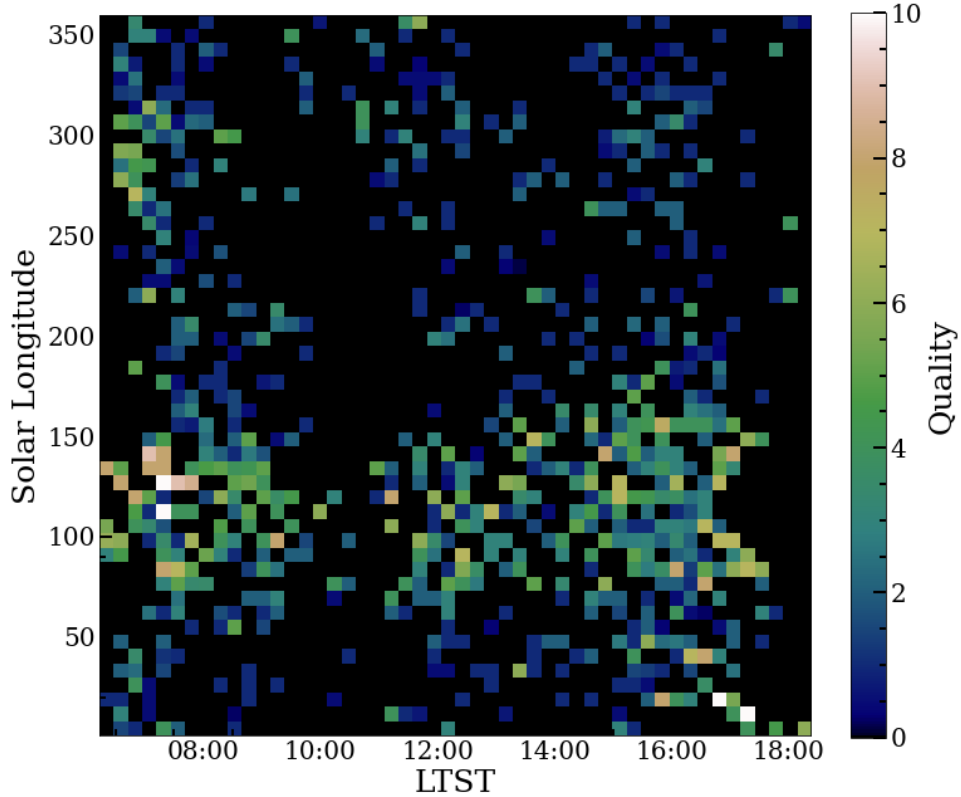
Figure 3.4: ZM and SHM quality values averaged across 50 bins of solar longitude and LTST. The ACB season is clearly visible as a band of higher-quality movies between $L_s \approx 50° - 170°$. A second smaller peak centred around $L_s = 300°$ is due to increased dust clouds at the peak of the dusty season.

In this equation, μ and ϕ are the cosines of the zenith and azimuthal viewing angles, respectively, and τ is the optical depth. $I(\tau, \mu, \phi)$ is the observed radiance at a particular optical depth, and $J(\tau, \mu, \phi)$ is the source function at the same optical depth. The source function can be simplified by assuming that single scattering dominates over multiple scattering (a valid assumption to make given the clouds' low opacity), and that all of the scattered light originates from the sun, rather than upwardly-scattered radiation from the ground. The latter of these assumptions can be justified given that the diffuse ground radiation is invariant across the Navcam FOV, so it will be removed from the image once MFS is applied. The source function is then:

$$J(\tau, \mu, \phi) = \frac{\omega}{4\pi} F P(\Theta) \exp\left(-\frac{\tau}{\mu_0}\right) \tag{3.2}$$

where ω is the single scattering albedo (assumed to be 1; Liou, 1992; Moores et al., 2015), $P(\Theta)$ is the scattering phase function, and $\mu0$ is the cosine of the solar elevation angle.

Because the clouds are at high altitudes, we can assume that no scattering occurs above the clouds and that all of the observed radiance is the result of scattering within the clouds. By combining this with our prior assumption that the clouds are optically thin, we can find that the scattered radiance from the clouds is (Kloos et al., 2016):

$$I(\tau, \mu, \phi) = \frac{\Delta\tau}{4\pi\mu}FP(\Theta) \tag{3.3}$$

Finally, we need to multiply this equation by the spectral bandpass of the Navcam ($\Delta\lambda$ = 250 nm) and account for the additional attenuation caused by dust in the atmosphere between the clouds and the rover. We can determine the latter of these using τ_{COL}, the atmospheric column density as measured by Mastcam imaging of the solar disc (Lemmon, 2014). With these terms included and rearranging to solve for the cloud optical depth, the final form of the high-clouds formula is:

$$\tau_{HC} = \frac{4\pi\mu I_{\lambda,VAR}\Delta\lambda}{P(\Theta)F_\lambda \exp\left(-\frac{\tau_{COL}}{\mu}\right)} \tag{3.4}$$

Note that $I(\tau, \mu, \phi)$ has been substituted for $I_{\lambda,VAR}$, the difference between a high- and low-radiance point in a MFS frame. These two points, corresponding to a cloudy and cloudless (or nearly-cloudless) portion of the image, respectively, are chosen through visual inspection, as seen in Fig. 3.5.

This equation was used without incident by Moores et al. (2015), Kloos et al. (2016), and Kloos et al. (2018) to construct a record of ACB cloud opacities covering the first two MYs of the MSL mission. Our initial analysis of MY 34–36 using this same equation produced mean opacities much higher than those for MY31–33, inconsistent with the known repeatability of the ACB. A quick examination revealed that rather than all of the opacities being uniformly higher, the MY 34-36 data contained an anomalously large number of extremely high-opacity

71
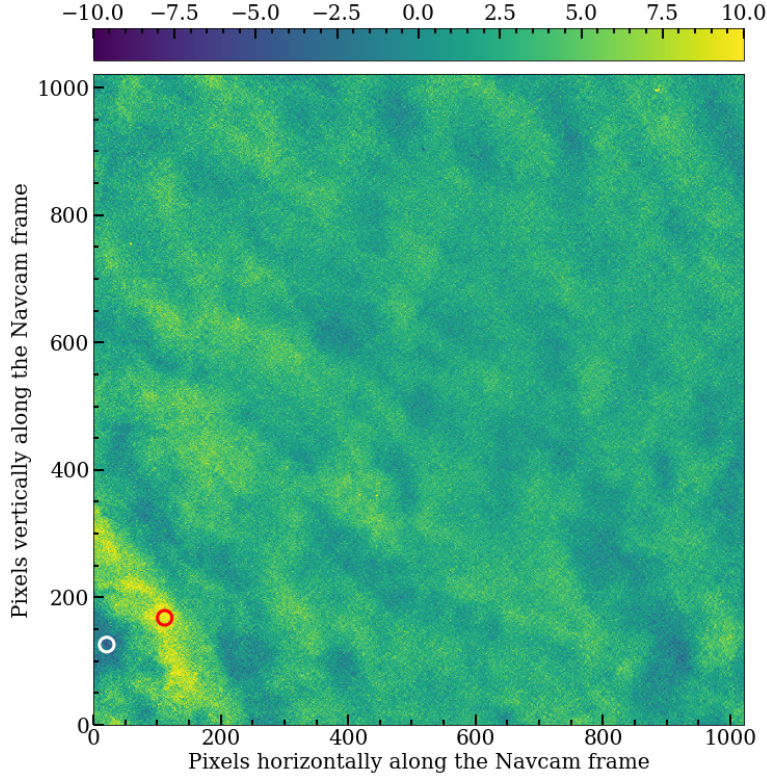
Figure 3.5: An example radiance map of the time-variable component of frame 5 of the sol 2633 ZM. The high and low radiance points are indicated by the red and white markers, respectively.

clouds (see Fig. 3.6). After a closer inspection of the offending movies, we realized that the highest-opacity clouds were generally occurring in movies where the Sun was close to the edge of the frame. When combined with the PFSS results, this led us to realize that the assumption of a flat phase function was inappropriate.

3.1.4 Finding a Scattering Phase Function

The high-clouds formula can be rearranged to solve for the scattering phase function, rather than the opacity:

$$P(\Theta) = \frac{4\pi \mu I_{\lambda,VAR}\Delta\lambda}{\Delta\tau F_\lambda \exp\left(-\frac{\tau_{COL}}{\mu}\right)} \tag{3.5}$$

Eq. 3.5 is nothing new; indeed, it is the same equation used by Cooper et al. (2019) and Innanen et al. (2021) to derive a phase function using the PFSS. As such, we face the
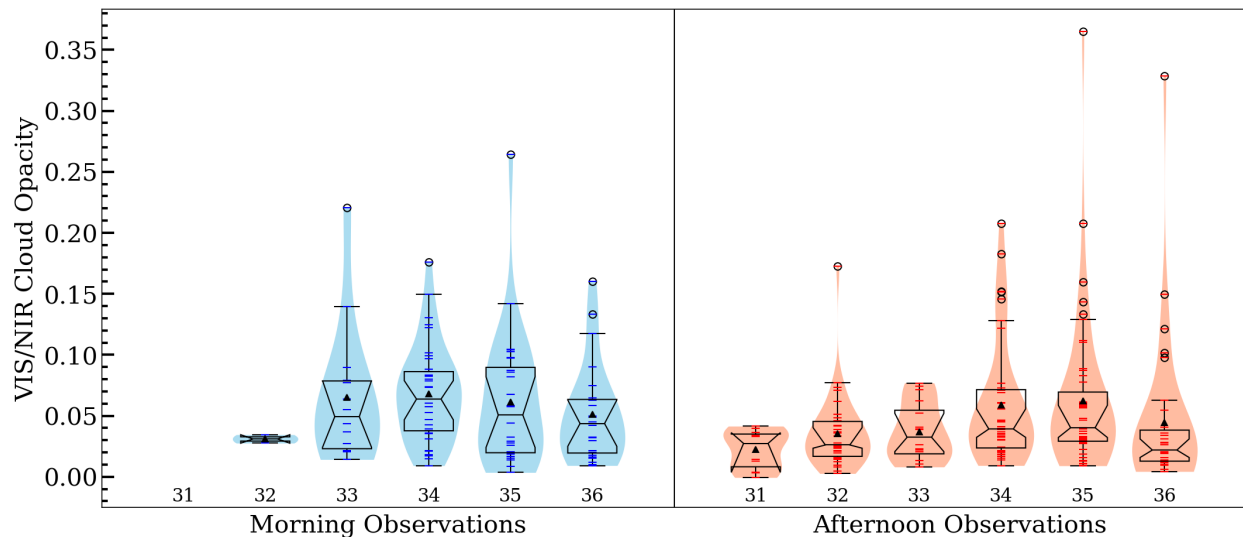
Figure 3.6: Calculated opacities for the first five MYs of the MSL mission. Note how the averages for MY 34-36 are being pulled upward by a small number of extremely high opacity measurements, particularly in the afternoon.

same problem they did, in that we must assume a cloud opacity. Rather than using data from MCS or any other mission, we instead choose to use the values calculated using the high-clouds formula, but *only over the range where the assumption of a flat phase function holds.*

As Fig. 3.7 shows, the high-clouds opacities do not begin trending upward until Sunward of $\sim 60°$. At larger scattering angles, the opacity curve is roughly flat, consistent with our expectations given the low variability of the ACB. This means that these values can be used to determine a "true" mean opacity, which we can use as an input to Eq. 3.5.

To account for the known diurnal variability and to permit for the possibility of interannual variability given the MY 34 GDS, we divide all of our opacities by MY and by time of day, resulting in six datasets. A mean opacity is calculated for each using values at scattering angles $> 70°$, the results of which are given in Table 3.1.4 and Fig. 3.8. Interestingly, we do not see the higher morning opacities reported by Kloos et al. (2016). In fact, the only significant diurnal difference observed is in MY 34, when the *afternoon* clouds are thicker than those in the morning.
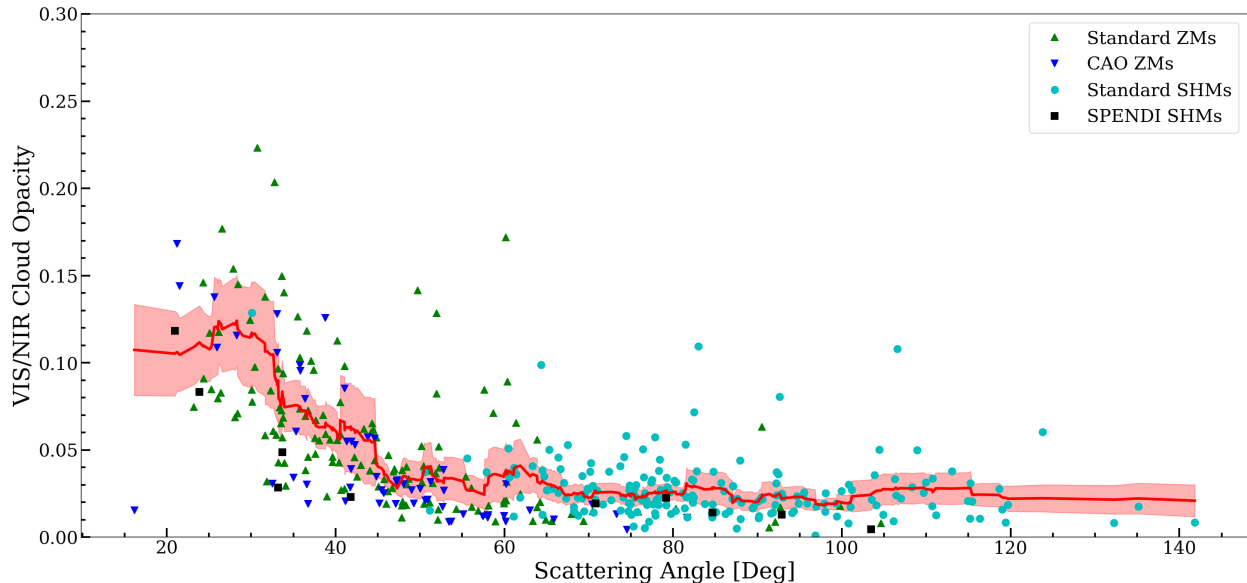
Figure 3.7: Calculated high-clouds opacities as a function of scattering angle. The upward turn at low scattering angles is indicative of a breakdown in our model's assumptions.

	Mars Year		
Time	33	34	35
Morning	0.028 ± 0.02	0.021 ± 0.02	0.023 ± 0.01
Afternoon	0.024 ± 0.01	0.029 ± 0.02	0.022 ± 0.01

Table 3.1: Calculated mean cloud opacities for MY 34 – 36 using points at scattering angles $> 70°$.

Once we have found our mean opacities, we next have to find the scattering angle at the points where we measured the opacity in each movie. Because the Sun is sufficiently far away that we can consider it to be located at infinity, we can assume that the solar position vectors at the Navcam and the cloud are parallel. Under this assumption, the scattering angle Θ at the centre of the Navcam frame is the angle between the solar position vector and the Navcam pointing, as is illustrated in Fig. 3.9. The azumuth and elevation of both the Sun and the Navcam pointing are recorded in the PDS label, so it is relatively trivial to find this angle in 3D space:

$$\cos(\Theta) = \cos(\theta_{\odot})\cos(\theta_N) + \sin(\theta_{\odot})\cos(\theta_N)\cos(\phi_N - \phi_{\odot}) \tag{3.6}$$

74
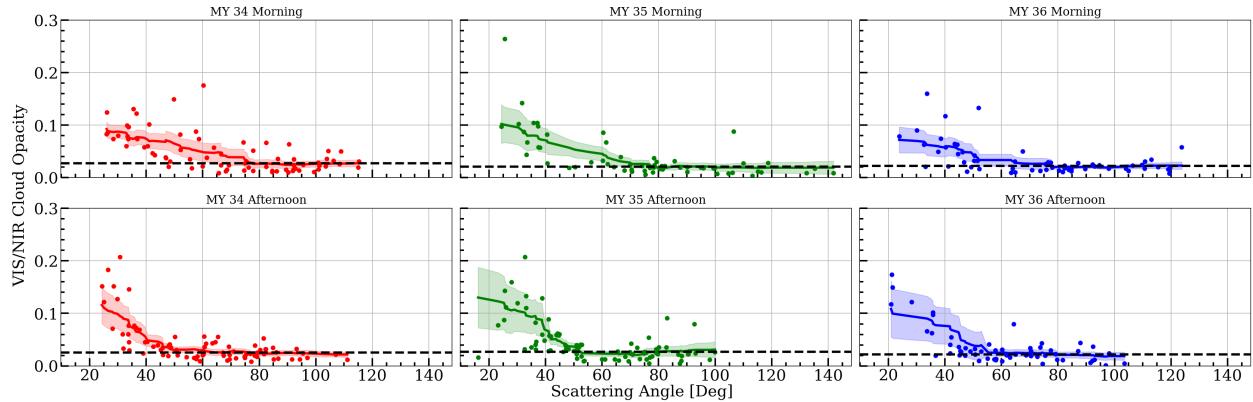
Figure 3.8: Morning and afternoon opacities for MY 34 – 36. The dashed line in each panel represents the previously-assumed value of 1/15. We see fairly consistently that the values at high scattering angles cluster around 1/15 before rapidly increasing Sunward of 50-80°.

where θ_N, $\theta_\odot$, ϕ_N, and $\phi_\odot$ are the zenith and azimuth angles of the Navcam and Sun, respectively.

If the camera's FOV is sufficiently small, the central scattering angle is a good approximation of the scattering angle across the entire frame. This is not the case for the Navcams. Because they have a FOV of 45°, the scattering angle can vary by almost 70° across diagonal corners of the frame. Consequently, we need some way to determine the azimuth and elevation of each pixel in the image.

For this purpose, we can use a camera model. A camera model uses a set of vectors and scalars that describe the optical properties of a particular camera, allowing for conversions to be made between real-world 3D coordinates and image coordinates and back. The MSL Navcams use a CAHVOR model, named after the elements that comprise it:

- $\vec{C}$: The 3D coordinates of the camera's focal point.

- $\vec{A}$: A vector normal to the plane of the camera's sensor.

- $\vec{H}$: The horizontal information vector.

- $\vec{V}$: The vertical information vector.

- $\vec{O}$: The optical axis unit vector.
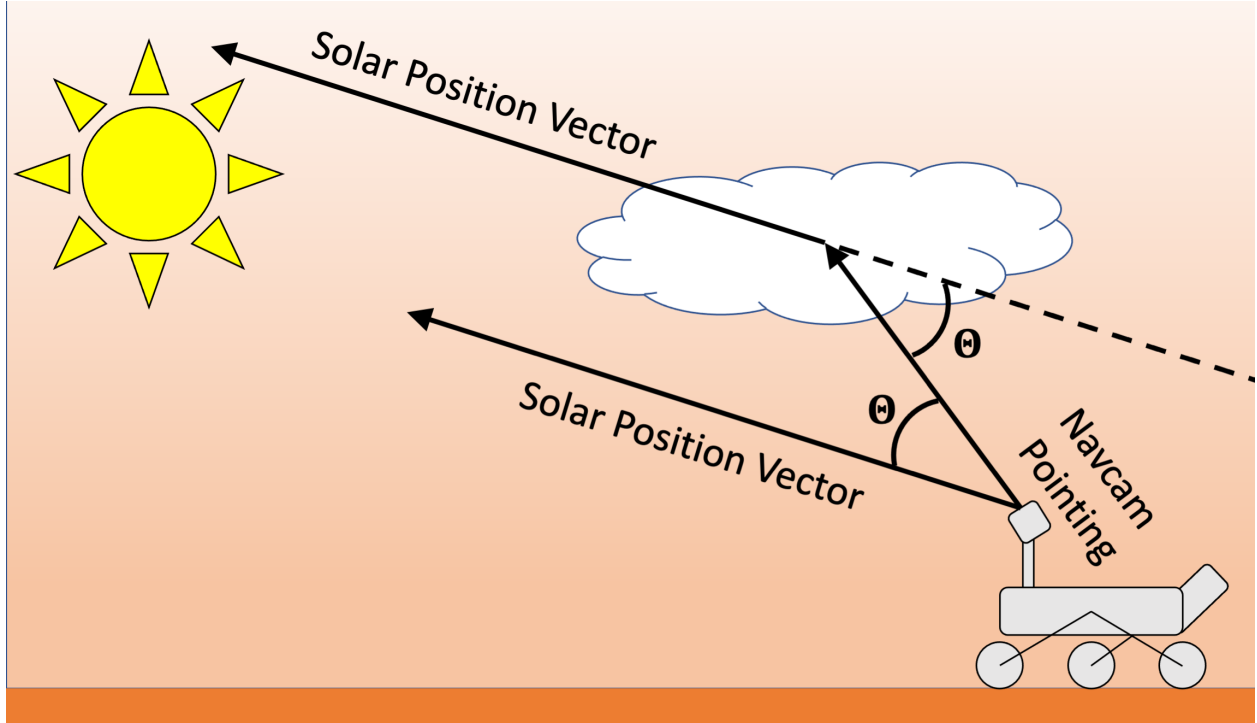
Figure 3.9: Diagram of the scattering angle geometry, illustrating how in the assumption of the Sun at infinity, the scattering angle is equivalent to the angle between the solar position vector and the Navcam pointing.

- R : Radial lens distortion coefficients.

Because the Navcams are fairly linear and the CCD image plane is nearly perfectly perpendicular to the pointing of the camera, $\vec{O}$ is approximately the same as $\vec{A}$ and the values contained in R are small. Thus, the CAHVOR model can be simplified to a linear CAHV model without much loss of accuracy. All of the model elements are provided in the PDS label that accompanies each image.

In the CAHV model, the Cartesian coordinates of a vector perpendicular to a pixel located at (i, j) are given by:

$$(x, y, z) = \vec{C} - \left[(\vec{V} - j\vec{A}) \times (\vec{H} - i\vec{A}) \right] \tag{3.7}$$

The Cartesian coordinates can then be transformed to elevation and azimuth angles through the usual means. Before doing so, we must note that the coordinates derived
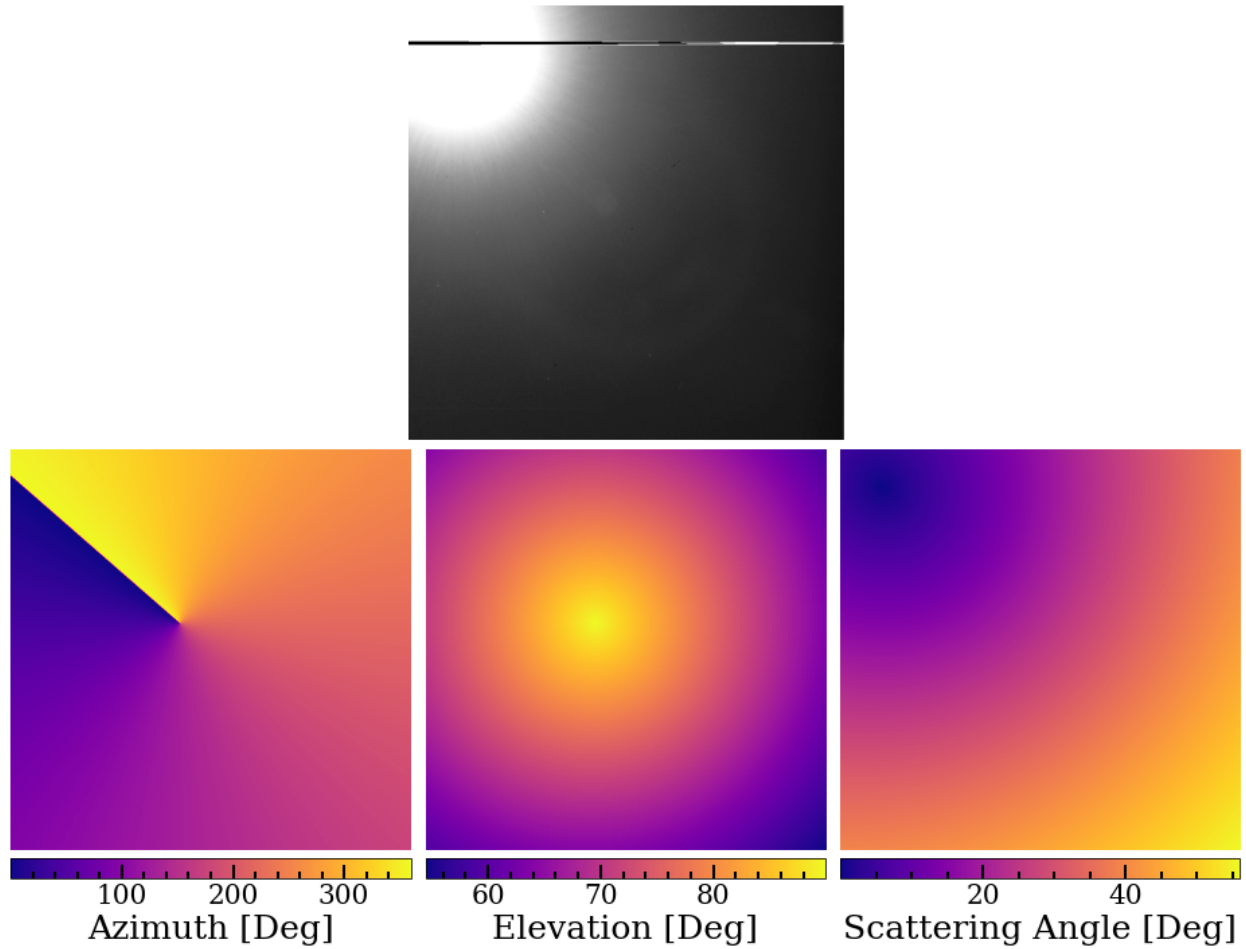
Figure 3.10: Azimuth, elevation, and scattering angles for a ZM taken on sol 3106. Although this movie was rendered unusable by the presence of the Sun in the frame, we can see that the scattering angle approaches zero near the Sun, as we expect.

through these means are in the rover navigation frame, while we typically work in the site frame. Fortunately, the PDS label also includes a quaternion to transform between the two reference frames with ease. The final result can be seen in Fig. 3.10.

3.2   Results and Analysis

In total, we have a total of 515 ZMs and SHMs during the MY 33–36 ACB seasons with visible clouds; 229 with opacities measured at scattering angles greater than 60° and 183 measured at scattering angles less than 60°.

To quantify the goodness-of-fit between our new phase functions and those that have been previously calculated, we can use the coefficient of determination:

$$R^2 = 1 - \frac{RSS}{TSS} \tag{3.8}$$

In this equation, RSS is the residual sum of squares and TSS is the total sum of squares, with higher values of R^2 indicating a better fit.

Before we can determine R^2, we have to normalize the curves. Ordinarily, phase functions are normalized such that the total area under the curve (from $0°$ to $180°$) is 4π. However, because we don't observe the full range of scattering angles, it is not possible to normalize our phase functions in this way. Previous works using the PFSS instead chose to normalize the phase functions by the value of a previously-derived phase function (Clancy et al. (2003) for Cooper et al. (2019) and Cooper et al. (2019) for Innanen et al. (2021) and Innanen et al. (2022)) at the median observed scattering angle. We can do this because when comparing two phase functions, their relative shapes are more important than their actual values. However, we do still have to choose a reasonable normalization value. Our early analysis suggested that the previous method for doing so was resulting in unfairly poor R^2 values. Instead, we will be normalizing our phase functions by the mean value of the MY 34-36 PFSS phase functions over the range of scattering angles where the assumption of a flat phase function holds, as we expect the PFSS and ZM/SHM phase functions to have approximately the same value there.

3.2.1 Interannual and Diurnal Variability

Thanks to the large number of points we have analyzed, it is possible to divide the data into morning and afternoon pairs for each MY, allowing us to examine whether or not the shape of our phase functions varies either diurnally or interannually. The results of this division are shown in Fig. 3.11 and Fig. 3.12.
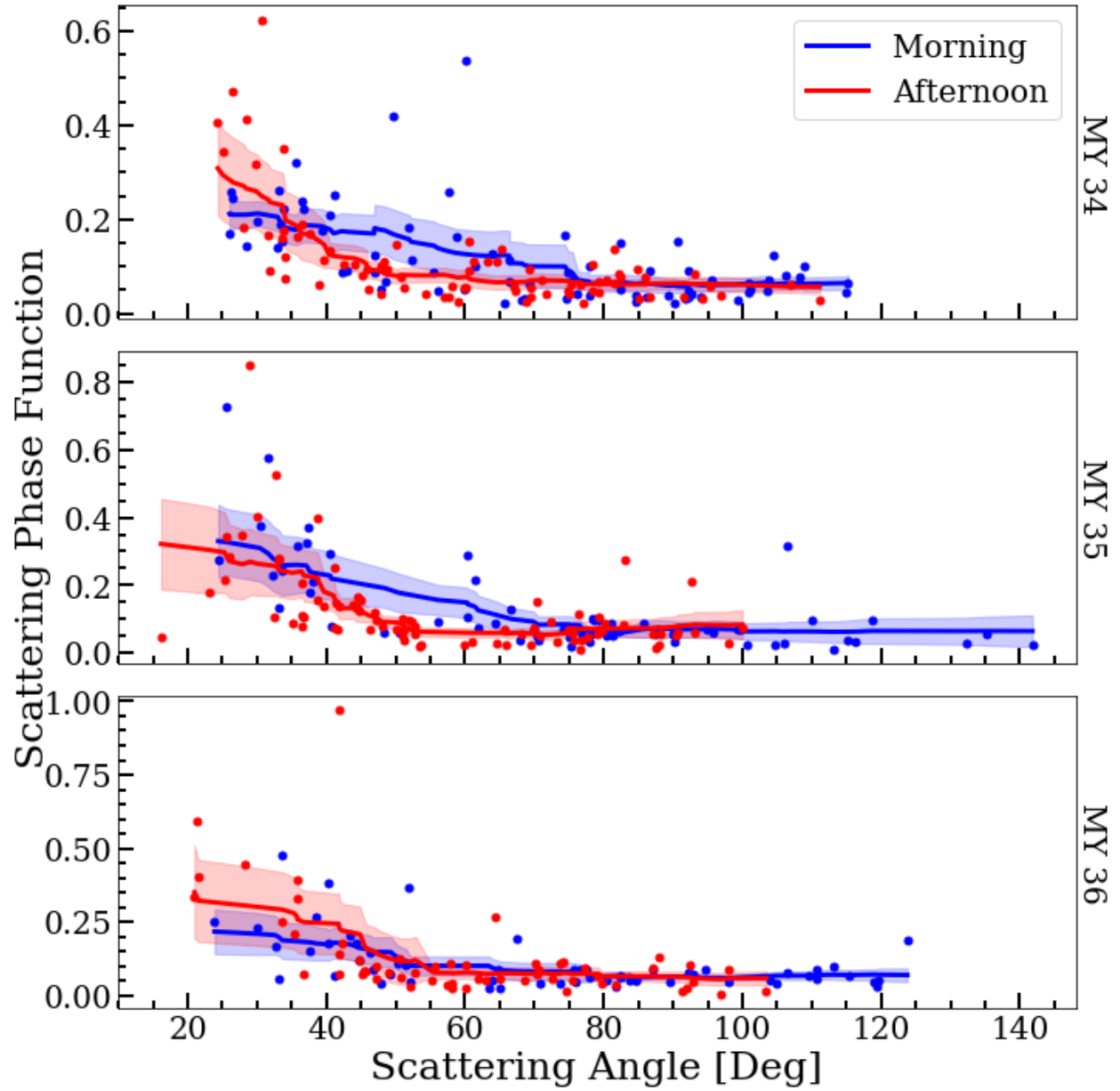
Figure 3.11: A comparison between AM and PM phase functions for MY 34 – 36.
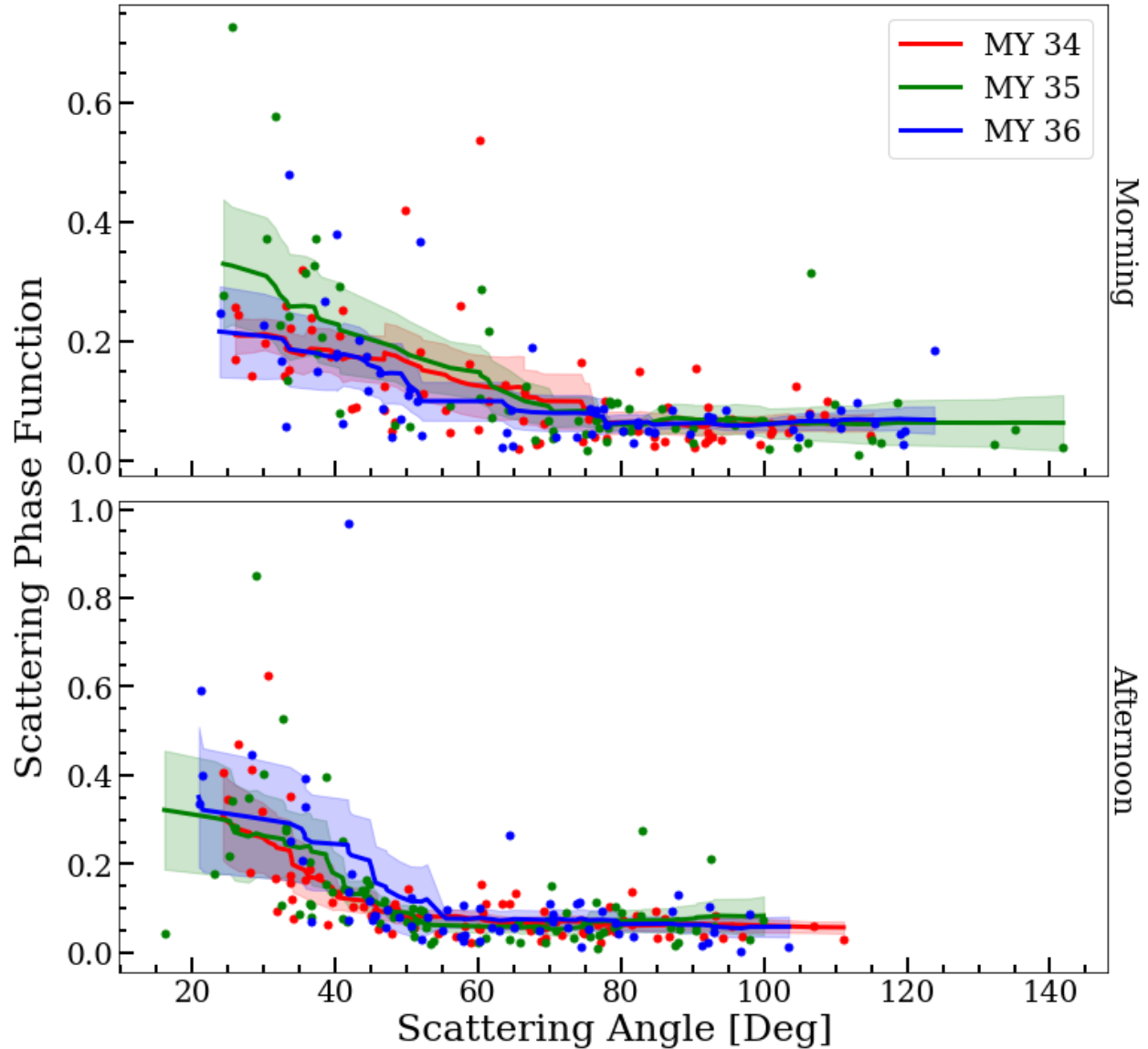
Figure 3.12: An interannual comparison of AM and PM phase functions, showing good agreement from year to year.

In Fig. 3.11, we can see that in MY 34 and MY 35, the morning and afternoon phase functions fall slightly outside of the other's 95% confidence interval for scattering angles between 40° – 60°, suggesting that there could be a significant diurnal difference. However, we are hesitant to come to this conclusion for several reasons. First, the apparent difference vanishes in MY 36, where the morning and afternoon phase functions follow each other

closely. Although this could be indicative of some degree of interannual variability, Fig. 3.12 suggests that this isn't the case. Here, we can see that the morning and afternoon curves for all three MYs fall within the 95% confidence interval, allowing for the possibility that the MY 34 and 35 morning phase functions are more consistent with the MY 36 morning phase function than they first appear.

Because we do not see significant diurnal variability in the phase functions, the remainder of our analysis will be conducted by combining the morning and afternoon phase functions into a single phase function for each MY.

3.2.2 Comparison With Other Phase Functions

There are three sets of phase functions that we can compare our results with, each of which will yield a difference piece of information. First, we can compare with the PFSS phase functions. We would expect these to be most similar to our phase functions, as the PFSS, ZMs, and SHMs observe the same clouds at the same location using the same camera on the same rover. Second, we can compare with phase functions that have been measured by other Martian missions, including both clouds and dust. This will allow us to see if our results are consistent with those elsewhere on the planet and to explore potential methodological challenges if they are not. Finally, we can compare with modeled phase functions of various ice crystal geometries, from which we can determine if Martian WICs have a dominant crystal habit. The results of the R^2 are presented in Table 3.2.2 and visually in Figs. 3.13 and 3.15, and will discussed in greater detail in the following sections.

Spacecraft-Derived Phase Functions of Martian Clouds

In this section, we will be comparing our phase functions with those that have previously been derived other Martian missions. Specifically, we will be looking at polar and midlatitude water-ice clouds from the Viking missions (Clancy and Lee, 1991) and aphelion clouds from the Thermal Emission Spectrometer (TES) onboard the Mars Global Surveyor (Clancy et al.,

Comparison Phase Function	MY 34	MY 35	MY 36
MY 34 PFSS	-1.195	-2.292	-1.030
MY 35 PFSS	0.186	-0.755	-0.160
MY 36 PFSS	0.619	0.566	0.755
Dust (Pathfinder)	0.753	0.067	0.492
Dust (Viking)	0.700	0.064	0.451
Midlatitude Clouds	0.827	0.876	0.740
Polar Clouds	0.877	0.908	0.791
Type 2A Aphelion Clouds	0.608	0.126	0.326
Type 2B Aphelion Clouds	0.524	0.095	0.305
Aggregates	0.883	0.902	0.740
Bullet Rosettes	0.507	0.461	0.348
Droxtals	0.377	0.380	0.290
Hollow Columns	0.648	0.604	0.373
Plates	0.767	0.670	0.611
Solid Columns	0.552	0.444	0.310
Spheres	0.718	0.785	0.650

Table 3.2: R^2 values for the comparison between our three modeled phase functions and other modeled phase functions for Martian and terrestrial water-ice and dust clouds.

2003), as well as dust phase functions derived from Viking (Clancy and Lee, 1991) and Pathfinder (Tomasko et al., 1999) data. We will also be comparing our results to those of the PFSS observation executed onboard MSL over the past three ACB seasons (Cooper et al., 2019; Innanen et al., 2021, 2022).

Because we are observing aphelion clouds, we would expect to see the best fit with the TES aphelion cloud phase functions. However, this is generally not the case, with R^2 values ranging from 0.095 to 0.608 between the two types of aphelion clouds across the three MYs we examined, indicating poor to moderate agreement. Looking at Fig. 3.13, we can see the likely cause for the poor agreement. Though both our phase functions and the TES phase functions show a similar Sunward increase at scattering angles below $\sim 60°$, the TES curves increase beyond $\sim 90-100°$ towards the 180° backscattering peak, while our phase functions remain flat.

The dust and Viking phase functions perform moderately better than the TES phase functions (with the exception of MY 35), with the Viking curves having R^2 values between
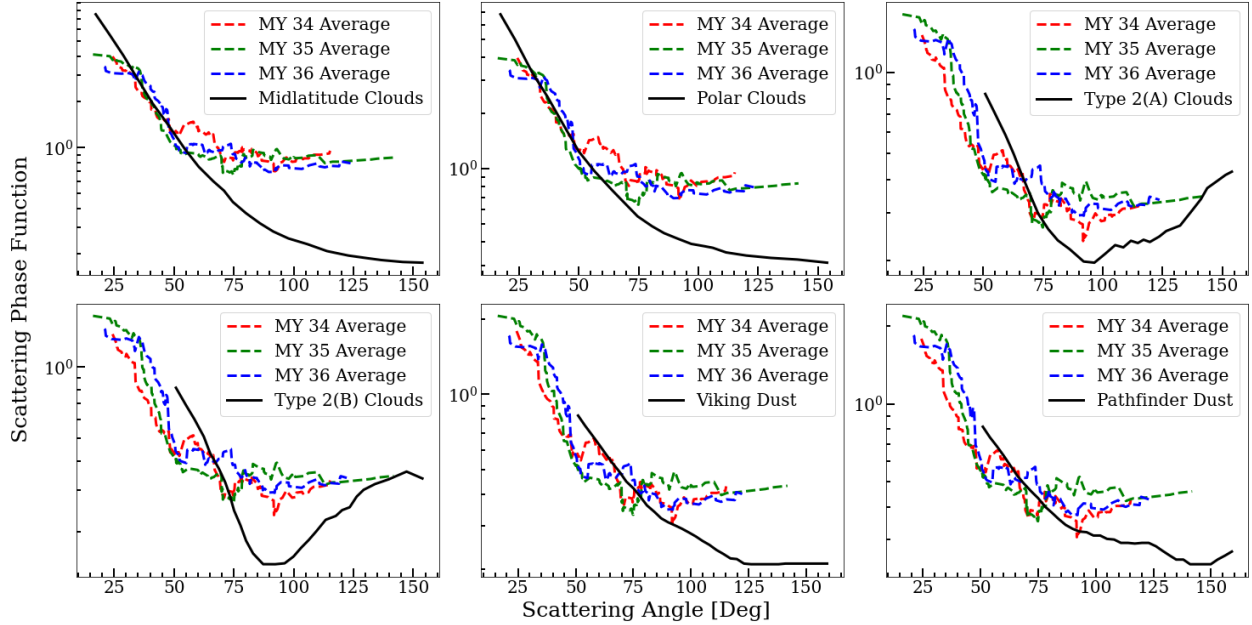
Figure 3.13: Comparing our three phase functions with six cloud and dust phase functions derived from Pathfinder, Viking, and TES data. Although similarly smooth to our phase functions, none appear to display the flattening out behaviour that we observe.

0.7 and 0.9. Unlike the TES results, these phase functions begin to flatten out, though they do so $\sim 20°$ later than our phase functions and generally continue downward (albeit at a reduced rate) rather than reaching a constant value. We do note that the difference in magnitude is somewhat exaggerated by the log scale used in Fig. 3.13, so the difference at scattering angles $> 60°$ is not as large as it may appear.

Finally, we can compare our results to the phase functions derived using the PFSS. Because both the PFSS and ZMs/SHMs are executed onboard MSL using the rover's Navcams, we would expect that they would show similar results. Instead, we see the worst agreement of any of the spacecraft-derived phase functions, with negative values of R^2. In Fig. 3.14, we can see why this is. Although both sets of phase functions flatten out at large scattering angles, our newly-derived phase functions do not begin to increase until we look approximately 20° closer to the Sun than increase seen in the PFSS curves. Additionally, the PFSS phase functions display some unusual behaviour at small scattering angles, either decreasing in value (MY 34), flattening out (MY 35), or neither (MY 36). In general, we expect to see

an increase in the forward scattering direction, so we are more inclined to believe our results than those of the PFSS. As we will discuss later, we suspect that this difference may be the result of a small but important difference in the construction of the two observations.
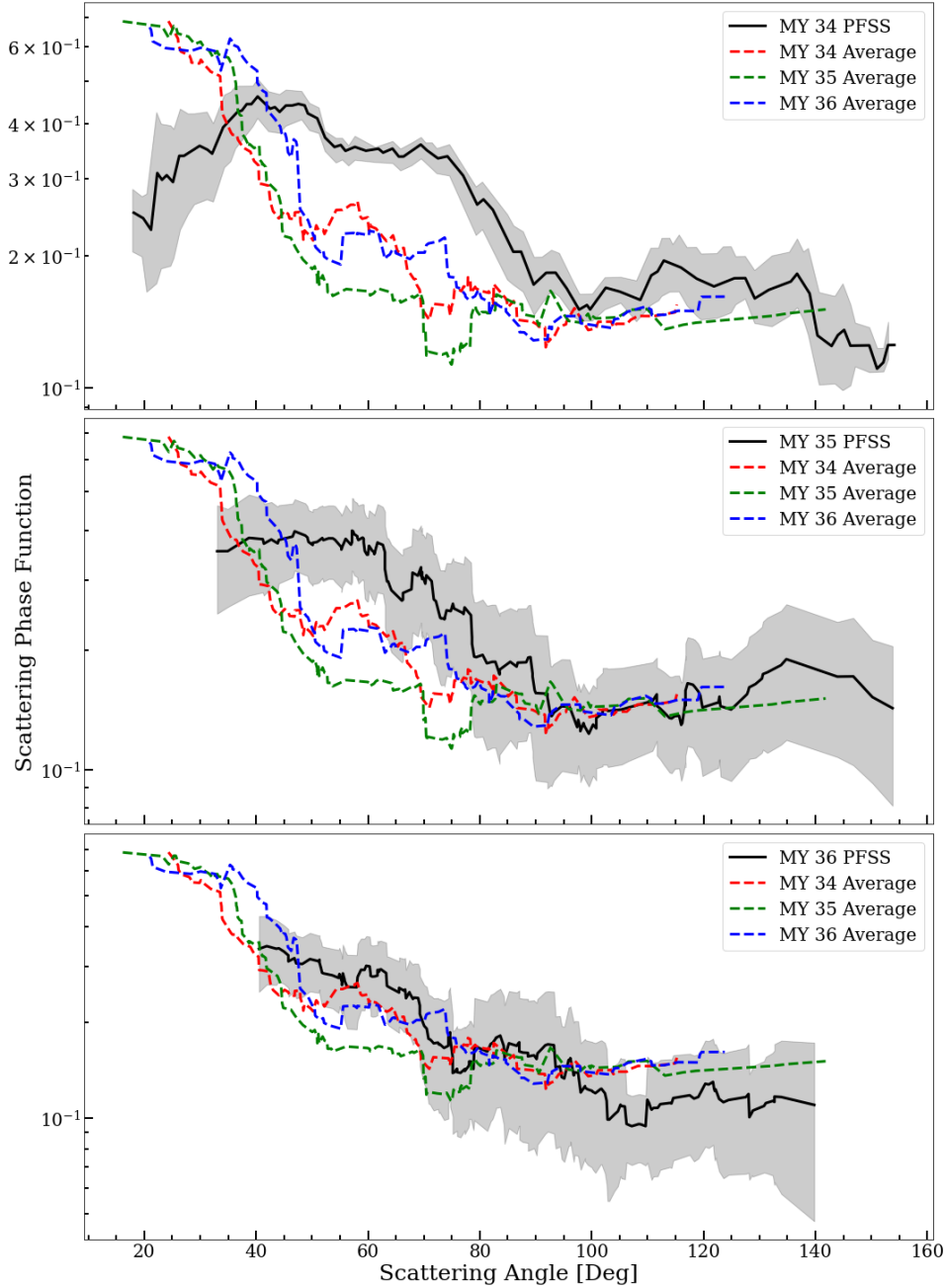
Figure 3.14: A comparison of our three phase functions with the PFSS phase functions for MY 34–36, including the 95 percent confidence interval for the PFSS phase functions. Although both show the same flattening behaviour at large scattering angles, the PFSS curves begin their upward deviation approximately 20° further from the Sun than our results, and either flatten our or turn back down at small scattering angles.

Modeled Phase Functions of Water-Ice Crystal Geometries

To see if we can determine a dominant ice crystal geometry for the WICs present over Gale Crater during the ACB season, we compare our phase function with those modeled for seven randomly-oriented geometries by Yang and Liou (1996) and Yang et al. (2010): aggregates, bullet rosettes, droxtals, hollow and solid columns, plates, and spheres.

As seen in Table 3.2.2 and Fig. 3.15, none of the geometries show particularly convincing agreement with our results, with aggregates, hollow columns, plates, and spheres being the only geometries with R^2 values consistently above 0.5. From a visual examination, it's easy to see why. Our phase functions are smooth and flat (other than the Sunward increase that has been the subject of this chapter), while the modeled curves show local maxima near $22°$ and $46°$ that are responsible for the various optical phenomena (i.e. halos and parhelia) that can be observed in terrestrial cirrus clouds. The modeled phase functions tend to drop sharply near $120°$ before rising towards the backscattering direction. However, if we ignore the local maxima, the location and magnitude of the increase at low scattering angles in our phase functions does appear to closely follow the increase seen in all of the models.
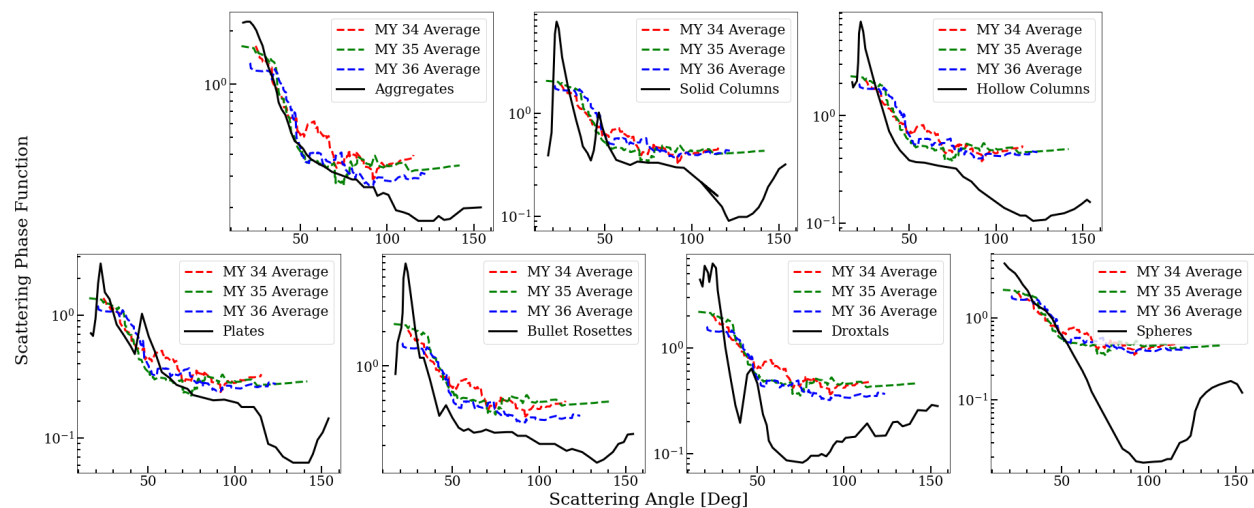
Figure 3.15: Comparisons between our three phase functions and the phase functions of seven randomly-oriented crystal geometries. Many of the modeled curves contain local maxima and minima that do not appear in our data, potentially indicating a particle size mismatch.

86

3.3 Discussion

We have found generally poor agreement between our derived phase functions and nearly every other phase function that we compare them to. Although we see the expected increase in the forward scattering direction that is present in the comparison phase functions but not in the PFSS data, our phase functions lack the local maxima present in the crystal geometry curves and are flatter than the non-MSL Martian phase functions at larger scattering angles.

As previously mentioned, it is likely that the phase functions of Yang and Liou (1996) and Yang et al. (2010) are inappropriate for comparison with Martian phase functions due to a fundamental difference in assumed particle sizes. Much like our phase functions, none of the MSL, Viking, or TES phase functions show the 22° or 46° local maxima, which is consistent with Martian clouds having smaller particle sizes than terrestrial cirrus clouds. As a result, any attempts to draw conclusions about the ice crystal geometries of ACB clouds using these data should be viewed with suspicion.

Differing particle sizes are not the only plausible explanation for the poor agreement that we see between our phase functions and seven ice crystal phase functions. It is possible that Martian WICs have exotic crystal geometries that are not observed on Earth. For example, rather than being composed of nearly-pure water ice, the scattering centres could be dust particles coated in a thin layer of ice. It is also possible that Martian WICs contain a mixture of ice crystal geometries rather than a single dominant geometry, which has been observed to occur in terrestrial cirrus clouds (Whiteway et al., 2004). To examine this possibility, we can fit our derived phase functions to a linear combination of the seven ice crystal phase functions and the two dust phase functions. The results can be seen in Fig. 3.16, showing a preference for a combination of dust and aggregate ices. However, none of the fits are particularly good and fall outside the 95% confidence interval of our observations across many of the observed scattering angles, indicating that a mixture of dust and Earth-like ice crystals is not the most plausible explanation for our results.
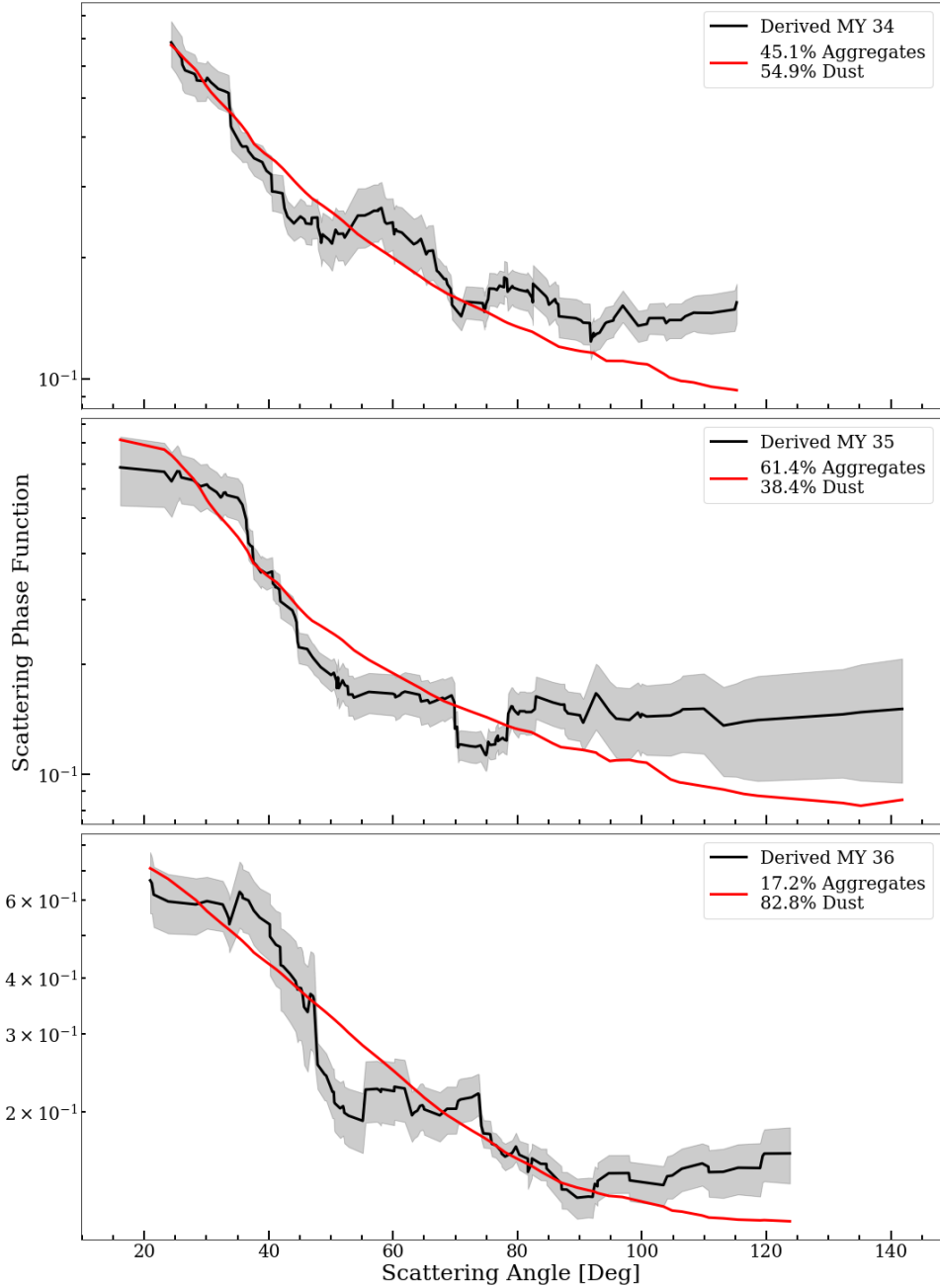
Figure 3.16: Fitting a linear combination of the seven ice crystal geometries and dust to our three derived phase functions. In all three cases, the fit preferred a combination of dust and aggregate ices. Although the combined phase function fits our observations better than any of the individual phase functions, the fit still falls outside of our observations' 95% confidence interval, suggesting that our observations cannot be explained through a linear combination of multiple types of scattering centres.

The extremely poor agreement between our ZM/SHM-derived phase functions and the PFSS-derived phase functions was surprising, given that both observations use MSL's Navcams and both are derived through observations of ACB clouds. There is one fundamental difference between the two observations that may explain the discrepancy. To save on data volume, the PFSS takes three frames at each pointing, the minimum required to perform mean-frame subtraction, while the ZM and SHM each use eight frames. It may be the case that by including more frames in the mean frame, we are able to more robustly extract the radiances of near-Sun features in the ZMs and SHMs than we are in the PFSS. If further analysis shows this to be the case, then it likely warrants a modification to the PFSS for the MY 37 ACB season and beyond.

Harder to explain is the difference between our phase functions and the Viking and TES phase functions. The TES phase functions in particular are unusual in that they are derived for ACB clouds, the same as we are observing. This may be a consequence of the different wavelengths used by TES and MSL. The TES phase functions were derived from observations in the thermal infrared, while MSL's Navcams operate in the visible. It is known that the optical properties of terrestrial cirrus clouds are quite different in the infrared versus the visible – for example, they are optically thin in the visible but comparatively optically thick in the infrared, leading to their being the only cloud type that creates a net warming effect of Earth's surface (Stephens and Webster, 1981). If a similar effect occurs in Martian WICs, it could account for the different phase functions observed for ACB clouds by TES and MSL.

The difference in observed wavelengths should be considered for the Viking and Pathfinder phase functions as well. The Viking phase functions were derived from observations using the Viking Orbiter's Infrared Thermal Mapper, so they may be subject to the same challenges as the TES phase functions when comparing them to our results. The Pathfinder phase function is more directly comparable, as the Imager for Mars Pathfinder observed in a spectral range of 444 – 965 nm, entirely overlapping the Navcams' 600 – 800 nm spectral range.

The fact that we may be observing a small diurnal difference in the shape of the phase function is potentially interesting, particularly given that the difference appears in the ACB seasons immediately before and after the MY 34 global dust storm but not in MY 36. It was previously pointed out that because Cooper et al. (2019); Innanen et al. (2021), and Innanen et al. (2022) used MCS opacities, which are all taken at the same local time, any information on diurnal variability would likely be lost. However, because the apparent difference is so small, we do not yet have sufficient data to confidently say that it is real and not an artifact of which points were selected for analysis.

Chapter 4

Conclusions

4.1 Lunar Micro Cold Traps

Permanently-shadowed regions (PSRs) near the lunar poles have been a subject of scientific interest for a number of years due to their ability to cold-trap volatile molecules over geologically long timescales. With the Artemis program poised to return humans to the Moon to stay later this decade, there has been increased interest in characterizing the resource potential of lunar PSRs. Existing orbital datasets are severely limited by their low resolutions, averaging over fine details at smaller scales. The goal of this work was to examine the effect that small-scale terrain features have on the thermal conditions present at the LCROSS impact site and to see if this effect could explain the volatile abundances observed in the impact plume.

To examine this question, we constructed an illumination and thermal model of a realistic rough surface based off of orbital altimetry of Cabeus Crater and the LCROSS impact site. We found that the small-scale structure of the lunar surface plays a critical role in determining the thermal environment of PSRs at human scales, with maximum temperatures across a single pixel spanning approximately 10 K. We also determined that maximum temperatures are not necessarily the best indication of volatile stability, as there exists a large set of

points that are only briefly above any given temperature threshold. Given that the low temperatures would not impart large velocities to molecules that undergo sublimation, the effective cold-trapping area might be much larger than the maximum temperature map implies.

Our analysis also shows that the available cold-trapping area is not sufficient to explain the LCROSS impact abundances. This could either indicate that most of the exhumed volatiles came from the subsurface, where stability is largely decoupled from surface temperatures, or that the Moon's volatile contents are limited by delivery sources rather than the available cold-trapping area.

4.2 The Scattering Phase Function of Martian Water-Ice Clouds

Using cloud movies taken by the Mars Science Laboratory Curiosity rover during the ACB season, we have derived scattering phase functions for Mars Years $34 - 36$. Our observations span a wide range of scattering angles, from $\sim 20°$ to $\sim 140°$. We find that there is very minimal variability in the phase function, either diurnally or interannually, which is consistent with the results of Innanen et al. (2021). Simultaneously, we were able to derive mean opacities for the ACB using observations taken at high scattering angles. Here too we see little variability, though this is inconsistent with Kloos et al. (2018), who found that ACB clouds over Gale Crater have higher opacities in the morning than in the afternoon.

To examine whether our results make sense in a larger context, we compared our phase function with other Martian phase functions from MSL (Cooper et al., 2019; Innanen et al., 2021), TES (Clancy et al., 2003), and Viking (Clancy and Lee, 1991). We find reasonable agreement with Viking polar and midlatitude clouds but poor agreement with TES aphelion clouds, which is surprising considering that we are observing the latter and not the former. The TES aphelion phase functions both have a local minimum at intermediate scattering

angles, while our phase functions are flat except for in the forward scattering direction. The disagreement between our results and the PFSS-derived phase functions is surprising given that all of the MSL data were acquired using the same instrument on the same rover at (roughly) the same location on the Martian surface. The PFSS-derived phase functions begin their upward turn approximately 20° before ours and turn back downward near 40°, while our phase functions continue upward. We hypothesize that some of this difference may be explained by the eight frames per pointing of the ZMs/SHMs allowing for enhanced clarity of near-solar features compared to the three frames per pointing of the PFSS.

Finally, we attempt to constrain the dominant ice crystal habit of ACB clouds through comparison with phase functions derived for terrestrial cirrus clouds (Yang and Liou, 1996; Yang et al., 2010). The best-fitting geometry are aggregates, with R^2 values greater than 0.85 in MY 34 and MY 35, and greater than 0.7 in MY 36. The only other geometries with R^2 values consistently above 0.5 are plates and spheres. There is an important caveat to these results, however: the crystal sizes in Martian and terrestrial WICs may not be comparable. Yang et al. (2010) assume a maximum crystal size of 50 μm. Although the Phoenix mission derived an ice crystal size of 42 μm from LiDAR observations of virga fall rates, the particle sizes of near-equatorial clouds may be significantly smaller. For example, Clancy et al. (2003) found that high-altitude and polar hood clouds have particle sizes between 1 and 2 μm, while the ACB has particle sizes between 3 and 4 μm. A difference in the microphysical properties of terrestrial and Martian WICs could account for why our phase functions are smooth and lacking the local peaks observed in the Yang et al. (2010) phase functions that are responsible for scattering phenomena like halos, parhelia, and pillars that are observed regularly on Earth, but have only conclusively been seen once on Mars (Lemmon et al., 2022).

Chapter 5

Future Work

5.1 Lunar Micro Cold Traps

In this thesis, we have explored only a very small portion of the parameter space available to us at a single point on the lunar surface. Consequently, we are left with a number of avenues for expanding our work.

First, we could adjust the surficial features of our upscaled terrain. This could include changing the RMS slope of the Gaussian surface or another parameter such as the albedo. Because we do not have *in-situ* measurements of the properties of the lunar surface near the LCROSS impact site at the scales we are examining, our model uses best guess values based on global averages. It is entirely possible that the actual values differ substantially from the average values, so it could be worthwhile to examine how varying the physical parameters of the surface affects the temperatures.

There are additional improvements that could be made to our terrain model. One shortcoming of using interpolated terrain is that it is limited by the data that exist at the original resolution. It cannot replicate features too small to be visible at 240 metres per pixel, like small craters and boulders. Cai and Fa (2020) found that the surface roughness at the scales we investigated here is controlled by small craters that have degraded over time, so

constructing a terrain model that incorporates these effects could be a worthwhile path to explore in the future. A future terrain model could also incorporate the varying RMS slope seen at different lengthscales rather than using just one value.

The LCROSS impact site was selected because it was an opportunity to link observed and modeled volatile abundances in a way that was not possible at other locations. However, this would could easily be expanded to additional sites, particularly those currently being examined as suitable sites for the Artemis Base Camp. With the delivery of VIPER to the lunar south pole in the imminent future, we will soon have an additional set of *in-situ* data to test our modeled results against.

Finally, we have only looked at surficial temperatures. Given that much of the Moon's volatile content might be buried beneath the surface, it would make sense to examine the subsurface temperature distribution as well and how vertical migration of volatiles might have affected what was available to be exhumed at the time of the LCROSS impact.

5.2 The Scattering Phase Function of Martian Water-Ice Clouds

Our results here focused on MY 34–36, as this was both the range of unpublished data and the period during which the PFSS was executed. However, our previously-published cloud opacity papers (Moores et al., 2015; Kloos et al., 2016, 2018) all relied on the assumption of a flat phase function, which we have now shown is inappropriate. These works were aware of the potential problem; indeed, Kloos et al. (2016) reported an initial lower limit for the phase function using ZMs and SHMs in combination with MCS water-ice opacity retrievals. However, because Kloos et al. (2016) restricted their measurements to the range of scattering angles between 70° and 115° (within the area where the assumption of a flat phase function holds), they did not examine the near-Sun region where the discrepancy arises. When looking at all of the movies taken during the first two MYs of the MSL mission, we may find a wider

range of scattering angles, which could justify a reanalysis of those data.

In each movie, we examined only one set of points, a byproduct of the fact that our initial goal was to update the record of cloud opacities. Because the Navcam frame covers a wide range of scattering angles in a single image, it should be possible to extract multiple phase function measurements from each movie, assuming that multiple cloud features are visible. Doing so would allow us to add more data points to our phase function curve (thus making the rolling averages more robust) without increasing the number of observations.

As previously noted, the difference between the PFSS and ZM/SHM results at low scattering angles may be a result of the former using three frames per pointing while the latter use eight. To examine whether or not this is the case, we could redo some of our low scattering angle calculations using three frames from the ZMs and SHMs that most closely replicate the temporal spacing between the PFSS frames. If this analysis reveals that the number of frames is driving the difference, then it could be worth exploring modifications to the PFSS for the MY 37 ACB season and beyond. Operationally, this could be a challenge given that the PFSS is already a lengthy observation (~ 20 minutes) and adding more frames would make it even longer. As such, we would need to put forward strong evidence in favour of an increased science return to justify the bigger hit to data resources and power availability.

Although the assumption of a flat phase function was the most obvious problem with our radiative transfer model, it was not the only problem that we identified. Notably, we found that cloud opacities are suppressed near sunrise and sunset, likely due to the decreased contrast between the clouds and the darkened background sky when the Sun is near the horizon. It is not yet clear what effect (if any) this has on the previously-identified diurnal trends, as it appears to affect morning and afternoon measurements equally. It is also not obvious if there is a simple way to correct for this error (as there was with the phase function), or if the model will have to be rebuilt from the ground up.

Finally, in this thesis we specifically only looked at data taken during the ACB season. However, the cadence of ZM and SHM observations is not limited to this time of year,

continuing through the dusty perihelion season as well. During the dusty season, we assume that the clouds observed by MSL are made up of dust rather than water ice. It might then be possible to apply the methods discussed here to those clouds, allowing for the determination of a dust cloud phase function in addition to one for water-ice clouds. This could be challenging since the opacities of dust clouds are less regular and predictable than that of the ACB, but one could perhaps find a way to use Mastcam tau measurements as a proxy for dust cloud opacities.

References

Apollo 15: Preliminary Science Report, 289, Jan 1972. URL https://ui.adsabs.harvard.edu/abs/1972NASSP.289...... ADS Bibcode: 1972NASSP.289......

J. R. Arnold. Ice in the lunar polar regions. *JGR*, 84:5659–5668, Sept. 1979. doi: 10.1029/JB084iB10p05659.

J. L. Bandfield, P. O. Hayne, J.-P. Williams, B. T. Greenhagen, and D. A. Paige. Lunar surface roughness derived from lro diviner radiometer observations. *Icarus*, 248: 357–372, Mar 2015. ISSN 0019-1035. doi: 10.1016/j.icarus.2014.11.009. ADS Bibcode: 2015Icar..248..357B.

A. B. Binder. Lunar Prospector: Overview. *Science*, 281:1475, Sept. 1998. doi: 10.1126/science.281.5382.1475.

G. Bischof, B. A. Cooper, and J. E. Moores. A record of water-ice clouds at the phoenix landing site derived from modeling met temperature data. *The Planetary Science Journal*, 3(4):97, Apr 2022. ISSN 2632-3338. doi: 10.3847/PSJ/ac649e.

W. V. Boynton, G. F. Droege, I. G. Mitrofanov, T. P. McClanahan, A. B. Sanin, M. L. Litvak, M. Schaffner, G. Chin, L. G. Evans, J. B. Garvin, K. Harshman, A. Malakhov, G. Milikh, R. Sagdeev, and R. Starr. High spatial resolution studies of epithermal neutron emission from the lunar poles: Constraints on hydrogen mobility. *Journal of Geophysical*

Research (Planets), 117:E00H33, Dec 2012. ISSN 0148-0227. doi: 10.1029/2011JE003979. ADS Bibcode: 2012JGRE..117.0H33B.

Y. Cai and W. Fa. Meter-Scale Topographic Roughness of the Moon: The Effect of Small Impact Craters. *Journal of Geophysical Research (Planets)*, 125(8):e06429, Aug. 2020. doi: 10.1029/2020JE006429.

Y. Cai and W. Fa. Meter-scale topographic roughness of the moon: The effect of small impact craters. *Journal of Geophysical Research: Planets*, 125(8):e2020JE006429, 2020. ISSN 2169-9100. doi: 10.1029/2020JE006429.

C. Campbell, D. Ellison, C. Smith, and J. Moores. Updated Altitudes for Martian Water-Ice Clouds above Gale Crater. In *European Planetary Science Congress*, pages EPSC2021–451, Sept. 2021. doi: 10.5194/epsc2021-451.

C. L. Campbell, A. M. Kling, S. D. Guzewich, C. L. Smith, J. L. Kloos, M. T. Lemmon, C. A. Moore, B. A. Cooper, R. M. Haberle, and J. E. Moores. Estimating the altitudes of Martian water-ice clouds above the Mars Science Laboratory rover landing site. *Planetary and Space Science*, 182:104785, Mar. 2020. doi: 10.1016/j.pss.2019.104785.

C. L. Campbell, J. L. Kloos, C. L. Smith, D. Ellison, C. W. Hayes, A. C. Innanen, and J. E. Moores. Wind direction record of aerosols observed by the mars science laboratory. In *Seventh International Workshop on the Mars Atmosphere: Modelling and Observations*, page 1205, June 2022.

G. D. Cassini. *Philosophical Transactions of the Royal Society of London Series I*, 2:615–617, Jan. 1666.

R. T. Clancy and S. W. Lee. A new look at dust and clouds in the mars atmosphere: analysis of emission-phase-function sequences from global viking irtm observations. *Icarus*, 93: 135–158, Sep 1991. ISSN 0019-1035. doi: 10.1016/0019-1035(91)90169-T. ADS Bibcode: 1991Icar...93..135C.

R. T. Clancy, A. W. Grossman, M. J. Wolff, P. B. James, D. J. Rudy, Y. N. Billawala, B. J. Sandor, S. W. Lee, and D. O. Muhleman. Water vapor saturation at low altitudes around mars aphelion: A key to mars climate? *Icarus*, 122:36–62, Jul 1996. ISSN 0019-1035. doi: 10.1006/icar.1996.0108. ADS Bibcode: 1996Icar..122...36C.

R. T. Clancy, M. J. Wolff, and P. R. Christensen. Mars aerosol studies with the mgs tes emission phase function observations: Optical depths, particle sizes, and ice cloud types versus latitude and solar longitude. *Journal of Geophysical Research (Planets)*, 108:5098, Sep 2003. ISSN 0148-0227. doi: 10.1029/2003JE002058. ADS Bibcode: 2003JGRE..108.5098C.

A. Colaprete, P. Schultz, J. Heldmann, D. Wooden, M. Shirley, K. Ennico, B. Hermalyn, W. Marshall, A. Ricco, R. C. Elphic, D. Goldstein, D. Summy, G. D. Bart, E. Asphaug, D. Korycansky, D. Landis, and L. Sollitt. Detection of Water in the LCROSS Ejecta Plume. *Science*, 330(6003):463, Oct. 2010. doi: 10.1126/science.1186986.

A. Colaprete, R. C. Elphic, M. Shirley, K. Ennico-Smith, D. S. S. Lim, K. Zacny, and C. J. The volatiles investigating polar exploration rover (viper) mission. page 1523, Mar 2021. ADS Bibcode: 2021LPI....52.1523C.

B. Cooper, M. de la Torre Juárez, M. Mischna, M. Lemmon, G. Martínez, D. Kass, A. R. Vasavada, C. Campbell, and J. Moores. Thermal forcing of the nocturnal near surface environment by martian water ice clouds. *Journal of Geophysical Research: Planets*, 126 (12):e2020JE006737, 2021. ISSN 2169-9100. doi: 10.1029/2020JE006737.

B. A. Cooper, J. E. Moores, D. J. Ellison, J. L. Kloos, C. L. Smith, S. D. Guzewich, and C. L. Campbell. Constraints on Mars Aphelion Cloud Belt phase function and ice crystal geometries. *Planetary and Space Science*, 168:62–72, Apr. 2019. doi: 10.1016/j.pss.2019.01.005.

J. Crank and P. Nicolson. A practical method for numerical evaluation of solutions of partial differential equations of the heat-conduction type. *Advances in Computational Mathematics*, 6:207–226, Dec. 1996. doi: 10.1007/BF02127704.

B. J. R. Davidsson and S. Hosseini. Implications of surface roughness in models of water desorption on the moon. *Monthly Notices of the Royal Astronomical Society*, 506(3): 3421–3429, Sep 2021. ISSN 0035-8711. doi: 10.1093/mnras/stab1360.

B. J. R. Davidsson, H. Rickman, J. L. Bandfield, O. Groussin, P. J. Gutiérrez, M. Wilska, M. T. Capria, J. P. Emery, J. Helbert, L. Jorda, A. Maturilli, and T. G. Mueller. Interpretation of thermal emission. i. the effect of roughness for spatially resolved atmosphereless bodies. *Icarus*, 252:1–21, May 2015. ISSN 0019-1035. doi: 10.1016/j.icarus.2014.12.029. ADS Bibcode: 2015Icar..252....1D.

D. De Rosa, B. Bussey, J. T. Cahill, T. Lutz, I. A. Crawford, T. Hackwill, S. van Gasselt, G. Neukum, L. Witte, A. McGovern, P. M. Grindrod, and J. D. Carpenter. Characterisation of potential landing sites for the european space agency's lunar lander project. *Planetary and Space Science*, 74(1):224–246, 2012. ISSN 0032-0633. doi: https://doi.org/10.1016/j.pss.2012.08.002. URL `https://www.sciencedirect.com/science/article/pii/S0032063312002395`. Scientific Preparations For Lunar Exploration.

V. R. Eke, L. F. A. Teodoro, D. J. Lawrence, R. C. Elphic, and W. C. Feldman. A quantitative comparison of lunar orbital neutron data. *The Astrophysical Journal*, 747:6, Mar 2012. ISSN 0004-637X. doi: 10.1088/0004-637X/747/1/6. ADS Bibcode: 2012ApJ...747....6E.

E. C. Ezell and L. N. Ezell. *On Mars: Exploration of the Red Planet.* NASA, 1984.

W. C. Feldman, R. C. Reedy, and D. S. McKay. Lunar neutron leakage fluxes as a function of composition and hydrogen content. *GRL*, 18(11):2157–2160, Nov. 1991. doi: 10.1029/91GL02618.

W. C. Feldman, S. Maurice, A. B. Binder, B. L. Barraclough, R. C. Elphic, and D. J. Lawrence. Fluxes of Fast and Epithermal Neutrons from Lunar Prospector: Evidence

for Water Ice at the Lunar Poles. *Science*, 281:1496, Sept. 1998. doi: 10.1126/science.281.5382.1496.

G. R. Gladstone, S. A. Stern, K. D. Retherford, R. K. Black, D. C. Slater, M. W. Davis, M. H. Versteeg, K. B. Persson, J. W. Parker, D. E. Kaufmann, A. F. Egan, T. K. Greathouse, P. D. Feldman, D. Hurley, W. R. Pryor, and A. R. Hendrix. LAMP: The Lyman Alpha Mapping Project on NASA's Lunar Reconnaissance Orbiter Mission. *SSR*, 150(1-4):161–181, Jan. 2010. doi: 10.1007/s11214-009-9578-6.

G. R. Gladstone, K. D. Retherford, A. F. Egan, D. E. Kaufmann, P. F. Miles, J. W. Parker, D. Horvath, P. M. Rojas, M. H. Versteeg, M. W. Davis, T. K. Greathouse, D. C. Slater, J. Mukherjee, A. J. Steffl, P. D. Feldman, D. M. Hurley, W. R. Pryor, A. R. Hendrix, E. Mazarico, and S. A. Stern. Far-ultraviolet reflectance properties of the moon's permanently shadowed regions. *Journal of Geophysical Research (Planets)*, 117:E00H04, Jan 2012. ISSN 0148-0227. doi: 10.1029/2011JE003913. ADS Bibcode: 2012JGRE..117.0H04G.

R. O. Green, C. Pieters, P. Mouroulis, M. Eastwood, J. Boardman, T. Glavich, P. Isaacson, M. Annadurai, S. Besse, D. Barr, B. Buratti, D. Cate, A. Chatterjee, R. Clark, L. Cheek, J. Combe, D. Dhingra, V. Essandoh, S. Geier, J. N. Goswami, R. Green, V. Haemmerle, J. Head, L. Hovland, S. Hyman, R. Klima, T. Koch, G. Kramer, A. S. K. Kumar, K. Lee, S. Lundeen, E. Malaret, T. McCord, S. McLaughlin, J. Mustard, J. Nettles, N. Petro, K. Plourde, C. Racho, J. Rodriquez, C. Runyon, G. Sellar, C. Smith, H. Sobel, M. Staid, J. Sunshine, L. Taylor, K. Thaisen, S. Tompkins, H. Tseng, G. Vane, P. Varanasi, M. White, and D. Wilson. The moon mineralogy mapper (m3) imaging spectrometer for lunar science: Instrument description, calibration, on-orbit measurements, science data calibration and on-orbit validation. *Journal of Geophysical Research: Planets*, 116(E10), 2011. ISSN 2156-2202. doi: 10.1029/2011JE003797. URL `https://onlinelibrary.wiley.com/doi/abs/10.1029/2011JE003797`.

A. S. Hale, L. K. Tamppari, D. S. Bass, and M. D. Smith. Martian water ice clouds: A view from Mars Global Surveyor Thermal Emission Spectrometer. *Journal of Geophysical Research (Planets)*, 116(E4):E04004, Apr. 2011. doi: 10.1029/2009JE003449.

Hansen. On the construction of new lunar tables, and on some points in the lunar theory depending on the conformation of the moon with respect to its centre of gravity. *Monthly Notices of the Royal Astronomical Society*, 15(1):1–16, Nov 1854. ISSN 0035-8711. doi: 10.1093/mnras/15.1.1a.

J. Haruyama, M. Ohtake, T. Matsunaga, T. Morota, C. Honda, Y. Yokota, C. M. Pieters, S. Hara, K. Hioki, K. Saiki, H. Miyamoto, A. Iwasaki, M. Abe, Y. Ogawa, H. Takeda, M. Shirao, A. Yamaji, and J.-L. Josset. Lack of exposed ice inside lunar south pole shackleton crater. *Science*, 322:938, Nov 2008. ISSN 0036-8075. doi: 10.1126/science.1164020. ADS Bibcode: 2008Sci...322..938H.

J. Haruyama, S. Yamamoto, Y. Yokota, M. Ohtake, and T. Matsunaga. An explanation of bright areas inside shackleton crater at the lunar south pole other than water-ice deposits. *Geophysical Research Letters*, 40(15):3814–3818, 2013. ISSN 1944-8007. doi: 10.1002/grl.50753.

P. O. Hayne, D. A. Paige, J. T. Schofield, D. M. Kass, A. Kleinböhl, N. G. Heavens, and D. J. McCleese. Carbon dioxide snow clouds on mars: South polar winter observations by the mars climate sounder. *Journal of Geophysical Research: Planets*, 117(E8), 2012. ISSN 2156-2202. doi: 10.1029/2011JE004040. URL `https://onlinelibrary.wiley.com/doi/abs/10.1029/2011JE004040`.

P. O. Hayne, A. Hendrix, E. Sefton-Nash, M. A. Siegler, P. G. Lucey, K. D. Retherford, J.-P. Williams, B. T. Greenhagen, and D. A. Paige. Evidence for exposed water ice in the moon's south polar regions from lunar reconnaissance orbiter ultraviolet albedo

and temperature measurements. *Icarus*, 255:58–69, Jul 2015. ISSN 0019-1035. doi: 10.1016/j.icarus.2015.03.032. ADS Bibcode: 2015Icar..255...58H.

P. O. Hayne, J. L. Bandfield, M. A. Siegler, A. R. Vasavada, R. R. Ghent, J.-P. Williams, B. T. Greenhagen, O. Aharonson, C. M. Elder, P. G. Lucey, and D. A. Paige. Global regolith thermophysical properties of the moon from the diviner lunar radiometer experiment. *Journal of Geophysical Research: Planets*, 122(12):2371–2400, 2017. doi: https://doi.org/10.1002/2017JE005387. URL `https://agupubs.onlinelibrary.wiley.com/doi/abs/10.1002/2017JE005387`.

P. O. Hayne, O. Aharonson, and N. Schörghofer. Micro cold traps on the Moon. *Nature Astronomy*, 5:169–175, Jan. 2021. doi: 10.1038/s41550-020-1198-9.

P. Helfenstein and M. K. Shepard. Submillimeter-Scale Topography of the Lunar Regolith. *Icarus*, 141(1):107–131, Sept. 1999. doi: 10.1006/icar.1999.6160.

B. Hermalyn, P. H. Schultz, M. Shirley, K. Ennico, and A. Colaprete. Scouring the surface: Ejecta dynamics and the lcross impact event. *Icarus*, 218:654–665, Mar 2012. ISSN 0019-1035. doi: 10.1016/j.icarus.2011.12.025. ADS Bibcode: 2012Icar..218..654H.

W. Herschel. On the Remarkable Appearances at the Polar Regions of the Planet Mars, the Inclination of Its Axis, the Position of Its Poles, and Its Spheroidical Figure; With a Few Hints Relating to Its Real Diameter and Atmosphere. By William Herschel, Esq. F. R. S. *Philosophical Transactions of the Royal Society of London Series I*, 74:233–273, Jan. 1784.

D. P. Hinson and R. J. Wilson. Temperature inversions, thermal tides, and water ice clouds in the martian tropics. *Journal of Geophysical Research (Planets)*, 109:E01002, Jan 2004. ISSN 0148-0227. doi: 10.1029/2003JE002129. ADS Bibcode: 2004JGRE..109.1002H.

Y. Hong, G. Liu, and J. L. F. Li. Assessing the radiative effects of global ice clouds based on cloudsat and calipso measurements. *Journal of Climate*, 29:7651–7674, Nov 2016. ISSN 0894-8755. doi: 10.1175/JCLI-D-15-0799.1. ADS Bibcode: 2016JCli...29.7651H.

A. Innanen, B. Cooper, C. Campbell, S. Guzewich, J. Kloos, and J. Moores. A Comparison of Aphelion Cloud Belt Phase Functions Before and After the Mars Year 34 Global Dust Storm. In *European Planetary Science Congress*, pages EPSC2021–372, Sept. 2021. doi: 10.5194/espc2021-372.

A. C. Innanen, B. A. Cooper, C. L. Campbell, S. D. Guzewich, J. L. Kloos, H. M. Sapers, and J. E. Moores. The Aphelion Cloud Belt Phase Function at Gale Crater. In *Seventh International Workshop on the Mars Atmosphere: Modelling and Observations*, page 3505, June 2022.

S. J. Keihm. Interpretation of the lunar microwave brightness temperature spectrum: Feasibility of orbital heat flow mapping. *Icarus*, 60(3):568–589, Dec. 1984. doi: 10.1016/0019-1035(84)90165-9.

J. L. Kloos, J. E. Moores, M. Lemmon, D. Kass, R. Francis, M. de la Torre Juárez, M.-P. Zorzano, and F. J. Martín-Torres. The first Martian year of cloud activity from Mars Science Laboratory (sol 0-800). *Advances in Space Research*, 57(5):1223–1240, Mar. 2016. doi: 10.1016/j.asr.2015.12.040.

J. L. Kloos, J. E. Moores, J. A. Whiteway, and M. Aggarwal. Interannual and Diurnal Variability in Water Ice Clouds Observed from MSL Over Two Martian Years. *Journal of Geophysical Research (Planets)*, 123(1):233–245, Jan. 2018. doi: 10.1002/2017JE005314.

J. L. Kloos, J. E. Moores, J. Sangha, T. G. Nguyen, and N. Schorghofer. The Temporal and Geographic Extent of Seasonal Cold Trapping on the Moon. *Journal of Geophysical Research (Planets)*, 124(7):1935–1944, July 2019. doi: 10.1029/2019JE006003.

J. L. Kloos, J. E. Moores, P. J. Godin, and E. Cloutis. Illumination conditions within permanently shadowed regions at the lunar poles: Implications for in-situ passive remote sensing. *Acta Astronautica*, 178:432–451, Jan. 2021. doi: 10.1016/j.actaastro.2020.09.012.

S. D. Koeber, M. S. Robinson, and E. J. Speyerer. Lroc observations of permanently shadowed regions on the moon. page 2811, Mar 2014. ADS Bibcode: 2014LPI....45.2811K.

M. G. Langseth, S. J. Keihm, and K. Peters. Revised lunar heat-flow values. *Lunar and Planetary Science Conference Proceedings*, 3:3143–3171, Apr. 1976.

L. J. Lanzerotti, W. L. Brown, and R. E. Johnson. Ice in the polar regions of the moon. *JGR*, 86:3949, May 1981. doi: 10.1029/JB086iB05p03949.

D. J. Lawrence, R. C. Elphic, W. C. Feldman, H. O. Funsten, and T. H. Prettyman. Performance of orbital neutron instruments for spatially resolved hydrogen measurements of airless planetary bodies. *Astrobiology*, 10:183–200, Mar 2010. ISSN 1531-1074. doi: 10.1089/ast.2009.0401. ADS Bibcode: 2010AsBio..10..183L.

D. J. Lawrence, V. R. Eke, R. C. Elphic, W. C. Feldman, H. O. Funsten, T. H. Prettyman, and L. F. A. Teodoro. Technical comment on "hydrogen mapping of the lunar south pole using the lro neutron detector experiment lend". *Science*, 334:1058, Nov 2011. ISSN 0036-8075. doi: 10.1126/science.1203341. ADS Bibcode: 2011Sci...334.1058L.

C. Lee, M. I. Richardson, C. E. Newman, and M. A. Mischna. The sensitivity of solsticial pauses to atmospheric ice and dust in the marswrf general circulation model. *Icarus*, 311:23–34, Sep 2018. ISSN 0019-1035. doi: 10.1016/j.icarus.2018.03.019. ADS Bibcode: 2018Icar..311...23L.

M. T. Lemmon. The Mars Science Laboratory Optical Depth Record. In *Eighth International Conference on Mars*, volume 1791 of *LPI Contributions*, page 1338, July 2014.

M. T. Lemmon, D. Toledo, V. Apestigue, I. Arruego, M. J. Wolff, P. Patel, S. Guzewich, A. Colaprete, A. Vicente-Retortillo, L. Tamppari, F. Montmessin, M. de la Torre Juarez, J. Maki, T. McConnochie, A. Brown, and J. F. Bell III. Hexagonal prisms form in water-ice clouds on mars, producing halo displays seen by perseverance rover. *Geophysical Research Letters*, 49(17):e2022GL099776, 2022. ISSN 1944-8007. doi: 10.1029/2022GL099776.

S. Li, P. G. Lucey, R. E. Milliken, P. O. Hayne, E. Fisher, J.-P. Williams, D. M. Hurley, and R. C. Elphic. Direct evidence of surface exposed water ice in the lunar polar regions. *Proceedings of the National Academy of Sciences*, 115(36):8907–8912, Sep 2018. ISSN 0027-8424, 1091-6490. doi: 10.1073/pnas.1802345115.

R. E. Lingenfelter, E. H. Canfield, and W. N. Hess. The Lunar Neutron Flux. *JGR*, 66(9): 2665–2671, Sept. 1961. doi: 10.1029/JZ066i009p02665.

K.-N. Liou. *Radiation and cloud processes in the atmosphere: Theory, observation, and modeling.* Oxford University Press, 1992.

M. L. Litvak, I. G. Mitrofanov, A. Sanin, A. Malakhov, W. V. Boynton, G. Chin, G. Droege, L. G. Evans, J. Garvin, D. V. Golovin, K. Harshman, T. P. McClanahan, M. I. Mokrousov, E. Mazarico, G. Milikh, G. Neumann, R. Sagdeev, D. E. Smith, R. Starr, and M. T. Zuber. Global maps of lunar neutron fluxes from the lend instrument. *Journal of Geophysical Research (Planets)*, 117:E00H22, Jun 2012. ISSN 0148-0227. doi: 10.1029/2011JE003949. ADS Bibcode: 2012JGRE..117.0H22L.

J. Liu, M. I. Richardson, and R. J. Wilson. An assessment of the global, seasonal, and inter-annual spacecraft record of Martian climate in the thermal infrared. *Journal of Geophysical Research (Planets)*, 108(E8):5089, Aug. 2003. doi: 10.1029/2002JE001921.

P. Lowell. *Mars.* Jan 1895. URL https://ui.adsabs.harvard.edu/abs/1895mars.book.....L. ADS Bibcode: 1895mars.book.....L.

P. Lowell. *Mars and its Canals.* Jan 1906. URL https://ui.adsabs.harvard.edu/abs/1906maca.book.....L. ADS Bibcode: 1906maca.book.....L.

P. Lowell. *Mars as the Abode of Life.* Jan 1908. URL https://ui.adsabs.harvard.edu/abs/1908mal..book.....L. ADS Bibcode: 1908mal..book.....L.

P. Lowell. Mars in 1909 as seen at the lowell observatory. *Nature*, 84:172–173, Aug 1910. ISSN 0028-0836. doi: 10.1038/084172e0. ADS Bibcode: 1910Natur..84..172L.

P. Lucey. Understanding the Lunar Surface and Space-Moon Interactions. *Reviews in Mineralogy and Geochemistry*, 60(1):83–219, Jan. 2006. doi: 10.2138/rmg.2006.60.2.

P. Lucey. Understanding the lunar surface and space-moon interactions. *Reviews in Mineralogy and Geochemistry*, 60:83–219, Jan 2006. doi: 10.2138/rmg.2006.60.2. ADS Bibcode: 2006RvMG...60...83L.

P. G. Lucey, G. A. Neumann, M. A. Riner, E. Mazarico, D. E. Smith, M. T. Zuber, D. A. Paige, D. B. Bussey, J. T. Cahill, A. McGovern, P. Isaacson, L. M. Corley, M. H. Torrence, H. J. Melosh, J. W. Head, and E. Song. The global albedo of the moon at 1064 nm from lola. *Journal of Geophysical Research (Planets)*, 119:1665–1679, Jul 2014. ISSN 0148-0227. doi: 10.1002/2013JE004592. ADS Bibcode: 2014JGRE..119.1665L.

A. Martinez and M. A. Siegler. A Global Thermal Conductivity Model for Lunar Regolith at Low Temperatures. *Journal of Geophysical Research (Planets)*, 126(10):e06829, Oct. 2021. doi: 10.1029/2021JE006829.

S. Maurice, D. J. Lawrence, W. C. Feldman, R. C. Elphic, and O. Gasnault. Reduction of neutron data from lunar prospector. *Journal of Geophysical Research (Planets)*, 109:E07S04, Jun 2004. ISSN 0148-0227. doi: 10.1029/2003JE002208. ADS Bibcode: 2004JGRE..109.7S04M.

E. Mazarico, G. A. Neumann, D. E. Smith, M. T. Zuber, and M. H. Torrence. Illumination conditions of the lunar polar regions using LOLA topography. *Icarus*, 211(2):1066–1081, Feb. 2011. doi: 10.1016/j.icarus.2010.10.030.

R. S. Miller. Statistics for orbital neutron spectroscopy of the moon and other airless planetary bodies. *Journal of Geophysical Research (Planets)*, 117:E00H19, Apr 2012a. ISSN 0148-0227. doi: 10.1029/2011JE003984. ADS Bibcode: 2012JGRE..117.0H19M.

R. S. Miller. Reply to comment by i. mitrofanov and w. boynton on "statistics for orbital neutron spectroscopy of the moon and other airless planetary bodies". *Journal of Geophysical Research (Planets)*, 117:E10004, Oct 2012b. ISSN 0148-0227. doi: 10.1029/2012JE004123. ADS Bibcode: 2012JGRE..11710004M.

J. L. Mitchell, S. J. Lawrence, E. J. Speyerer, M. S. Robinson, and B. W. Denevi. Assessment of water ice at the lunar north pole based on lroc narrow angle camera imagery and mini-rf data. page 1746, Mar 2016. ADS Bibcode: 2016LPI....47.1746M.

I. Mitrofanov and W. Boynton. Comment on "statistics for orbital neutron spectroscopy of the moon and other planetary bodies" by r. s. miller. *Journal of Geophysical Research (Planets)*, 117:E10003, Oct 2012. ISSN 0148-0227. doi: 10.1029/2012JE004078. ADS Bibcode: 2012JGRE..11710003M.

I. G. Mitrofanov, A. Bartels, Y. I. Bobrovnitsky, W. Boynton, G. Chin, H. Enos, L. Evans, S. Floyd, J. Garvin, D. V. Golovin, A. S. Grebennikov, K. Harshman, L. L. Kazakov, J. Keller, A. A. Konovalov, A. S. Kozyrev, A. R. Krylov, M. L. Litvak, A. V. Malakhov, T. McClanahan, G. M. Milikh, M. I. Mokrousov, S. Ponomareva, R. Z. Sagdeev, A. B. Sanin, V. V. Shevchenko, V. N. Shvetsov, R. Starr, G. N. Timoshenko, T. M. Tomilina, V. I. Tretyakov, J. Trombka, V. S. Troshin, V. N. Uvarov, A. B. Varennikov, and A. A. Vostrukhin. Lunar Exploration Neutron Detector for the NASA Lunar Reconnaissance Orbiter. *SSR*, 150(1-4):183–207, Jan. 2010. doi: 10.1007/s11214-009-9608-4.

I. G. Mitrofanov, A. B. Sanin, W. V. Boynton, G. Chin, J. B. Garvin, D. Golovin, L. G. Evans, K. Harshman, A. S. Kozyrev, M. L. Litvak, A. Malakhov, E. Mazarico, T. McClanahan, G. Milikh, M. Mokrousov, G. Nandikotkur, G. A. Neumann, I. Nuzhdin, R. Sagdeev, V. Shevchenko, V. Shvetsov, D. E. Smith, R. Starr, V. I. Tretyakov, J. Trombka, D. Usikov, A. Varenikov, A. Vostrukhin, and M. T. Zuber. Hydrogen mapping of the lunar south pole using the lro neutron detector experiment lend. *Science*, 330:483, Oct 2010. ISSN 0036-8075. doi: 10.1126/science.1185696. ADS Bibcode: 2010Sci...330..483M.

I. G. Mitrofanov, W. V. Boynton, M. L. Litvak, A. B. Sanin, and R. D. Starr. Response to comment on "hydrogen mapping of the lunar south pole using the lro neutron detector experiment lend". *Science*, 334:1058, Nov 2011. ISSN 0036-8075. doi: 10.1126/science.1203483. ADS Bibcode: 2011Sci...334.1058M.

F. Montmessin, F. Forget, P. Rannou, M. Cabane, and R. M. Haberle. Origin and role of water ice clouds in the martian water cycle as inferred from a general circulation model. *Journal of Geophysical Research (Planets)*, 109:E10004, Oct 2004. ISSN 0148-0227. doi: 10.1029/2004JE002284. ADS Bibcode: 2004JGRE..10910004M.

J. E. Moores, M. T. Lemmon, H. Kahanpää, S. C. R. Rafkin, R. Francis, J. Pla-Garcia, K. Bean, R. Haberle, C. Newman, M. Mischna, A. R. Vasavada, M. de la Torre Juárez, N. Rennó, J. Bell, F. Calef, B. Cantor, T. H. Mcconnochie, A.-M. Harri, M. Genzer, M. H. Wong, M. D. Smith, F. J. Martín-Torres, M.-P. Zorzano, O. Kemppinen, and E. McCullough. Observational evidence of a suppressed planetary boundary layer in northern gale crater, mars as seen by the navcam instrument onboard the mars science laboratory rover. *Icarus*, 249:129–142, Mar 2015. ISSN 0019-1035. doi: 10.1016/j.icarus.2014.09.020. ADS Bibcode: 2015Icar..249..129M.

J. E. Moores, M. T. Lemmon, S. C. R. Rafkin, R. Francis, J. Pla-Garcia, M. de la Torre Juárez, K. Bean, D. Kass, R. Haberle, C. Newman, M. Mischna, A. Vasavada, N. Rennó, J. Bell, F. Calef, B. Cantor, T. H. Mcconnochie, A.-M. Harri, M. Genzer, M. Wong, M. D. Smith, F. Javier Martín-Torres, M.-P. Zorzano, O. Kemppinen, and E. McCullough. Atmospheric movies acquired at the Mars Science Laboratory landing site: Cloud morphology, frequency and significance to the Gale Crater water cycle and Phoenix mission results. *Advances in Space Research*, 55(9):2217–2238, May 2015. doi: 10.1016/j.asr.2015.02.007.

H. E. Newell. Harold Urey and the Moon. *Moon*, 7(1-2):1–5, Mar. 1973. doi: 10.1007/BF00578802.

S. Nozette, P. Rustan, L. P. Pleasance, D. M. Horan, P. Regeon, E. M. Shoemaker, P. D. Spudis, C. H. Acton, D. N. Baker, J. E. Blamont, B. J. Buratti, M. P. Corson, M. E. Davies, T. C. Duxbury, E. M. Eliason, B. M. Jakosky, J. F. Kordas, I. T. Lewis, C. L. Lichtenberg, P. G. Lucey, E. Malaret, M. A. Massie, J. H. Resnick, C. J. Rollins, H. S. Park, A. S. McEwen, R. E. Priest, C. M. Pieters, R. A. Reisse, M. S. Robinson, R. A. Simpson, D. E. Smith, T. C. Sorenson, R. W. Vorder Breugge, and M. T. Zuber. The Clementine Mission to the Moon: Scientific Overview. *Science*, 266(5192):1835–1839, Dec. 1994. doi: 10.1126/science.266.5192.1835.

S. Nozette, C. L. Lichtenberg, P. Spudis, R. Bonner, W. Ort, E. Malaret, M. Robinson, and E. M. Shoemaker. The Clementine Bistatic Radar Experiment. *Science*, 274(5292): 1495–1498, Nov. 1996. doi: 10.1126/science.274.5292.1495.

E. J. Öpik. The lunar atmosphere. *PLANSS*, 9(5):211–244, May 1962. doi: 10.1016/0032-0633(62)90149-6.

D. A. Paige, M. C. Foote, B. T. Greenhagen, J. T. Schofield, S. Calcutt, A. R. Vasavada, D. J. Preston, F. W. Taylor, C. C. Allen, K. J. Snook, B. M. Jakosky, B. C. Murray, L. A. Soderblom, B. Jau, S. Loring, J. Bulharowski, N. E. Bowles, I. R. Thomas, M. T. Sullivan, C. Avis, E. M. de Jong, W. Hartford, and D. J. McCleese. The Lunar Reconnaissance Orbiter Diviner Lunar Radiometer Experiment. *SSR*, 150(1-4):125–160, Jan. 2010a. doi: 10.1007/s11214-009-9529-2.

D. A. Paige, M. A. Siegler, J. A. Zhang, P. O. Hayne, E. J. Foote, K. A. Bennett, A. R. Vasavada, B. T. Greenhagen, J. T. Schofield, D. J. McCleese, M. C. Foote, E. DeJong, B. G. Bills, W. Hartford, B. C. Murray, C. C. Allen, K. Snook, L. A. Soderblom, S. Calcutt, F. W. Taylor, N. E. Bowles, J. L. Bandfield, R. Elphic, R. Ghent, T. D. Glotch, M. B. Wyatt, and P. G. Lucey. Diviner Lunar Radiometer Observations of Cold Traps in the Moon's South Polar Region. *Science*, 330(6003):479, Oct. 2010b. doi: 10.1126/science.1187726.

A. Petrosyan, B. Galperin, S. E. Larsen, S. R. Lewis, A. Määttänen, P. L. Read, N. Renno, L. P. H. T. Rogberg, H. Savijärvi, T. Siili, A. Spiga, A. Toigo, and L. Vázquez. The martian atmospheric boundary layer. *Reviews of Geophysics*, 49:RG3005, Sep 2011. ISSN 8755-1209. doi: 10.1029/2010RG000351. ADS Bibcode: 2011RvGeo..49.3005P.

M. I. Richardson, R. J. Wilson, and A. V. Rodin. Water ice clouds in the martian atmosphere: General circulation model experiments with a simple cloud scheme. *Journal of Geophysical Research (Planets)*, 107:5064, Sep 2002. ISSN 0148-0227. doi: 10.1029/2001JE001804. ADS Bibcode: 2002JGRE..107.5064R.

M. S. Robinson, S. M. Brylow, M. Tschimmel, D. Humm, S. J. Lawrence, P. C. Thomas, B. W. Denevi, E. Bowman-Cisneros, J. Zerr, M. A. Ravine, M. A. Caplinger, F. T. Ghaemi, J. A. Schaffner, M. C. Malin, P. Mahanti, A. Bartels, J. Anderson, T. N. Tran, E. M. Eliason, A. S. McEwen, E. Turtle, B. L. Jolliff, and H. Hiesinger. Lunar Reconnaissance Orbiter Camera (LROC) Instrument Overview. *SSR*, 150(1-4):81–124, Jan. 2010. doi: 10.1007/s11214-010-9634-2.

M. A. Rosenburg, O. Aharonson, J. W. Head, M. A. Kreslavsky, E. Mazarico, G. A. Neumann, D. E. Smith, M. H. Torrence, and M. T. Zuber. Global surface slopes and roughness of the moon from the lunar orbiter laser altimeter. *Journal of Geophysical Research: Planets*, 116(E2), 2011. doi: https://doi.org/10.1029/2010JE003716. URL `https://agupubs.onlinelibrary.wiley.com/doi/abs/10.1029/2010JE003716`.

L. Rubanenko and O. Aharonson. Stability of ice on the moon with rough topography. *Icarus*, 296:99–109, Nov 2017. ISSN 0019-1035. doi: 10.1016/j.icarus.2017.05.028.

A. B. Sanin, I. G. Mitrofanov, M. L. Litvak, B. N. Bakhtin, J. G. Bodnarik, W. V. Boynton, G. Chin, L. G. Evans, K. Harshman, F. Fedosov, D. V. Golovin, A. S. Kozyrev, T. A. Livengood, A. V. Malakhov, T. P. McClanahan, M. I. Mokrousov, R. D. Starr, R. Z.

Sagdeev, V. I. Tret'yakov, and A. A. Vostrukhin. Hydrogen distribution in the lunar polar regions. *Icarus*, 283:20–30, Feb 2017. ISSN 0019-1035. doi: 10.1016/j.icarus.2016.06.002.

I. Schlimme, A. Macke, and J. Reichardt. The impact of ice crystal shapes, size distributions, and spatial structures of cirrus clouds on solar radiative fluxes. *Journal of Atmospheric Sciences*, 62:2274–2283, Jul 2005. ISSN 0022-4928. doi: 10.1175/JAS3459.1. ADS Bibcode: 2005JAtS...62.2274S.

N. Schorghofer. Planetary-Code-Collection: Thermal and Ice Evolution Models for Planetary Surfaces. Zenodo, Dec. 2021.

N. Schorghofer and O. Aharonson. The Lunar Thermal Ice Pump. *The Astrophysical Journal*, 788(2):169, June 2014. doi: 10.1088/0004-637X/788/2/169.

N. Schorghofer and G. J. Taylor. Subsurface migration of h2o at lunar cold traps. *Journal of Geophysical Research: Planets*, 112 (E2), 2007. ISSN 2156-2202. doi: 10.1029/2006JE002779. URL https://onlinelibrary.wiley.com/doi/abs/10.1029/2006JE002779.

M. Siegler, D. Paige, J.-P. Williams, and B. Bills. Evolution of lunar polar ice stability. *Icarus*, 255:78–87, July 2015. doi: 10.1016/j.icarus.2014.09.037.

D. E. Smith, M. T. Zuber, G. B. Jackson, J. F. Cavanaugh, G. A. Neumann, H. Riris, X. Sun, R. S. Zellar, C. Coltharp, J. Connelly, R. B. Katz, I. Kleyner, P. Liiva, A. Matuszeski, E. M. Mazarico, J. F. McGarry, A.-M. Novo-Gradac, M. N. Ott, C. Peters, L. A. Ramos-Izquierdo, L. Ramsey, D. D. Rowlands, S. Schmidt, V. S. Scott, G. B. Shaw, J. C. Smith, J.-P. Swinski, M. H. Torrence, G. Unger, A. W. Yu, and T. W. Zagwodzki. The Lunar Orbiter Laser Altimeter Investigation on the Lunar Reconnaissance Orbiter Mission. *SSR*, 150(1-4):209–241, Jan. 2010. doi: 10.1007/s11214-009-9512-y.

M. D. Smith. Interannual variability in TES atmospheric observations of Mars during 1999-2003. *Icarus*, 167(1):148–165, Jan. 2004. doi: 10.1016/j.icarus.2003.09.010.

M. D. Smith. Spacecraft observations of the martian atmosphere. *Annual Review of Earth and Planetary Sciences*, 36:191–219, May 2008. ISSN 0084-6597. doi: 10.1146/annurev.earth.36.031207.124334. ADS Bibcode: 2008AREPS..36..191S.

N. J. S. Stacy, D. B. Campbell, and P. G. Ford. Arecibo radar mapping of the lunar poles: A search for ice deposits. *Science*, 276:1527–1530, Jan. 1997. doi: 10.1126/science.276.5318.1527.

G. L. Stephens and P. J. Webster. Clouds and climate: Sensitivity of simple systems. *Journal of the Atmospheric Sciences*, 38(2):235–247, Feb 1981. ISSN 0022-4928, 1520-0469. doi: 10.1175/1520-0469(1981)038¡0235:CACSOS¿2.0.CO;2.

L. K. Tamppari, R. W. Zurek, and D. A. Paige. Viking-era diurnal water-ice clouds. *Journal of Geophysical Research (Planets)*, 108(E7):5073, July 2003. doi: 10.1029/2002JE001911.

M. G. Tomasko, L. R. Doose, M. Lemmon, P. H. Smith, and E. Wegryn. Properties of dust in the martian atmosphere from the imager on mars pathfinder. *Journal of Geophysical Research*, 104:8987–9008, Apr 1999. ISSN 0148-0227. doi: 10.1029/1998JE900016. ADS Bibcode: 1999JGR...104.8987T.

H. C. Urey. The planets: their origin and development. *Mrs. Hepsa Ely Silliman Memorial Lectures*, 1952.

H. C. Urey. The origin and significance of the moon's surface. *Vistas in Astronomy*, 2: 1667–1680, Jan 1956. ISSN 0083-6656. doi: 10.1016/0083-6656(56)90091-5.

H. C. Urey. Meteorites and the moon. *Science*, 147(3663):1262–1265, Mar 1965. doi: 10.1126/science.147.3663.1262.

H. C. Urey, H. S. W. Massey, T. Gold, and S. K. Runcorn. Study of the ranger pictures of the moon. *Proceedings of the Royal Society of London. Series A. Mathematical and Physical Sciences*, 296(1446):418–431, Feb 1967. doi: 10.1098/rspa.1967.0034.

A. R. Vasavada, D. A. Paige, and S. E. Wood. Near-Surface Temperatures on Mercury and the Moon and the Stability of Polar Ice Deposits. *Icarus*, 141(2):179–193, Oct. 1999. doi: 10.1006/icar.1999.6175.

A. R. Vasavada, J. L. Bandfield, B. T. Greenhagen, P. O. Hayne, M. A. Siegler, J.-P. Williams, and D. A. Paige. Lunar equatorial surface temperatures and regolith properties from the Diviner Lunar Radiometer Experiment. *Journal of Geophysical Research (Planets)*, 117:E00H18, Apr. 2012. doi: 10.1029/2011JE003987.

K. Watson, B. Murray, and H. Brown. On the Possible Presence of Ice on the Moon. *JGR*, 66(5):1598–1600, May 1961. doi: 10.1029/JZ066i005p01598.

K. Watson, B. Murray, and H. Brown. The behavior of volatiles on the lunar surface. *Journal of Geophysical Research (1896-1977)*, 66(9):3033–3045, 1961. ISSN 2156-2202. doi: 10.1029/JZ066i009p03033.

J. Whiteway, C. Cook, M. Gallagher, T. Choularton, J. Harries, P. Connolly, R. Busen, K. Bower, M. Flynn, P. May, R. Aspey, and J. Hacker. Anatomy of cirrus clouds: Results from the Emerald airborne campaigns. *Geophysical Research Letters*, 31(24):L24102, Dec. 2004. doi: 10.1029/2004GL021201.

D. Williams. Mars fact sheet, 2020. URL https://nssdc.gsfc.nasa.gov/planetary/factsheet/marsfac

J. Williams, D. Boggs, and W. Folkner. De421 lunar orbit, physical librations, and surface coordinates, jpl iom 335-jw, db. *Technical Report. WF-20080314–001*, 2008.

R. J. Wilson and S. D. Guzewich. Influence of water ice clouds on nighttime tropical temperature structure as seen by the mars climate sounder. *Geophysical Research Letters*, 41:3375–3381, May 2014. ISSN 0094-8276. doi: 10.1002/2014GL060086. ADS Bibcode: 2014GeoRL..41.3375W.

R. J. Wilson, G. A. Neumann, and M. D. Smith. Diurnal variation and radiative influence of martian water ice clouds. *Geophysical Research Letters*, 34:L02710, Jan 2007. ISSN 0094-8276. doi: 10.1029/2006GL027976. ADS Bibcode: 2007GeoRL..34.2710W.

M. J. Wolff, J. F. Bell III, P. B. James, R. T. Clancy, and S. W. Lee. Hubble space telescope observations of the martian aphelion cloud belt prior to the pathfinder mission: Seasonal and interannual variations. *Journal of Geophysical Research: Planets*, 104(E4):9027–9041, 1999. doi: https://doi.org/10.1029/98JE01967. URL `https://agupubs.onlinelibrary.wiley.com/doi/abs/10.1029/98JE01967`.

M. J. Wolff, M. D. Smith, R. T. Clancy, R. Arvidson, M. Kahre, F. Seelos, S. Murchie, and H. Savijärvi. Wavelength dependence of dust aerosol single scattering albedo as observed by the Compact Reconnaissance Imaging Spectrometer. *Journal of Geophysical Research (Planets)*, 114(E9):E00D04, June 2009. doi: 10.1029/2009JE003350.

P. Yang and K. N. Liou. Geometric-optics integral-equation method for light scattering by nonspherical ice crystals. *Applied Optics*, 35(33):6568–6584, Nov. 1996. doi: 10.1364/AO.35.006568.

P. Yang, G. Hong, A. E. Dessler, S. S. C. Ou, K.-N. Liou, P. Minnis, and Harshvardhan. Contrails and induced cirrus: Optics and radiation. *Bulletin of the American Meteorological Society*, 91(4):473–478, Apr 2010. ISSN 0003-0007, 1520-0477. doi: 10.1175/2009BAMS2837.1.

L. Yu, Y. Fu, Y. Yang, R. Li, X. Qiu, and H. Cai. Assessment of longwave radiative effect of nighttime cirrus based on cloudsat and calipso measurements and single-column radiative transfer simulations. *Journal of Quantitative Spectroscopy and Radiative Transfer*, 221:87–97, Dec 2018. ISSN 0022-4073. doi: 10.1016/j.jqsrt.2018.09.019. ADS Bibcode: 2018JQSRT.221...87Y.

M. T. Zuber, J. W. Head, D. E. Smith, G. A. Neumann, E. Mazarico, M. H. Torrence,

O. Aharonson, A. R. Tye, C. I. Fassett, M. A. Rosenburg, and H. J. Melosh. Constraints on the volatile distribution within shackleton crater at the lunar south pole. *Nature*, 486:378–381, Jun 2012. ISSN 0028-0836. doi: 10.1038/nature11216. ADS Bibcode: 2012Natur.486..378Z.

List of Acronyms

ACB Aphelion Cloud Belt

CAO Cloud Altitude Observation

CCD Charge-Coupled Device

CPR Circular Polarization Ratio

DEM Digital Elevation Model

ENV Environmental Science

FFT Fast Fourier Transform

FOV Field of View

GDS Global Dust Storm

IR Infrared

LAMP Lyman Alpha Mapping Project

LCROSS Lunar Crater Observation and Sensing Satellite

LEND Lunar Exploration Neutron Detector

LOLA Lunar Orbiter Laser Altimeter

LOS Line of Sight

LP-NS Lunar Prospector Neutron Spectrometer

LRO Lunar Reconnaissance Orbiter

LROC Lunar Reconnaissance Orbiter Camera

NAC Narrow Angle Camera

Navcam Navigation Camera

NIR Near-Infrared

M^3 Moon Mineralogy Mapper

Mastcam Mast Camera

MCS Mars Climate Sounder

MFS Mean-Frame Subtraction

MRO Mars Reconnaissance Orbiter

MSL Mars Science Laboratory

MY Mars Year

PDS Planetary Data System

PFSS Phase Function Sky Survey

PSD Power Spectral Density

PSR Permanently-Shadowed Region

RMS Root-Mean-Square

RSM Remote Sensing Mast

SHM Suprahorizon Movie

SPENDI Shunt Prevention ENV Navcam Drop-In

SSR Seasonally-Shadowed Region

TES Thermal Emission Spectrometer

UV Ultraviolet

VIPER Volatiles Investigating Polar Exploration Rover

WIC Water-Ice Cloud

ZM Zenith Movie